Low-temperature thermochronology of the Chatkal-Kurama terrane (Uzbekistan-Tajikistan): insights into the Meso-Cenozoic thermal history of the western Tian Shan

Gilby Jepson*[1], Stijn Glorie[1], Dmitry Konopelko[2,3], Jack Gillespie[1], Martin Danišík[5], Rustam Mirkamalov[4], Yunus Mamadjanov[6,7], and Alan S. Collins[1]

[1]*Centre for Tectonics, Resources, and Exploration (TRaX, Department of Earth Sciences, The University of Adelaide, 5005, Australia.*

[2]*Saint Petersburg State University, 7/9 University Embankment, SPb 199034, Russia.*

[3]*Novosibirsk State University, 2 Pirogova St., Novosibirsk, 630090, Russia.*

[4]*State Committee of the Republic of Uzbekistan on Geology and Mineral Resources, Tashkent, Uzbekistan.*

[5]*John de Laeter Centre, TIGeR, School of Earth and Planetary Sciences, Curtin University, Perth, 6846, Australia.*

[6]*Institute of Geology, Earthquake Engineering and Seismology, Academy of Sciences of the Republic of Tajikistan*

[7]*Research Center for Ecology and Environment of Central Asia (Dushanbe), Chinese Academy of Sciences - Tajik Academy of Sciences*

July 19, 2018

Abstract

The Chatkal-Kurama terrane represents a key region in understanding the tectonic evolution of the western Tian Shan. In this contribution, we present new thermochronological data (apatite fission track and (U-Th-Sm)/He) and the associated thermal history models for 30 igneous samples from the Chatkal-Kurama terrane within Uzbekistan and Tajikistan (west of the Talas-Fergana fault), and integrate our data with published data from the western Tian Shan (east of the Talas Fergana fault). The Chatkal-Kurama terrane experienced a phase of rapid cooling during the Triassic-Jurassic at ~225-190 Ma, which we interpret as a far-field response to the closure of the Palaeo-Asian Ocean or

*corresponding author (gilby.jepson@adelaide.edu.au)

the accretion of the Qiangtang terrane on to the Eurasian margin. In the late Jurassic to the early Cretaceous, the Chatkal-Kurama terrane experienced a period of tectonic stability and denudation, before transitioning into a period of marine incursions of the Paratethys Sea. In contrast, fast cooling is recorded for the Kyrgyz western Tian Shan to the east of the Talas-Fergana fault. The differing thermal histories at either side of the Talas-Fergana fault suggest that the fault induced a topographic divide during the late Jurassic–early Cretaceous, with high relief in the east (Kyrgyz Tian Shan) and low relief to the west (Uzbek-Tajik Tian Shan). Finally, the Chatkal-Kurama terrane experienced renewed tectonic activity since ~30 Ma, related with the distant India-Eurasia collision and Pamir indentation. The Cenozoic reactivation induced crustal tilting of the Chatkal-Kurama terrane, progressively exposing deeper rocks to the south-west.

1 Introduction

Central Asia hosts the largest intracontinental mountain belt in the world, the Tian Shan. The Tian Shan is a vast mountain system that developed throughout the Mesozoic to Cenozoic as a response to tectonic forces at the distant Eurasian continental margins, and has long been studied to understand the far-field effects of continental collision (e.g. Allen et al. 1991, Hendrix et al. 1992, Jolivet et al. 2013). A number of studies have applied thermochronological techniques throughout the Tian Shan in order to constrain the timing and extent of intracontinental deformation (e.g. Sobel et al. 2006b, De Grave et al. 2011, Glorie et al. 2011, Macaulay et al. 2014, Bande et al. 2017b, Glorie & De Grave 2016).

These studies demonstrated that, following the final closure of the Palaeo-Asian (or Turkestan) Ocean and amalgamation of the terranes in the late Palaeozoic, the Tian Shan experienced several major periods of cooling during the Mesozoic to Cenozoic. During the Mesozoic, distinct cooling events have been interpreted as related with exhumation in response to a number of Cimmerian collisions (e.g. the collisions of Qiangtang, Lhasa, and Karakorum with Eurasia, Dumitru et al. 2001, De Grave et al. 2013, Jolivet et al. 2013, De Pelsmaeker et al. 2015, Glorie & De Grave 2016, Käßner et al. 2017b, Gillespie et al. 2017). The subsequent Cenozoic collision of India with Eurasia not only generated the Himalayas and the uplift of the Tibetan plateau, but is also thought to have driven uplift and deformation in the Asian continental interior, including the Tian Shan and other intracontinental mountain ranges (e.g. Molnar & Tapponnier 1975, Clift et al. 2002, Bouilhol et al. 2013). Cenozoic cooling and exhumation is mainly recorded in close vicinity to major faults within the Tian Shan (e.g. Glorie et al. 2011, De Grave et al. 2012, Macaulay et al. 2014, Glorie & De Grave 2016, Bande et al. 2017b). While the thermochronology of most of the central

Tian Shan (within Kyrgyzstan and China, to the east of the Talas Fergana fault) has been extensively studied (Figure 1), such studies currently do not account for the westernmost expression of the Tian Shan. A recent study by Bande et al. (2017b) investigated the thermochronology of the Kyrgyz Chatkal ranges (Figure 1) and obtained mainly Cenozoic cooling ages (~50-15 Ma), reflecting exhumation as a response to the indentation of the Pamir terrane. In this study, we apply low-temperature thermochronology to the Chatkal-Kurama terrane within western Uzbekistan and northern Tajikistan (west of the area studied by Bande et al. 2017b), plugging a critical gap in the thermochronological coverage of the region and developing a more complete picture of the thermal history of the western Tian Shan.

2 Geological Background

The ancestral Tian Shan formed in the late Palaeozoic during the closure of the Palaeo-Asian Ocean (PAO) and the subsequent collision of the Tarim Precambrian microcontinent with the southern margin of the early Palaeozoic Kazakhstan continent (e.g. Windley et al. 2007, Biske & Seltmann 2010, Xiao et al. 2013, Burtman 2015). The western part of the Tian Shan (within Tajikistan, Uzbekistan, Kyrgyzstan, and Kazakhstan) is traditionally subdivided into three major tectonic terranes: (1) the Northern Tian Shan, representing the deformed margin of the Palaeo-Kazakhstan microcontinent; (2) the Middle Tian Shan, composed of a Precambrian microcontinental sliver and a superimposed island-arc; and (3) the Southern Tian Shan, a late Palaeozoic fold-and-thrust belt (Figure 1, Biske & Seltmann 2010, Burtman 2015). These east-west trending linear terranes are cut by the north-west trending Talas-Fergana Fault with a total dextral offset of ~200 km (Figure 1, Burtman et al. 1996).

Our study area, the Chatkal-Kurama terrane, forms part of the Middle Tian Shan (MTS) that is exposed west of the Talas-Fergana Fault (TFF, Figure 1, e.g. Windley et al. 2007). The Chatkal-Kurama terrane formed due to the accretion of an island arc (locally known as the Chatkal Arc) onto the passive southern margin of the Palaeo-Kazakhstan during the late Ordovician (Alexeiev et al. 2016). This accretion caused the Chatkal arc to become the southern active margin of the Palaeo-Kazakhstan continent during the late Silurian – early Devonian, resulting in the generation of thick supra-subduction magmatic series (Konopelko, Seltmann, Mamadjanov, Romer, Rojas-Agramonte, Jeffries, Fidaev & Niyozov 2017, Dolgopolova et al. 2017). During the middle Devonian – early Carboniferous subduction halted and was followed by the deposition of carbonate sediments in a passive margin or transform fault environment (Dolgopolova et al. 2017). These sediments were subsequently uplifted and eroded before subduction

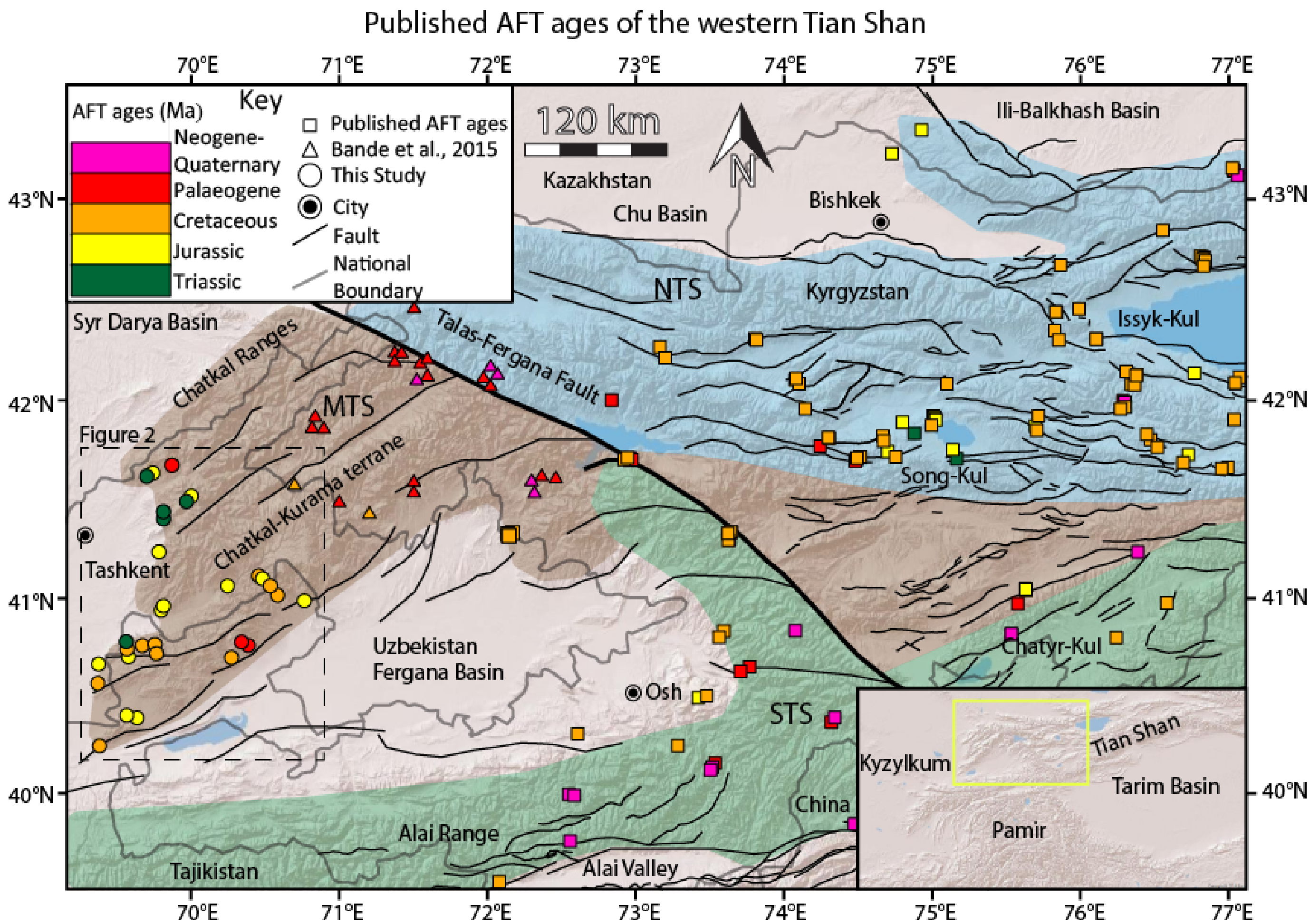

Figure 1: A shaded relief map of the western extent of the Tian Shan displaying published Mesozoic apatite fission track (AFT) ages for the region (colour coded following AFT central ages). Circle symbols represent sample location for data obtained in this study, triangles represent locations for data obtained by Bande et al. (2017b) (both to the west or in close proximity to the Talas-Fergana fault). Square symbols represent locations for published AFT ages from Sobel et al. (2006a,b), Glorie et al. (2010), De Grave et al. (2013), Macaulay et al. (2014), De Pelsmaeker et al. (2015), Käßner et al. (2017a), Bande et al. (2017c) and Nachtergaele et al. (2017). The Northern Tian Shan is denoted by NTS (shaded blue), the Middle Tian Shan by MTS (shaded brown), and the South Tian Shan by STS (shaded green).

under the southern margin of the Chatkal-Kurama terrane resumed in the early to middle Carboniferous, generating voluminous Andean-type intrusions and volcanics. This magmatic series, with ages in the range of ~320-300 Ma, comprise the majority of the Chatkal-Kurama terrane (Figure 2 Konopelko, Seltmann, Mamadjanov, Romer, Rojas-Agramonte, Jeffries, Fidaev & Niyozov 2017, Dolgopolova et al. 2017). The subsequent closure of the Palaeo-Turkestan ocean in the late Carboniferous resulted in voluminous, ~300-285 Ma post-collisional, granitoid magmatism during the Early Permian (Biske & Seltmann 2010, Seltmann et al. 2011, Konopelko, Seltmann, Mamadjanov, Romer, Rojas-Agramonte, Jeffries, Fidaev & Niyozov 2017, Dolgopolova et al. 2017).

The Mesozoic history of the Tian Shan is dominated by deformation caused by the collision of Cimmerian continental fragments with the southern margin of Eurasia [e.g. De Grave et al., 2012; Kässner et al., 2016b](e.g. De Grave et al. 2012, Käßner et al. 2017a). This period of Mesozoic deformation was initiated by the closure of the Palaeo-Asian Ocean (PAO) at the end of the Permian to the earliest Triassic (e.g. Xiao et al. 2009, Li et al. 2016). Subduction of the Palaeo-Tethys beneath Eurasia initiated in the Triassic, leading to the collision of the Qiangtang block to the southern Eurasian margin, which is thought to have induced extensive deformation to the Tian Shan (e.g. Ratschbacher et al. 2003, De Grave et al. 2011, Robinson 2015, Glorie & De Grave 2016). Subduction and accretion to the southern margin of Eurasia continued further south during the Jurassic and Early Cretaceous, culminating in the final closure of the Palaeo-Tethys Ocean (e.g. Kapp et al. 2007, Robinson 2015). Rapid Late Jurassic–Cretaceous cooling has been documented for the Kyrgyz Tian Shan (to the east of the TFF, e.g. De Grave et al. 2013, Nachtergaele et al. 2017). The extent of Jurassic and Cretaceous cooling in the westernmost Tian Shan (to the west of the TFF) is poorly defined. During the Late Jurassic–Early Cretaceous, coal deposits formed along the eastern margin of the Chatkal-Kurama terrane (Angren, Figure 2), suggesting a marine environment (Ahmedov 2000, Dill et al. 2008). To the south, the Fergana Basin (Figure 1), is characterised by basal sections of Jurassic conglomerate fining upward into Jurassic and Cretaceous sedimentary sequences, indicating that the Fergana Basin experienced marine incursions of the Paratethyan Sea (Burov & Molnar 1998, Bande et al. 2017b, De Pelsmaeker et al. 2018, Nachtergaele et al. 2017). Detailed analysis of the Late Cretaceous marine sediments suggested that the region was covered by a marine environment at least twice, once in the Turonian and again in the Maastrichtian (Ahmedov 2000, Yablonskaya 2004).

During the Cenozoic, the Tian Shan experienced renewed deformation, generating much of the high relief that can be found today. Many authors have identified a strong Cenozoic cooling signal within

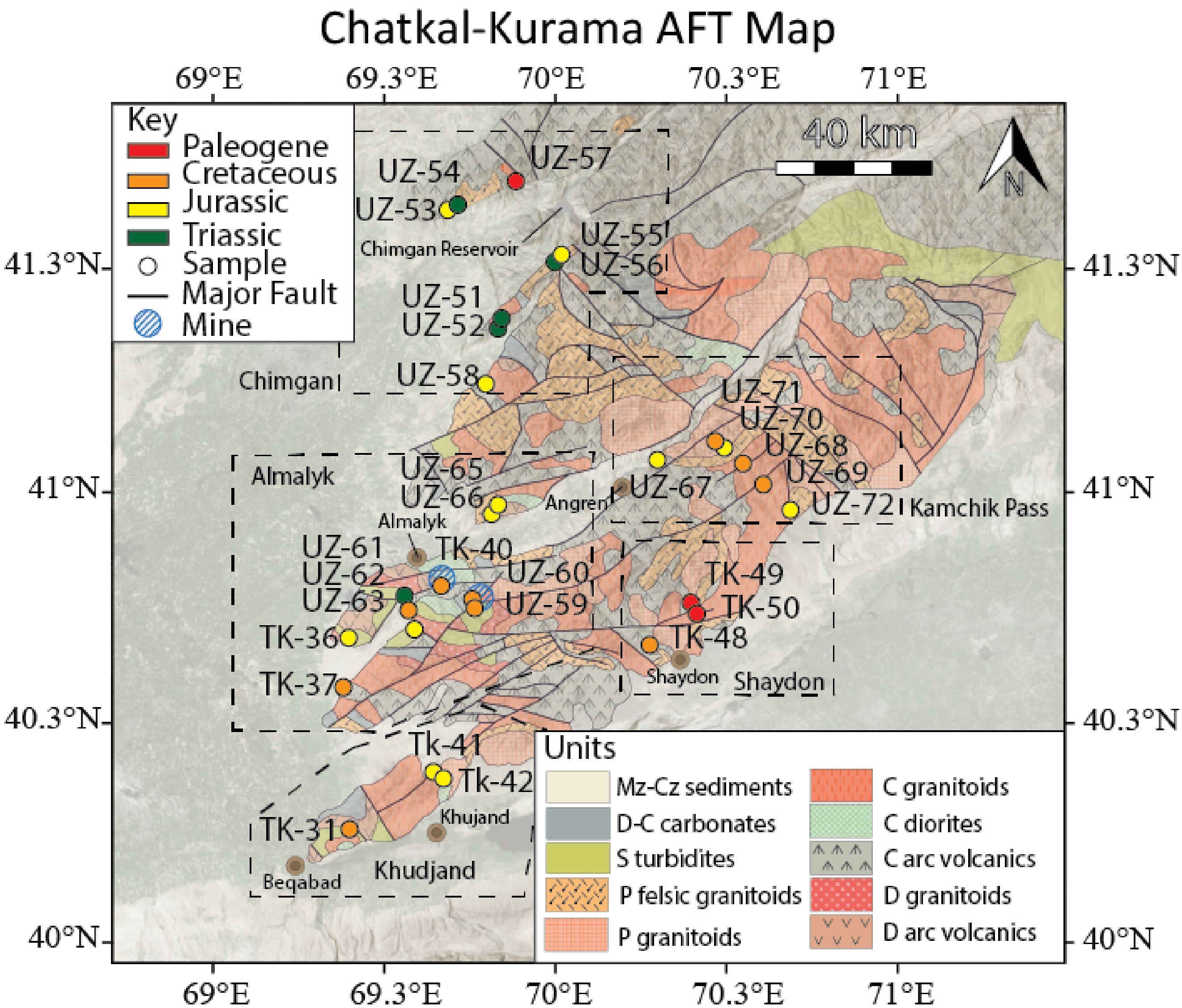

Figure 2: Geological map of the Chatkal-Kurama terrane modified from Dolgopolova et al. (2017). The map displays the locations for the apatite fission track (AFT) data obtained in this study. Sample symbols are colour coded following AFT central ages. A detailed summary of the AFT data is available in Supplementary File 1. *Mz* is the Mesozoic, *Cz* is the Cenozoic, *D* is Devonian, *C* is the Carboniferous, *S* is the Silurian, and *P* is the Permian.

the Tian Shan, which is thought to be related with the India-Eurasia collision and subsequent Pamir indentations with the Eurasian margin (e.g. Molnar & Tapponnier 1975, Sobel et al. 2006a, Aitchison et al. 2007, De Grave et al. 2007). In the western Tian Shan, previous studies have identified initiation of exhumation at ~30-20 Ma and accelerating of exhumation since ~15-10 Ma, which correlates with periods of Pamir convergence (e.g. Käßner et al. 2017b, Bande et al. 2017c, Jepson et al. 2018).

3 Methodology

New thermochronological data for 30 granitoid rock samples from the western Tian Shan are presented (Figure 2). Three different thermochronological methods were applied; (1) zircon (U-Th-Sm)/He dating (closure temperature ~180°C; Reiners et al. 2002), (2) apatite fission track thermochronology (partial annealing zone ~120-60°C; Wagner & Van den Haute 1992) and (3) apatite (U-Th-Sm)/He dating (closure temperature ~80-40°C, Zeitler et al. 1987).

3.1 Apatite fission track analysis (AFT)

The apatite fission track method is based on the temperature dependent annealing of mineral lattice damage features, known as 'fission tracks', that are created by the spontaneous decay of ^{238}U (Wagner & Van den Haute 1992). Fission tracks record the thermal history of a rock sample through the apatite partial annealing zone (APAZ) of ~120-60°C (Green 1986). Apatite grains were picked and mounted in epoxy resin, then polished to expose internal sections, and were subsequently chemically etched in a 5M HNO_3 solution for 20s at 20°C to reveal the natural spontaneous fission tracks. Fission track analysis was performed at The University of Adelaide using an Autoscan system. The concentration of uranium (^{238}U) and chlorine (^{35}Cl) of each apatite grain was measured using Laser Ablation-Inductively Coupled Plasma-Mass Spectrometry. Data reduction was performed in Iolite using the Trace Elements DRS (Paton et al. 2011). Instrumental drift correction was carried out using Madagascar apatite as an external standard, and elemental concentrations were calculated using ^{43}Ca as the internal standard. Age calculation was carried out as described in Hasebe et al. (2004) and De Grave et al. (2012), using the Durango apatite (McDowell et al. 2005) to perform a ζ-calibration (Vermeesch 2017). A duplicate sample was made for TK-50 and irradiated using californium (^{252}Cf) at The University of Melbourne in order to increase the likelihood of measuring a sufficient amount of confined tracks for thermal history reconstructions (Donelick & Miller 1991). For a detailed methodology see Glorie et al. (2017) and Gillespie et al. (2017).

3.2 Apatite and zircon (U-Th-Sm)/He

The (U-Th-Sm)/He thermochronometers are based on the diffusivity of ^{4}He. The thermal sensitivity for apatite helium (AHe) is 80-40°C, making it valuable for constraining the most recent thermal cooling event (Zeitler et al. 1987, Farley 2002). For zircon, the thermochronometer records the thermal history at ~190-170°C (Reiners et al. 2002, Guenthner et al. 2013). The (U-Th-Sm)/He analyses for this study were undertaken at the John de Laeter Centre, Curtin University and followed the protocols described in (Danišík et al. 2012).

Apatite and zircon crystals were hand-picked following the recommendations of Farley (2002), photographed and measured for physical dimensions, before being loaded in Pt (apatite) and Nb (zircon) microtubes. Helium (~4He) was extracted from apatite at ~900°C, under ultra-high vacuum using a diode laser and measured by isotope dilution on a Pfeiffer Prisma QMS-200 mass spectrometer. A "re-extract" was run after each sample to verify complete outgassing of the crystals. Helium gas results were corrected for blank, determined by heating empty microtubes using the same procedure. After the ~4He measurements, tubes containing the crystals were retrieved from the laser cell, spiked with ~235U and ~230Th and dissolved. Sample, blank, and spiked standard solutions were analysed by isotope dilution for ~238U and ~232Th, and by external calibration for ~147Sm on an Agilent 7500 ICP-MS. The total analytical uncertainty (TAU) was calculated as a square root of sum of squares of uncertainty on He and weighted uncertainties on U, Th, Sm and He measurements, and is typically $<5\%$ (1σ). The raw (U–Th)/He ages were corrected for alpha ejection (F_{T} correction) after Farley et al. (1996), whereby a homogenous distribution of U, Th and Sm was assumed for the crystals. Replicate analyses of internal standard Durango apatite (n=10) measured over the period of this study, yielded mean (U–Th–Sm)/He ages of 31.9 ± 1.9 Ma (1σ), consistent with the reference Durango (U–Th–Sm)/He age of 31.02 ± 1.01 Ma (McDowell et al. 2005). For the Fish Canyon zircon, we acquired 28.6 ± 0.8 Ma (n=10), which is in excellent agreement with the reference age of (Reiners 2005) at 28.3 ± 1.3 Ma.

3.3 Thermal History Modelling

Thermal history modelling was performed on a total of 24 samples, with a sufficient number of confined tracks (>10, although less tracks indicates less precision). The QTQt software (version 5.5.0) was applied, which uses Bayesian trans-dimensional Markov Chain Monte Carlo statistics to determine models for the cooling pathway of the sample (Gallagher 2012). Along with the confined track length, individual AFT, AHe, and ZHe ages were used in the modelling procedure. The concentration of ^{35}Cl was used as a kinetic parameter (Donelick et al. 2005). More details on the modelling approach can be found in (Gallagher 2012) and (Gillespie et al. 2017).

4 Results

For a systematic and thorough discussion, the results for the 30 samples in this study will be subdivided into five groups based on regional proximity to each other (Figure 2). The groups are named after nearby towns or mountain passes and will be discussed from north to south, and are as follows: (1) Chimgan, (2) Kamchik Pass, (3) Almalyk, (4) Shaydon, and (5) Khudjand (Figure 2). Tables 1 and 2 summarise the AFT and (U-Th-Sm)/He data. Detailed tables and figures for all single grain AFT, (U-Th-Sm)/He, mean track length (MTL) data and individual thermal history models are available in supplementary files 1, 2, 3, 4, 5, and 6.

Table 1: A summary table of the apatite fission track data(AFT): n is the number of grains analysed per sample and # of lengths is the number of confined track lengths idenfied in each sample. Elev is elevation in meters, age is the AFT central age in Ma, MTL is the mean track length in μ, and # is the number of confined tracks measured for each sample.

Sample	Lat	Long	Elev	n	Age	$\pm 1\sigma$	#	MTL	$\pm 1\sigma$
Chimgan									
UZ-51	41.391	69.857	1919	32	225.0	6.8	65	12.4	1.2
UZ-52	41.395	69.861	1769	5	235.0	20.0	-	-	-
UZ-53	41.629	69.725	1524	38	154.2	5.5	115	12.1	1.5
UZ-54	41.628	69.724	1109	37	207.2	4.4	170	12.4	1.1
UZ-55	41.528	70.024	1396	33	174.0	10.0	34	12.0	1.7
UZ-56	41.517	70.014	1909	34	218.9	6.3	64	12.7	1.3
UZ-57	41.684	69.894	1438	22	28.5	3.7	45	12.7	1.5
UZ-58	41.245	69.808	1207	31	171.3	7.5	31	12.7	1.6
Kamchick Pass									
UZ-67	41.072	70.271	1136	37	199.6	8.4	18	12.0	1.5
UZ-68	41.073	70.558	2139	27	135.0	12.0	24	11.8	1.1
UZ-69	41.027	70.609	1688	19	94.4	6.1	18	11.2	1.7
UZ-70	41.110	70.505	2061	27	156.0	15.0	13	11.4	1.2
UZ-71	41.125	70.479	1620	31	96.8	5.0	36	12.1	1.8

UZ-72	40.997	70.789	1530	41	167.0	12.0	63	12.1	1.4

Almalyk

UZ-59	40.775	69.778	1041	31	100.0	9.1	27	11.7	1.6
UZ-60	40.768	69.781	1222	39	141.4	8.4	51	12.4	1.3
UZ-61	40.772	69.586	705	38	205.8	6.4	34	12.9	1.0
UZ-62	40.752	69.591	752	28	143.8	8.6	66	13.0	1.2
UZ-63	40.712	69.603	878	39	182.0	9.8	56	12.8	1.2
UZ-65	40.950	69.824	827	17	187.0	14.0	17	12.4	1.0
UZ-66	40.971	69.838	915	31	196.0	12.0	61	12.9	1.0
TK-36	40.674	69.401	540	28	183.0	11.0	63	13.1	0.9
TK-37	40.576	69.396	489	35	103.6	5.1	14	12.0	2.2
TK-40	40.799	69.690	864	14	116.1	5.5	-	-	-

Shaydon

TK-48	40.678	70.292	1024	22	124.0	12.0	-	-	-
TK-49	40.746	70.426	1192	10	32.0	10.0	-	-	-
TK-50	40.768	70.410	1304	33	31.4	3.4	20	12.7	0.8

Khudjand

TK-31	40.254	69.408	500	40	131.0	5.0	75	11.9	1.5
TK-41	40.397	69.660	633	34	163.9	4.8	99	13.3	1.1
TK-42	40.379	69.683	540	20	176.0	10.0	-	-	-

4.1 Chimgan region

Eight granitoid samples were collected in the southern Chatkal Mountains surrounding Chimgan reservoir, in the north of our study area (Figure 2). The majority of samples from the Chimgan region display a Triassic AFT central age. Samples UZ-52, UZ-54, and UZ-56 yield unimodal AFT ages of 235 ± 20 Ma, 207 ± 4 Ma, and 219 ± 6 Ma respectively (Table 1). Samples UZ-54 and UZ-56 produced mean track lengths (MTL) of 12.4 ± 1.1 μm and 12.7 ± 1.3 μm, respectively. Sample UZ-51 displays a slightly bimodal age distribution, with 80% of the single grain ages preserving a similar Triassic age (225 ± 7 Ma) and 20% of single grain ages recording a Palaeogene signal (~52 ± 5 Ma, Supplementary File 3). Samples UZ-53, UZ-55, and UZ-58, which were sampled at slightly lower elevations (Table 1), yield ages of 155 ± 6 Ma, 174 ± 10 Ma, and 171 ± 8 Ma, respectively. Furthermore, they display reduced MTL values and broader confined track length distributions compared to the Triassic samples, with values of 12.1 ± 1.5 μm, 12.0 ± 1.7 μm, and 12.7 ± 1.6 μm, respectively. The most northerly sample (UZ-57), which was sampled in the Chatkal Ranges (an area of slightly higher relief; ~2000m, Figure 1), gave a younger AFT central age of 29 ± 4 Ma, with a MTL of 12.7 ± 1.5 μm.

4.2 Kamchik Pass transect

A series of samples were taken over an elevation profile across Kamchik Pass across the eastern limb of the Chatkal-Kurama terrane (Figure 2). In total, six granitoid samples were taken with a minimum of ~150m vertical distance between neighbouring samples, and were grouped into the Kamchik Pass transect.

The AFT central ages from the Kamchik Pass samples can be separated into Jurassic and Cretaceous ages. Sample UZ-67, east of the main sample transect, produced an AFT central age of 200 ± 8 Ma and a MTL of 12.0 ± 1.5 μm. Samples UZ-70 and UZ-72 were taken at low elevations along the Kamchik pass transect and yielded Jurassic central ages of 156 ± 15 Ma and 167 ± 12 Ma, respectively (Figure 2). The MTL for the sample that produced a Middle Jurassic AFT age (UZ-72) is 12.1 ± 1.4 μm, while for the Late Jurassic AFT sample (UZ-70) a shorter MTL of 11.4 ± 1.2 μm was recorded. Samples UZ-68, UZ-69, and UZ-71 yielded Cretaceous AFT ages of 135 ± 12 Ma, 94 ± 6 Ma, and 97 ± 5 Ma respectively (Table 1 and Figure 2). The three Cretaceous AFT age samples yielded, on average, lower MTLs compared to the Jurassic AFT samples of 11.8 ± 1.1 μm, 11.2 ± 1.7 μm, and 12.1 ± 1.8 μm, respectively. The samples along Kamchik Pass show no clear age-elevation relationship. Based on apatite quality, sample UZ-69 was selected for AHe analysis and yielded a Cenozoic AHe age of 13.5 ± 1.3 Ma, which is significantly younger than the AFT ages obtained for Kamchik Pass (Table 2 and Supplementary File 2).

4.3 Almalyk region

Ten samples were taken from mineral deposit hosting regions surrounding the town of Almalyk (Figure 2). This includes two samples taken in close vicinity to the Sari-Cheku porphyry copper-gold deposit (UZ-59 and UZ-60), and one sample from just south of the Kalmakyr porphyry deposit (TK-40, Seltmann & Porter 2005).

The AFT central ages obtained for the ten samples produced one Late Triassic age, four Jurassic ages,

Table 2: Mean zircon (U–Th–Sm)/He and apatite (U–Th–Sm)/He age and chemistry data. For single grain analysis, see Table S2. Concentrations of thorium, uranium and samarium in ng. He is the concentration of helium measured in ncc. Th/U is the ratio of thorium to uranium. Raw age is the age before the F_{T} correction is made. F_{T} is the alpha-ejection correction parameter of Farley et al. (1996). Cor. age is the age after applying the F_{T} correction. TAU is the total analytical uncertainty, and eU is the effective uranium (Guenthner et al. 2013).

Sample	^{232}Th	±(%)	^{238}U	±(%)	^{147}Sm	±(%)	He	±(%)	TAU(%)	Th/U	Raw age	±1σ	F_{T}	Cor. age	±1σ
Zircon (U-Th-Sm)/He Data															
TK-42	1.132	1.4	2.683	1.9	0.002	18.2	53.137	1.0	2.039	0.5	159.5	3.2	0.70	229.0	6.2
TK-36	1.077	1.4	4.027	1.9	0.002	14.9	93.629	0.7	1.952	0.3	179.9	3.5	0.72	244.4	8.1
Apatite (U-Th-Sm)/He Data															
UZ-69	0.111	3.8	0.051	4.0	0.022	0.3	0.075	2.4	3.8	2.2	8.0	0.3	0.60	13.5	1.3
TK-50	0.119	3.9	0.067	4.1	0.041	0.2	0.175	2.2	4.0	1.8	12.7	0.5	0.69	18.2	1.2
TK-49	0.056	4.1	0.039	4.2	0.011	0.4	0.130	2.1	4.0	1.4	20.8	0.8	0.53	27.5	2.5
TK-41	0.143	5.2	0.067	5.3	0.021	0.4	1.0	2.6	4.9	2.3	69.1	3.5	0.65	125.8	6.3
TK-36	0.097	4.7	0.093	4.9	0.014	0.4	1.5	2.7	4.9	1.0	110.5	5.3	0.71	178.6	8.9

and five Cretaceous ages. A Late Triassic AFT age was obtained for sample UZ-61 of 206 ± 6 Ma. The four Jurassic AFT ages are recorded by UZ-63, UZ-65, UZ-66, and TK-36, displaying ages of 182 ± 10 Ma, 187 ± 14 Ma, 196 ± 13 Ma, and 183 ± 11 Ma, respectively. The three samples that were taken near mineral deposits yielded Late Cretaceous ages. Samples TK-40, UZ-59, and UZ-60 gave AFT ages of 116 ± 6 Ma, 100 ± 9 Ma, and 141 ± 8 Ma, respectively. Away from the deposits, Cretaceous AFT ages were recorded for samples TK-37 and UZ-62, with central ages of 104 ± 5 Ma and 144 ± 9 Ma, respectively (Table 1 and Figure 2). Based on apatite and zircon quality, two Almalyk samples were selected for AHe analysis and one Almalyk sample was selected for ZHe analysis. Sample TK-40 produced an AHe age of 143 ± 7 Ma, which is slightly older than its AFT age of 116 ± 6 Ma. The AHe age for TK-36, calculated as 179 ± 9 Ma, is within error to its AFT age of 183 ± 11 Ma. Sample TK-36 was also selected for ZHe analysis yielded an age of 244 ± 8 Ma (Table 2).

The Late Triassic–-Early Jurassic samples of TK-36, UZ-61, UZ-63, UZ-65, and UZ-66 yielded, on average, longer MTLs of 13.1 ± 0.9 μm, 12.9 ± 1.0 μm, 12.8 ± 1.2 μm, 12.4 ± 1.0 μm, and 12.9 ± 1.0 μm, respectively. For the Cretaceous samples UZ-59, UZ-60, and UZ-62 slightly shorter MTLs of 11.7 ± 1.6 μm, 12.4 ± 1.3 μm, and 13.0 ± 1.2 μm were obtained (Table 1).

4.4 Shaydon region

The Shaydon region consists of three samples that were taken near the village of Shaydon, Tajikistan (Figure 2). Sample TK-48 yielded a Cretaceous central age of 124 ± 12 Ma. Samples TK-49, and TK-50 both yielded consistent Palaeogene AFT ages of 32 ± 10 Ma, and 31 ± 3 Ma (Table 1). AHe analysis was performed on both Palaeogene AFT age samples. For sample TK-49, an Oligocene AHe age of 28 ± 3 Ma was obtained that is within error to its AFT age, and for sample TK-50, and a Miocene AHe age of 18 ± 1 Ma was obtained, which is slightly younger than its corresponding AFT age (Table 2). Sample TK-50 was selected for ^{252}Cf irradiation to obtain a sufficient quantity of confined tracks, producing a MTL of 12.7 ± 0.8 μm (Table 1).

4.5 Khudjand region

The Khudjand region represents the most south-western extent of the Chatkal-Kurama terrane, from which three samples were taken (TK-41, TK-42, and TK-31). Samples TK-41, and TK-42 both yielded Jurassic AFT central ages of 164 ± 5 Ma and 176 ± 10 Ma, respectively. For sample TK-41, a MTL of 13.3 ± 1.1 μm was obtained. In contrast, sample TK-31, generated a Cretaceous AFT age of 131 ± 5 Ma and a lower MTL of 11.9 ± 1.5 μm (Table 1). Based on apatite quality, sample TK-41 was selected for AHe analysis, producing a Cretaceous age of 126 ± 14 Ma that is slightly younger than its corresponding AFT age of 164 ± 5 Ma. Sample TK-42 was selected for ZHe analysis, yielding a Triassic age of 229 ± 6 Ma (Table 2).

4.6 Thermal history models

Thermal history models were produced for samples with a sufficient quantity of confined tracks (>10, Table 1 and Supplementary File 5). Of the 30 samples analysed in this study, 24 were suitable for thermal history modelling. Figure 3 displays all time-temperature models calculated for the Chatkal-Kurama terrane. Detailed individual thermal models for each sample and modelling parameters are available in Supplementary File 5 and 6.

The thermal history models in this study show a distinct relationship between the AFT age and the thermal pathway obtained. The Triassic AFT age samples UZ-51, UZ-54, and UZ-56 from the Chimgan region and sample UZ-61 from the Almalyk region (green models in Figure 3) display rapid cooling through the APAZ during the Triassic (~250-220 Ma) followed by a long period of thermal stability during most of the Mesozoic and Cenozoic. Some samples show a subsequent cooling pulse since ~25 Ma, which is not well pronounced in the models (Figure 3). The thermal history models for the Early Jurassic AFT age samples TK-36, UZ-63, UZ-65, and UZ-66 from the Almlyk region and sample TK-41 from the Khudjand region (yellow models in Figure 3) show cooling through the APAZ during the latest Triassic–Early Jurassic (~215-190 Ma). The Jurassic AFT samples display a similar thermal history to the models obtained for the Triassic AFT age samples, relatively fast cooling in the Early Jurassic, followed by thermal quiescence (or slight reheating) during most of the Late Jurassic–Palaeogene. Several samples were affected by renewed cooling since ~35 Ma. The Late Jurassic AFT samples UZ-53, UZ-55, and UZ-58 from the Chimgan region, and samples UZ-67, UZ-70, and UZ-72 from the Kamchik Pass all display very similar thermal history models to those obtained for the Lower Jurassic AFT samples. However, the initial cooling during the Jurassic through the APAZ was slower. The Cretaceous AFT age samples UZ-69, UZ-69, and UZ-71 from the Kamchik Pass, samples UZ-59, UZ-60, and UZ-62 from the Almalyk region, and sample TK-31 from the Khudjand region (orange models in Figure 3), display rather slow cooling and increased residence time in the APAZ during the Cretaceous, followed by a renewed onset of cooling since ~30 Ma. Finally, the two Cenozoic samples, UZ-57 from the Chimgan region, and TK-50 from the Shaydon region (red models in Figure 3) both display fast cooling through the APAZ since ~35 Ma (Figure 3 and Supplementary File 5). In summary, the thermal history models indicate rapid cooling during the Triassic–Early Jurassic (~250-190 Ma), slow cooling or thermal quiescence during the Late Jurassic–Palaeogene and renewed cooling during the Neogene (~35-25 Ma).

5 Interpretation and discussion

5.1 Thermochronological interpretations

The sample locations within the Chatkal-Kurama terrane range from the south-western margin of the terrane, near Khudjand, to the Uzbekistan-Kazakhstan border around the Chimgan reservoir in the north (Figure 2). Over this geographic extent, the obtained AFT ages display a clear younging trend from the north-west to the south-east. The oldest (Triassic) AFT ages from the Chatkal-Kurama terrane were obtained on the north-western margin. Towards the south-east, a mixture of Jurassic and Cretaceous AFT ages were obtained, with Cretaceous ages becoming more abundant further south and near the mineral deposits in the Almalyk region. The youngest AFT ages identified in this study were obtained in the north of the study area (in the Chatkal Ranges) and in the south-east of the Chatkal-Kurama terrane, at the margin of the Fergana Basin (Figure 2).

As illustrated by the thermal history models (Figure 3), the Triassic and Early Jurassic AFT age samples cooled rapidly to the surface at that time and remained unaffected by any later thermal activity. The mid to Late Jurassic and Cretaceous AFT age samples underwent more protracted residence in the APAZ and partially record the subsequent Cenozoic cooling identified in the Cenozoic AFT age samples.

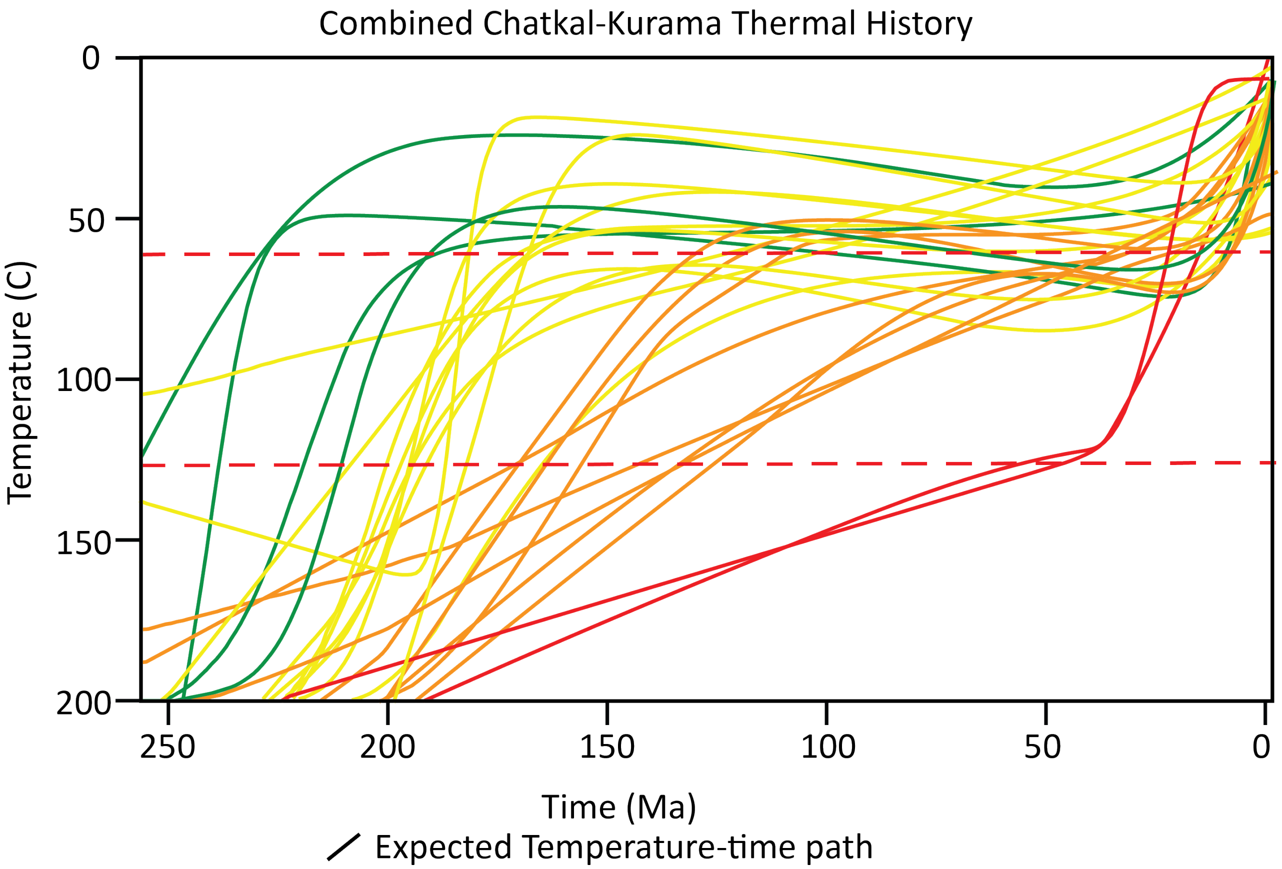

Figure 3: A plot displaying the modelled temperature-time paths for all samples within the Chatkal-Kurama terrane that yielded sufficient confined track data for modelling purposes. Modelling was performed using QTQt Gallagher (2012). Apatite and zircon U-Th/Sm data was used to refine the thermal models where appropriate. The temperature-time path is coloured according to apatite fission track central age; green is Triassic, yellow is Jurassic, orange is Cretaceous, and red is Palaeogene. The red-dashed line represents the apatite partial annealing zone. This figure demonstrates the relationship between Cretaceous apatite fission track age and increased residence time in the apatite partial annealing zone. Individual sample histograms and temperature-time plots are available in Supplementary Files 4 and 5, the used criteria for thermal modelling are tabulated in Supplementary File 6.

This pattern can be illustrated by plotting the MTL values for each sample against their corresponding AFT central ages (Figure 4). In this plot, our new data from the Chatkal-Kurama terrane is combined with Bande et al. (2017b) from the adjoining Chatkal Ranges in western Kyrgyzstan, and display a characteristic 'boomerang' trend (Green et al. 1986, Gallagher 2012). The longer MTLs suggest faster cooling, while shorter MTLs reflect prolonged residence in the APAZ. The 'boomerang plot' demonstrates that the Triassic and Early Jurassic AFT ages are indicative of a significant thermal event at that time. The Late Jurassic and Cretaceous AFT ages correspond to shorter MTLs and are thus, slowly cooled APAZ residence ages. In the Late Palaeogene, the 'boomerang' begins to curve back up towards longer MTLs, suggesting the start of a second thermal event (Figure 4). The latter event is better exposed in the higher relief of the Chatkal Ranges (Figure 1, Bande et al. 2017b), but also the south-eastern margin on the Chatkal-Kurama terrane, along the Fergana basin margin.

The (U-Th-Sm)/He data obtained in this study further illustrate the two thermal events that were identified in the boomerang plot and thermal history models (during the Triassic and Late Palaeogene–Early Neogene, Figure 3 and Figure 4). The ZHe ages (~250-225 Ma, TK-42 and TK-36) are in agreement with the Triassic AFT ages obtained from sample TK-42. Additionally, sample TK-36 yielded an Early Jurassic AHe age (~180 Ma) that is within error to its corresponding AFT age (183 ± 11 Ma, Table 2 and Figure 4). These results strengthen the claim that the Chatkal-Kurama terrane underwent fast cooling during the Triassic–Early Jurassic. Sample TK-41 and TK-40 yielded scattered Late Jurassic–Cretaceous AHe ages which were significantly younger or older than their corresponding AFT age (163 ± 5 Ma), suggesting slow cooling at that time (Table 2 and Supplementary File 2). Late Palaeogene–Early Neogene AHe ages (~28-14 Ma, UZ-69, TK-49, and TK-50) chronologically match corresponding AFT ages (~31 Ma), suggesting renewed cooling began during the Palaeogene, as illustrated by the thermal history models and boomerang plot (Figures 3 and 4, and Table 2).

The significant geographic younging trend throughout the Chatkal-Kurama terrane reflects the progressive influence of a Cenozoic thermal pulse from north-west to south-east. The north-western section of the Chatkal-Kurama terrane (excluding the Cenozoic AFT sample in the Chatkal Ranges) effectively represents a Triassic–Early Jurassic palaeo-surface while the Chatkal-Kurama terrane was, in our interpretation, progressively exhumed towards the south-east, during the Cenozoic. In addition, we suggest that the progressive exhumation to the south-east reflects a process of fault-block tilting. This Cenozoic tilting process exposed a deeper section of the thermal history of the Chatkal-Kurama terrane (that was at lower APAZ temperatures during the Cretaceous) in the south-east with respect to the north-west.

The Chatkal-Kurama terrane is bounded to the north-west by the Syrdarya Block, which represents a Mesoproterozoic to Neoproterozoic continental block, a part of the Kazakhstan palaeocontinent (Samygin & Burtman 2009, Dolgopolova et al. 2017, Konopelko, Klemd, Petrov, Apayarov, Nazaraliev, Vokueva, Scherstén & Sergeev 2017). To the south-east of the Chatkal-Kurama terrane, the Fergana Basin basement is a rigid piece of Palaeozoic crust (Figure 2, Burov & Molnar 1998). Both the Syrdarya Block and the Fergana basement are strong units within the Central Asian edifice that transmit stress from distant collisions at the Eurasian plate margins. The Chatkal-Kurama terrane is composed of weaker crust (e.g. volcanic arc) that is more easily deformed than the surrounding rigid block of the Fergana and Syrdarya blocks. Therefore, the crustal tilting can be explained by different crustal strengths in response to distant stresses. The north-east of the Chatkal-Kurama terrane was held in place along the margin of the Syrdarya Block, leading to the preservation of Triassic cooling ages, while the continental collisions on the southern Eurasian margin drove progressive tilting of the Chatkal-Kurama terrane, towards the Fergana basin margin, as demonstrated by the Cretaceous and Palaeogene AFT and AHe ages (Figure 2).

5.2 Thermotectonic evolution of the Chatkal-Kurama terrane

5.2.1 Triassic–Early Jurassic

This study reports a Triassic–Early Jurassic fast cooling pulse experienced by the Chatkal-Kurama terrane (Figures 2, 3, 4, and Table 2). The oldest thermochronological ages obtained from the north-western margin of the Chatkal-Kurama terrane are the Triassic ZHe (245 and 229 Ma) and AFT ages (225 Ma) from samples TK-36, TK-42, and UZ-51 (Figure 4). In comparison, the youngest age of magmatism identified in the Chatkal-Kurama terrane is Permian (~286 Ma, Konopelko, Seltmann, Mamadjanov, Romer, Rojas-Agramonte, Jeffries, Fidaev & Niyozov 2017). Therefore, a direct thermal relationship between the Triassic AFT ages to post-magmatic cooling can be excluded.

Previous thermochronological studies in the Tian Shan ascribe Triassic–Early Jurassic AFT ages to the closure of the PAO in the Permian and the subsequent collision of the Qiangtang Block with the Eurasian margin (e.g. Xiao et al. 2009, Glorie et al. 2010, De Grave et al. 2011, Macaulay et al. 2014, Glorie & De Grave 2016). During this period samples along the north-western margin of the Chatkal-Kurama terrane were rapidly cooled to surface temperatures. Thus, we interpret the Triassic–Early Jurassic fast

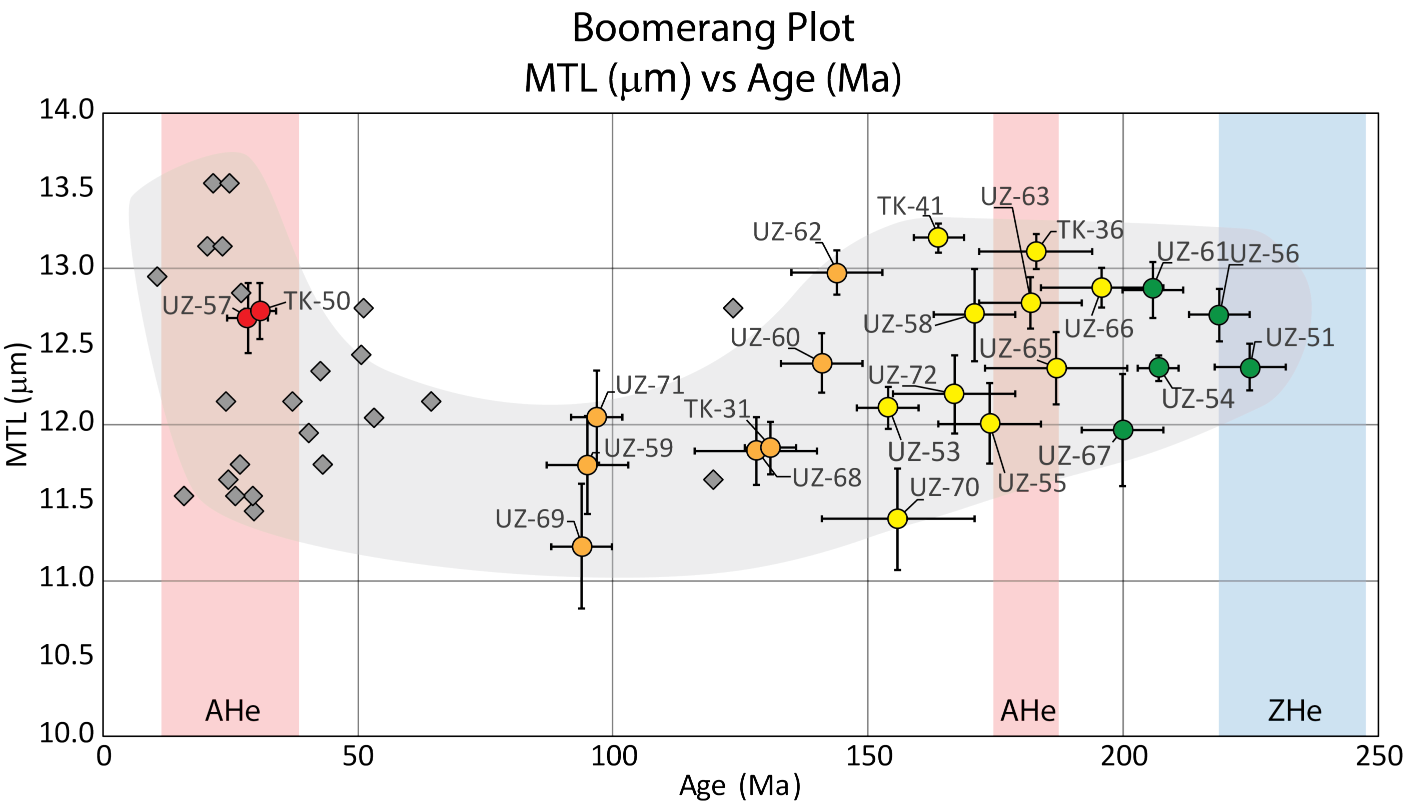

Figure 4: A 'boomerang' plot displaying apatite fission track (AFT) central age against mean track lengths (MTL). Circles denote AFT data obtained in this study, diamond symbols are data from (Bande et al. 2017b). Colour coding is the same as in previous figures and represents central AFT ages; green is Triassic, yellow is Jurassic, orange is Cretaceous, and red is Palaeogene. The x-axis error bars are the $\pm 1\sigma$ standard deviations, and the vertical error bars are standard errors of the mean. The red and blue shaded bars represent the age and $\pm 1\sigma$ uncertainties for the apatite helium (AHe), and zircon helium (ZHe) data obtained in this study, respectively. This plot highlights a period of fast cooling in the Triassic–Early Jurassic, followed by slow cooling in the Late Jurassic–Cretaceous, before showing a return to fast cooling in the Cenozoic.

cooling signal in our data to be related with exhumation associated with the closure of the PAO and/or the Qiangtang convergence in the Triassic–Early Jurassic.

5.2.2 Late Jurassic–Cretaceous

In the Chatkal-Kurama terrane, our data are indicative of protracted residence in the APAZ during the Late Jurassic–Early Cretaceous, suggesting that the Chatkal-Kurama terrane experienced a period of steady, slow denudation and tectonic quiescence at that time (Figure 3). In the Late Jurassic–Cretaceous thermotectonic quiescence induced planation and punctuated marine incursions of the Paratethyan Sea (Burov & Molnar 1998, Yablonskaya 2004, Bande et al. 2017a, De Pelsmaeker et al. 2018, Nachtergaele et al. 2017). These marine incursions deposited thick Jurassic and Cretaceous sedimentary sequences, conglomerates, and coal deposits (Ahmedov 2000, Dill et al. 2008).

5.2.3 Cenozoic

The presence of a Cenozoic fast cooling signal for the Chatkal-Kurama terrane (both in this study and Bande et al. (2017b)) is evident by overlapping ages for multiple thermochronometers (AFT and AHe), in combination with long MTLs and associated thermal history models (Figs. 3 and 4). Bande et al. (2017b) interprets this thermal event to deformation in the Chatkal-Kurama caused by the Cenozoic reactivation of the Talas-Fergana Fault (Sobel & Dumitru 1997). Similarly, the Cenozoic thermochronological ages identified in the south-eastern margin are likely in response to stresses from the reactivation of the Talas-Fergana Fault transmitting both along the TFF and the Fergana Basin into the Chatkal-Kurama terrane. This Cenozoic reactivation of the Chatkal-Kurama terrane likely provided a source for the thick Cenozoic sedimentary sequences identified in the nearby Fergana Basin (Ahmedov 2000, Bande et al. 2017b, De Pelsmaeker et al. 2018).

5.2.4 Regional trends for the western Tian Shan

The following section aims to integrate the thermochronological results obtained for the Chatkal-Kurama into the greater western Tian Shan thermo-tectonic history. In this study, we define the western Tian Shan as the section of the Tian Shan within the former Soviet Republics (Tajikistan, Uzbekistan, Kyrgyzstan, and Kazakhstan). The Mesozoic and Cenozoic thermo-tectonic evolution of the Chatkal-Kurama terrane is comparable to previous studies within the western Tian Shan (e.g. Sobel et al. 2006a, Glorie et al. 2011, De Grave et al. 2013, Käßner et al. 2017a), demonstrating that the western Tian Shan underwent a cyclical tectonic evolution of deformation, quiescence, and reactivation as a result of strain propagation from the Eurasian margin into the Central Asian interior.

The relationship between the tectonic history of the Chatkal-Kurama terrane and the western Tian Shan is demonstrated in Figure 5. Figure 5a represents a boomerang plot for all AFT age and length data obtained in the western Tian Shan (latitudinal and longitudinal constraints were placed at 40.000°N and 77.140°E, respectively), allowing for a direct comparison between the AFT age and length data of the Chatkal-Kurama terrane (west of the TFF) and Kyrgyz western Tian Shan (east of the TFF). The plot shows that both the Chatkal-Kurama terrane and the western Kyrgyz Tian Shan both experienced a phase of fast cooling in the Triassic–Early Jurassic. However, while the Chatkal-Kurama terrane experienced a period of tectonic stability during the Late Jurassic–Cretaceous (low MTL values), the Kyrgyz western

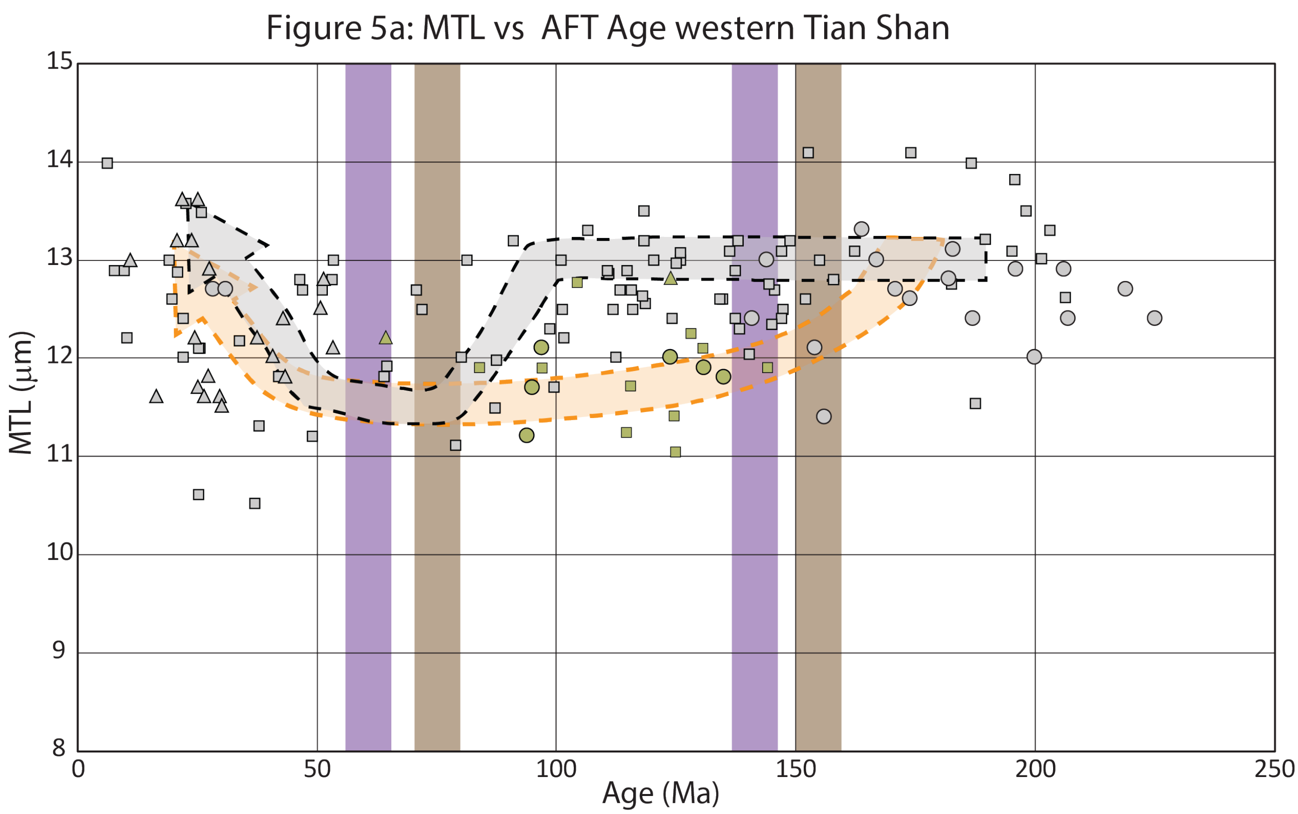

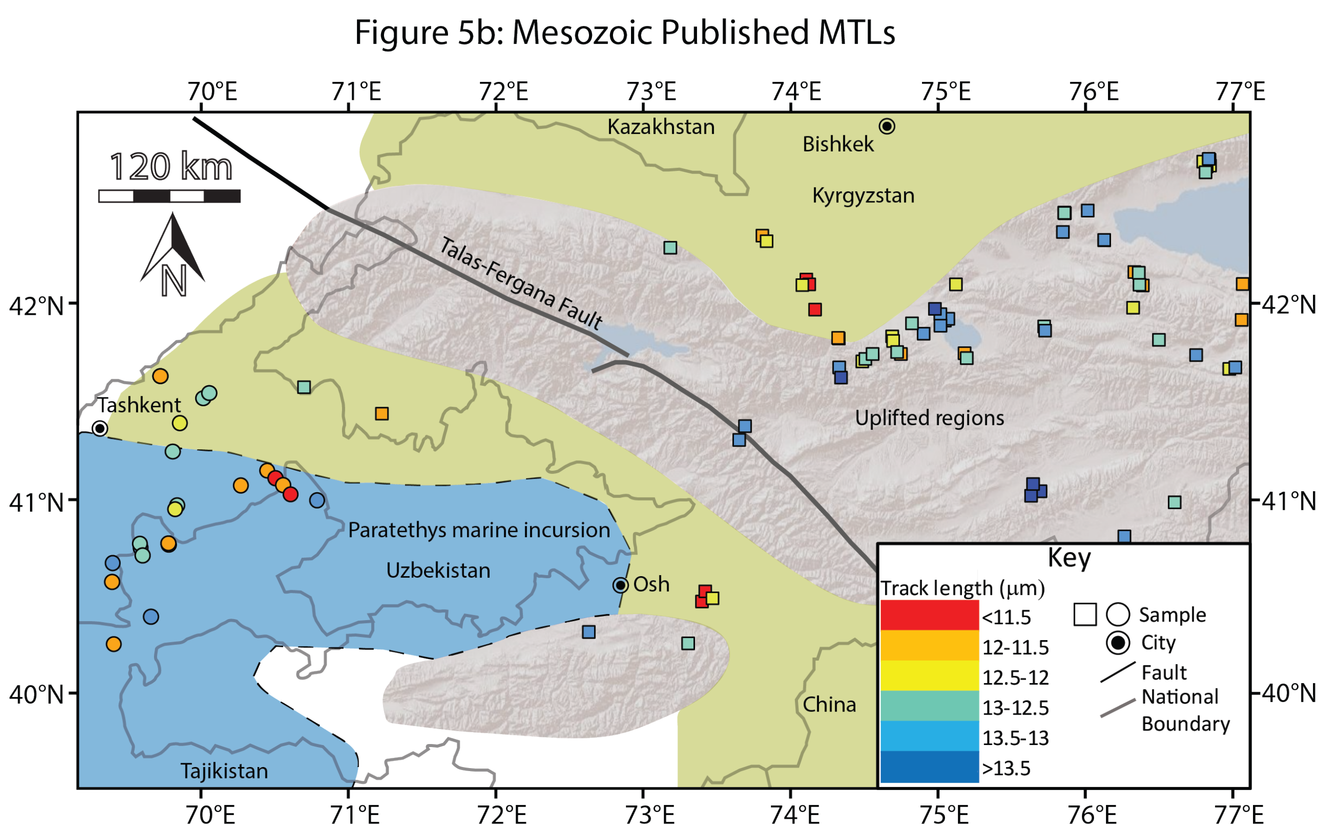

Figure 5: Caption next page

Figure 5: **Figure 5a:** A boomerang plot displaying apatite fission track (AFT) central age against mean track length (MTL) for the western Tian Shan. Circle symbols identify the samples obtained in this study, the triangles are from samples in (Bande et al. 2017b), and the squares represent data obtained from other published AFT data in the Tian Shan (Sobel et al. 2006a, Glorie et al. 2010, De Grave et al. 2011, Glorie et al. 2011, De Grave et al. 2012, 2013, Thiede et al. 2013, Bande et al. 2017a, Käßner et al. 2017b, Bande et al. 2017c, Nachtergaele et al. 2017). The colour code of the symbols denotes they samples location in Figure 5b. Green coloured coded symbols identify samples that were assessed to lie in marine-mountain transition zone, grey colour coded symbols identify samples that lie in the regions that lie in the mountainous zone. The brown shaded bars represent periods of conglomerate formation experienced in the Tian Shan. The purple shaded bars represent periods of planation identified the Tian Shan. **Figure 5b:** A map of the western extent of the Tian Shan displaying the mean track length (MTL) of published Mesozoic apatite fission track (AFT) data for the region, modified from (De Pelsmaeker et al. 2018). The higher abundance of MTLs to the east of the Talas-Fergana Fault (TFF) is an indication that the Kyrgyz Tian Shan experienced a longer period of deformation and exhumation during the Mesozoic, when compared to the Chatkal-Kurama terrane to the west of the TFF. Blue regions represent areas of marine incursion during the Mesozoic, green regions represent areas of marine-mountain transition, and the grey regions represent areas that were uplifted in the Mesozoic (after De Pelsmaeker et al. 2018). Circles represent data obtained by this study. Published AFT data are represented by squares, obtained from; Glorie et al. (2010), De Grave et al. (2011), Glorie et al. (2011), De Grave et al. (2012), De Grave et al. (2013), Macaulay et al. (2014), and De Pelsmaeker et al. (2018).

Tian Shan records prolonged fast cooling at that time (higher MTL values). From the Late Eocene–Early Oligocene, the western Tian Shan experienced the onset of renewed cooling as demonstrated by the increase in MTL values from corresponding Cenozoic AFT ages (Figure 5a).

The contrasting Mesozoic cooling histories on either side of the TFF are further explored in Figure 5b, which shows the geographical distribution of MTLs for the Mesozoic samples used in Figure 5a. The abundance of longer MTLs to the east of the TFF indicates that, during the Mesozoic, areas to the east of the Talas-Fergana fault experienced more rapid exhumation compared to the west (Figure 5b). Particularly in close vicinity to the TFF, new AFT results from the Kyrgyz Tian Shan are indicative of Late Jurassic–Early Cretaceous basement cooling and denudation at that time (Nachtergaele et al. 2017). To the west of the TFF, MTL values are lower, suggesting slow cooling and flattening of the pre-existing Mesozoic relief. Bande et al. (2017b) and De Pelsmaeker et al. (2018) suggest that during the Cretaceous much of the Chatkal-Kurama terrane was submerged by a marine incursion of the Paratethys Sea, while the North Tian Shan remained tectonically active. In this model, the Talas-Fergana Fault partitions strain from the Eurasian margin into the area to the east of the fault, causing deformation, while leaving the Chatkal-Kurama terrane relatively undeformed. Based on detrital zircon data, De Pelsmaeker et al. (2018) proposed a model for the palaeogeography of the western Tian Shan during the Late Jurassic–Early Cretaceous. The AFT data obtained in this study fits very well with this model and strengthen the hypothesis that the TFF acted as a topographic divide between the high eastern and low western Tian Shan during the Cretaceous. A slight modification to the original model was made to accommodate for the shorter MTLs near the northern margin of the Kyrgyz Tian Shan (Suusamyr valley, Glorie et al. 2010) and near the Kyrgyz Chatkal Ranges south-eastern piedmonts (Bande et al. 2017b). As shown, the regions that record relatively short MTLs were covered by the marine incursion of the Paratethys or are located within a transitional zone during the Late Jurassic–Early Cretaceous, while high relief maintained to the east of the TFF (Figure 5b).

Given the widespread occurrence of a Late Jurassic conglomerate deposits in the Tarim and Junggar basins, the fast, Late Jurassic cooling signal in the Kyrgyz Tian Shan is attributed to exhumation and denudation (Figure 5a Dumitru et al. 2001, Jolivet et al. 2013, Glorie & De Grave 2016). The contrast between slow cooling, tectonic stability in the Chatkal-Kurama terrane and fast cooling, tectonic activity in the Kyrgyz western Tian Shan (west of the TFF) continues through to the end of the early Cretaceous. During the late Cretaceous and early Palaeogene, then entire western Tian Shan records slow cooling or tectonic quiescence, leading to the development of widespread planation surfaces (e.g. Bazhenov et al. 1993, Burbank et al. 1999, Glorie et al. 2010, Jolivet et al. 2013).

The collision of India with Eurasia and the subsequent Pamir indentation during the Cenozoic marked the end of this period of tectonic stability (e.g. Schwab et al. 2004, Kapp et al. 2007). The stress from these Cenozoic collisions partitioned strain into the continental interior of Eurasia via major faults (Sobel et al. 2006a, Glorie et al. 2010). These collisions continued to be the dominant control on the reactivation and exhumation that has been identified throughout the Tian Shan and the Chatkal-Kurama terrane in the Cenozoic (Figure 5a, e.g. De Grave et al. 2012, Macaulay et al. 2014, Bande et al. 2017b, Käßner et al. 2017b, Bande et al. 2017c). Within our study area, fast Cenozoic cooling was revealed for the south-eastern margin of the Chatkal-Kurama terrane (Samples TK-49, TK-50, and UZ-69), which induced crustal tilting and fault reactivation. This observation is in good agreement with other studies that describe reactivation and deformation since ~30-20 Ma, with a significant increase across the Tian Shan in the last ~10 Ma (Sobel & Dumitru 1997, Sobel et al. 2006a,b, Glorie et al. 2010, De Grave et al. 2011, Glorie et al. 2011, De Grave et al. 2013, Macaulay et al. 2014, Käßner et al. 2017b, Bande et al. 2017c, Jepson et al. 2018).

6 Conclusion

Based on the thermochronological results and modelling presented in this study, the following conclusions can be drawn for the thermotectonic evolution of the Chatkal-Kurama terrane:

- The Chatkal-Kurama terrane records fast cooling during the Triassic–Early Jurassic (~ 225–180 Ma) as a result of the Palaeo-Asian Ocean and the Qiangtang collision at the Eurasian margin. Subsequently, slow cooling and tectonic quiescence prevailed during the Late Jurassic–Early Cretaceous, leading to widespread denudation and marine incursion of the Paratethys.
- Since the late Palaeogene (~30 Ma), the Chatkal-Kurama terrane experienced reactivation and crustal tilting to the north-west, as a distant response to the collision of India and Eurasia and the subsequent Pamir indentation.
- Comparing our results with the neighbouring Kyrgyz western Tian Shan, the Talas-Fergana faults seemed to have acted as a structural divide, separating the low relief Chatkal-Kurama terrane from the high relief Kyrgyz Tian Shan during the late Mesozoic.

7 Acknowledgements

We are grateful to Farid Divaev, Vladimir Chirikin and Yunus Mamjanov, who were responsible for logistics and transportation in the field. As well as Andy Gleadow at the University of Melbourne for use of their Cf source. This study was supported by an Australian Research Council Discovery grant (DP150101730). D. Konopelko was supported by the Ministry of Education and Science of the Russian Federation (project No 14.Y26.31.0018) and by travel grant 3.42.731.2017 from Saint Petersburg State University. Ben Wade and Sarah Gilbert are thanked for assistance with the LA-ICP-MS facility. This paper forms TRaX record #XXX.

References

Ahmedov, N. (2000), 'Stratified and intrusive formations of Uzbekistan', *Uzbekistan Geological Survey* .

Aitchison, J. C., Ali, J. R. & Davis, A. M. (2007), 'When and where did India and Asia collide?', *Journal of Geophysical Research: Solid Earth* **112**(B5).
URL: *https://agupubs.onlinelibrary.wiley.com/doi/abs/10.1029/2006JB004706*

Alexeiev, D., Kröner, A., Hegner, E., Rojas-Agramonte, Y., Biske, Y., Wong, J., Geng, H., Ivleva, E., Mühlberg, M., Mikolaichuk, A. & Liu, D. (2016), 'Middle to Late Ordovician arc system in the Kyrgyz Middle Tianshan: From arc-continent collision to subsequent evolution of a Palaeozoic continental margin', *Gondwana Research* **39**, 261 – 291.

URL: *http://www.sciencedirect.com/science/article/pii/S1342937X16300065*

Allen, M. B., Windley, B. F., Chi, Z., Zhong-Yan, Z. & Guang-Rei, W. (1991), 'Basin evolution within and adjacent to the Tien Shan Range, NW China', *Journal of the Geological Society* **148**(2), 369–378.

URL: *http://jgs.lyellcollection.org/content/148/2/369*

Bande, A., Radjabov, S., Sobel, E. R. & Sim, T. (2017a), 'Cenozoic palaeoenvironmental and tectonic controls on the evolution of the northern fergana basin', *Geological Society, London, Special Publications* **427**(1), 313–335.

URL: *http://sp.lyellcollection.org/content/427/1/313*

Bande, A., Sobel, E. R., Mikolaichuk, A., Schmidt, A. & Stockli, D. F. (2017c), 'Exhumation history of the western kyrgyz tien shan: Implications for intramontane basin formation', *Tectonics* **36**(1), 163–180.

URL: *https://agupubs.onlinelibrary.wiley.com/doi/abs/10.1002/2016TC004284*

Bande, A., Sobel, E. R., Mikolaichuk, A. & Torres, A. V. (2017b), 'Talas–Fergana Fault Cenozoic timing of deformation and its relation to Pamir indentation', *Geological Society, London, Special Publications* **427**(1), 295–311.

URL: *http://sp.lyellcollection.org/content/427/1/295*

Bazhenov, M. L., Chauvin, A., Audibert, M. & Levashova, N. (1993), 'Permian and Triassic paleomagnetism of the southwestern Tien Shan: timing and mode of tectonic rotations', *Earth and Planetary Science Letters* **118**(1), 195 – 212.

URL: *http://www.sciencedirect.com/science/article/pii/0012821X93901689*

Biske, Y. & Seltmann, R. (2010), 'Paleozoic Tian-Shan as a transitional region between the Rheic and Urals-Turkestan oceans', *Gondwana Research* **17**(2), 602 – 613. The Rheic Ocean: Palaeozoic Evolution from Gondwana and Laurussia to Pangaea.

URL: *http://www.sciencedirect.com/science/article/pii/S1342937X09002160*

Bouilhol, P., Jagoutz, O., Hanchar, J. M. & Dudas, F. O. (2013), 'Dating the India–Eurasia collision through arc magmatic records', *Earth and Planetary Science Letters* **366**, 163 – 175.
URL: *http://www.sciencedirect.com/science/article/pii/S0012821X1300040X*

Burbank, D., McLean, J., Bullen, M., Abdrakhmatov, K. & Miller, M. (1999), 'Partitioning of intermontane basins by thrust-related folding, Tien Shan, Kyrgyzstan', *Basin Research* **11**(1), 75–92.

Burov, E. B. & Molnar, P. (1998), 'Gravity anomalies over the Ferghana Valley (central Asia) and intracontinental deformation', *Journal of Geophysical Research: Solid Earth* **103**(B8), 18137–18152.
URL: *https://agupubs.onlinelibrary.wiley.com/doi/abs/10.1029/98JB01079*

Burtman, V. S. (2015), 'Tectonics and geodynamics of the Tian Shan in the Middle and Late Paleozoic', *Geotectonics* **49**(4), 302–319.
URL: *https://doi.org/10.1134/S0016852115040020*

Burtman, V. S., Skobelev, S. F. & Molnar, P. (1996), 'Late Cenozoic slip on the Talas-Ferghana fault, the Tien Shan, central Asia', *GSA Bulletin* **108**(8), 1004.
URL: *http://dx.doi.org/10.1130/0016-7606(1996)108<1004:LCSOTT>2.3.CO;2*

Clift, P. D., Carter, A., Krol, M. & Kirby, E. (2002), 'Constraints on India-Eurasia collision in the Arabian Sea region taken from the Indus Group, Ladakh Himalaya, India', *Geological Society, London, Special Publications* **195**(1), 97–116.
URL: *http://sp.lyellcollection.org/content/195/1/97*

Danišík, M., Štěpančíková, P. & Evans, N. J. (2012), 'Constraining long-term denudation and faulting history in intraplate regions by multisystem thermochronology: An example of the Sudetic Marginal Fault (Bohemian Massif, central Europe)', *Tectonics* **31**(2).
URL: *https://agupubs.onlinelibrary.wiley.com/doi/abs/10.1029/2011TC003012*

De Grave, J., Buslov, M. M. & Van den haute, P. (2007), 'Distant effects of India–Eurasia convergence and Mesozoic intracontinental deformation in Central Asia: Constraints from apatite fission-track thermochronology', *Journal of Asian Earth Sciences* **29**(2), 188 – 204. The 19th Himalaya-Karakoram-Tibet Workshop (HKT19) held at Niseko, Hokkaido, Japan, 10–13 July 2004.
URL: *http://www.sciencedirect.com/science/article/pii/S136791200600071X*

De Grave, J., Glorie, S., Buslov, M. M., Izmer, A., Fournier-Carrie, A., Batalev, V. Y., Vanhaecke, F., Elburg, M. & Van den haute, P. (2011), 'The thermo-tectonic history of the Song-Kul plateau, Kyrgyz Tien Shan: Constraints by apatite and titanite thermochronometry and zircon U/Pb dating', *Gondwana Research* **20**(4), 745 – 763.

URL: *http://www.sciencedirect.com/science/article/pii/S1342937X11001201*

De Grave, J., Glorie, S., Buslov, M. M., Stockli, D. F., McWilliams, M. O., Batalev, V. Y. & Van den haute, P. (2013), 'Thermo-tectonic history of the Issyk-Kul basement (Kyrgyz Northern Tien Shan, Central Asia)', *Gondwana Research* **23**(3), 998 – 1020. Ultrahigh-pressure and high-pressure metamorphic terranes in orogenic belts: reactions, fluids and geological processes.

URL: *http://www.sciencedirect.com/science/article/pii/S1342937X12002377*

De Grave, J., Glorie, S., Ryabinin, A., Zhimulev, F., Buslov, M., Izmer, A., Elburg, M., Vanhaecke, F. & Van den haute, P. (2012), 'Late Palaeozoic and Meso-Cenozoic tectonic evolution of the southern Kyrgyz Tien Shan: Constraints from multi-method thermochronology in the Trans-Alai, Turkestan-Alai segment and the southeastern Ferghana Basin', *Journal of Asian Earth Sciences* **44**, 149 – 168. Asian Climate and Tectonics.

URL: *http://www.sciencedirect.com/science/article/pii/S1367912011001866*

De Pelsmaeker, E., Glorie, S., Buslov, M. M., Zhimulev, F. I., Poujol, M., Korobkin, V. V., Vanhaecke, F., Vetrov, E. V. & De Grave, J. (2015), 'Late-Paleozoic emplacement and Meso-Cenozoic reactivation of the southern Kazakhstan granitoid basement', *Tectonophysics* **662**, 416 – 433. Special issue on Comparative tectonic and dynamic analysis of cratons, orogens, basins, and metallogeny:.

URL: *https://www.sciencedirect.com/science/article/pii/S0040195115003091*

De Pelsmaeker, E., Jolivet, M., Laborde, A., Poujol, M., Robin, C., Zhimulev, F. I., Nachtergaele, S., Glorie, S., Clercq, S. D., Batalev, V. Y. & Grave, J. D. (2018), 'Source-to-sink dynamics in the Kyrgyz Tien Shan from the Jurassic to the Paleogene: Insights from sedimentological and detrital zircon U-Pb analyses', *Gondwana Research* **54**, 180 – 204.

URL: *http://www.sciencedirect.com/science/article/pii/S1342937X17300679*

Dill, H., Kus, J., Dohrmann, R. & Tsoy, Y. (2008), 'Supergene and hypogene alteration in the dual-use kaolin-bearing coal deposit Angren, SE Uzbekistan', *International Journal of Coal Geology* **75**(4), 225

– 240.

URL: *http://www.sciencedirect.com/science/article/pii/S0166516208001328*

Dolgopolova, A., Seltmann, R., Konopelko, D., Biske, Y. S., Shatov, V., Armstrong, R., Belousova, E., Pankhurst, R., Koneev, R. & Divaev, F. (2017), 'Geodynamic evolution of the western tien shan, uzbekistan: Insights from u-pb shrimp geochronology and sr-nd-pb-hf isotope mapping of granitoids', *Gondwana Research* **47**, 76 – 109. Continental construction in Central Asia and actualistic comparisons with western Pacific.

URL: *http://www.sciencedirect.com/science/article/pii/S1342937X16304324*

Donelick, R. A. & Miller, D. S. (1991), 'Enhanced tint fission track densities in low spontaneous track density apatites using 252Cf-derived fission fragment tracks: A model and experimental observations', *International Journal of Radiation Applications and Instrumentation. Part D. Nuclear Tracks and Radiation Measurements* **18**(3), 301 – 307.

URL: *http://www.sciencedirect.com/science/article/pii/135901899190022A*

Donelick, R. A., O'Sullivan, P. B. & Ketcham, R. A. (2005), 'Apatite Fission-Track Analysis', *Reviews in Mineralogy and Geochemistry* **58**(1), 49.

URL: *http://dx.doi.org/10.2138/rmg.2005.58.3*

Dumitru, T. A., Zhou, D., Chang, E. Z., Graham, S. A., Hendrix, M. S., Sobel, E. R. & Carroll, A. R. (2001), 'Uplift, exhumation, and deformation in the Chinese Tian Shan', *Memoirs-Geological Society of America* pp. 71–100.

Farley, K. A. (2002), '(U-Th)/He Dating: Techniques, Calibrations, and Applications', *Reviews in Mineralogy and Geochemistry* **47**(1), 819.

URL: *http://dx.doi.org/10.2138/rmg.2002.47.18*

Farley, K., Wolf, R. & Silver, L. (1996), 'The effects of long alpha-stopping distances on (U-Th)/He ages', *Geochimica et Cosmochimica Acta* **60**(21), 4223 – 4229.

URL: *http://www.sciencedirect.com/science/article/pii/S0016703796001937*

Gallagher, K. (2012), 'Transdimensional inverse thermal history modeling for quantitative thermochronology', *Journal of Geophysical Research: Solid Earth* **117**(B2).

URL: *https://agupubs.onlinelibrary.wiley.com/doi/abs/10.1029/2011JB008825*

Gillespie, J., Glorie, S., Jepson, G., Zhang, Z. Y., Xiao, W. J., Danišík, M. & Collins, A. S. (2017), 'Differential Exhumation and Crustal Tilting in the Easternmost Tianshan (Xinjiang, China), Revealed by Low-Temperature Thermochronology', *Tectonics* **36**(10), 2142–2158.
URL: *https://agupubs.onlinelibrary.wiley.com/doi/abs/10.1002/2017TC004574*

Glorie, S., Alexandrov, I., Nixon, A., Jepson, G., Gillespie, J. & Jahn, B.-M. (2017), 'Thermal and exhumation history of Sakhalin Island (Russia) constrained by apatite U-Pb and fission track thermochronology', *Journal of Asian Earth Sciences* **143**, 326 – 342.
URL: *http://www.sciencedirect.com/science/article/pii/S1367912017302262*

Glorie, S. & De Grave, J. (2016), 'Exhuming the Meso–Cenozoic Kyrgyz Tianshan and Siberian Altai-Sayan: A review based on low-temperature thermochronology', *Geoscience Frontiers* **7**(2), 155 – 170. Special Issue: Exhuming Asia.
URL: *https://www.sciencedirect.com/science/article/pii/S1674987115000468*

Glorie, S., De Grave, J., Buslov, M., Elburg, M., Stockli, D., Gerdes, A. & Van den haute, P. (2010), 'Multi-method chronometric constraints on the evolution of the Northern Kyrgyz Tien Shan granitoids (Central Asian Orogenic Belt): From emplacement to exhumation', *Journal of Asian Earth Sciences* **38**(3), 131 – 146.
URL: *http://www.sciencedirect.com/science/article/pii/S1367912009002636*

Glorie, S., Grave, J. D., Buslov, M. M., Zhimulev, F. I., Stockli, D. F., Batalev, V. Y., Izmer, A., Van den haute, P., Vanhaecke, F. & Elburg, M. A. (2011), 'Tectonic history of the Kyrgyz South Tien Shan (Atbashi-Inylchek) suture zone: The role of inherited structures during deformation-propagation', *Tectonics* **30**(6).
URL: *https://agupubs.onlinelibrary.wiley.com/doi/abs/10.1029/2011TC002949*

Green, P., Duddy, I., Gleadow, A., Tingate, P. & Laslett, G. (1986), 'Thermal annealing of fission tracks in apatite: 1. A qualitative description', *Chemical Geology: Isotope Geoscience section* **59**, 237 – 253. Calibration of the Phanerozoic Time Scale.
URL: *http://www.sciencedirect.com/science/article/pii/0168962286900746*

Green, P. F. (1986), 'On the thermo-tectonic evolution of Northern England: evidence from fission track analysis', *Geological Magazine* **123**(5), 493–506.

Guenthner, W. R., Reiners, P. W., Ketcham, R. A., Nasdala, L. & Giester, G. (2013), 'Helium diffusion in natural zircon: Radiation damage, anisotropy, and the interpretation of zircon (U-Th)/He thermochronology', *American Journal of Science* **313**(3), 145–198.
URL: *http://www.ajsonline.org/content/313/3/145.abstract*

Hasebe, N., Barbarand, J., Jarvis, K., Carter, A. & Hurford, A. J. (2004), 'Apatite fission-track chronometry using laser ablation ICP-MS', *Chemical Geology* **207**(3), 135 – 145.
URL: *http://www.sciencedirect.com/science/article/pii/S0009254104000427*

Hendrix, M. S., Graham, S. A., Carroll, A. R., Sobel, E. R., McKnight, C. L., Schulein, B. J. & Wang, Z. (1992), 'Sedimentary record and climatic implications of recurrent deformation in the Tian Shan: Evidence from Mesozoic strata of the north Tarim, south Junggar, and Turpan basins, northwest China', *GSA Bulletin* **104**(1), 53.
URL: *http://dx.doi.org/10.1130/0016-7606(1992)104<0053:SRACIO>2.3.CO;2*

Jepson, G., Glorie, S., Konopelko, D., Gillespie, J., Danišík, M., Evans, N. J., Mamadjanov, Y. & Collins, A. S. (2018), 'Thermochronological insights into the structural contact between the Tian Shan and Pamirs, Tajikistan', *Terra Nova* **30**(2), 95–104.
URL: *https://onlinelibrary.wiley.com/doi/abs/10.1111/ter.12313*

Jolivet, M., Heilbronn, G., Robin, C., Barrier, L., Bourquin, S., Guo, Z., Jia, Y., Guerit, L., Yang, W. & Fu, B. (2013), 'Reconstructing the Late Palaeozoic - Mesozoic topographic evolution of the Chinese Tian Shan: available data and remaining uncertainties', *Advances in Geosciences* **37**, 7–18.
URL: *https://hal-insu.archives-ouvertes.fr/insu-00920043*

Kapp, P., DeCelles, P. G., Gehrels, G. E., Heizler, M. & Ding, L. (2007), 'Geological records of the Lhasa-Qiangtang and Indo-Asian collisions in the Nima area of central Tibet', *GSA Bulletin* **119**(7-8), 917.
URL: *http://dx.doi.org/10.1130/B26033.1*

Käßner, A., Ratschbacher, L., Jonckheere, R., Enkelmann, E., Khan, J., Sonntag, B., Gloaguen, R., Gadoev, M. & Oimahmadov, I. (2017b), 'Cenozoic intracontinental deformation and exhumation at the northwestern tip of the India-Asia collision—southwestern Tian Shan, Tajikistan, and Kyrgyzstan', *Tectonics* **35**(9), 2171–2194.
URL: *https://agupubs.onlinelibrary.wiley.com/doi/abs/10.1002/2015TC003897*

Käßner, A., Ratschbacher, L., Pfänder, J. A., Hacker, B. R., Zack, G., Sonntag, B.-L., Khan, J., Stanek, K. P., Gadoev, M. & Oimahmadov, I. (2017a), 'Proterozoic–Mesozoic history of the Central Asian orogenic belt in the Tajik and southwestern Kyrgyz Tian Shan: U-Pb, $^{40}Ar/^{39}Ar$, and fission-track geochronology and geochemistry of granitoids', *GSA Bulletin* **129**(3-4), 281.
URL: *http://dx.doi.org/10.1130/B31466.1*

Konopelko, D., Klemd, R., Petrov, S., Apayarov, F., Nazaraliev, B., Vokueva, O., Scherstén, A. & Sergeev, S. (2017), 'Precambrian gold mineralization at Djamgyr in the Kyrgyz Tien Shan: Tectonic and metallogenic implications', *Ore Geology Reviews* **86**, 537 – 547.
URL: *http://www.sciencedirect.com/science/article/pii/S0169136816306746*

Konopelko, D., Seltmann, R., Mamadjanov, Y., Romer, R., Rojas-Agramonte, Y., Jeffries, T., Fidaev, D. & Niyozov, A. (2017), 'A geotraverse across two paleo-subduction zones in Tien Shan, Tajikistan', *Gondwana Research* **47**, 110 – 130. Continental construction in Central Asia and actualistic comparisons with western Pacific.
URL: *http://www.sciencedirect.com/science/article/pii/S1342937X16302878*

Li, S., Chung, S.-L., Wilde, S. A., Wang, T., Xiao, W.-J. & Guo, Q.-Q. (2016), 'Linking magmatism with collision in an accretionary orogen', *Scientific reports* **6**, 25751.

Macaulay, E. A., Sobel, E. R., Mikolaichuk, A., Kohn, B. & Stuart, F. M. (2014), 'Cenozoic deformation and exhumation history of the Central Kyrgyz Tien Shan', *Tectonics* **33**(2), 135–165.
URL: *https://agupubs.onlinelibrary.wiley.com/doi/abs/10.1002/2013TC003376*

McDowell, F. W., McIntosh, W. C. & Farley, K. A. (2005), 'A precise 40Ar–39Ar reference age for the Durango apatite (U–Th)/He and fission-track dating standard', *Chemical Geology* **214**(3), 249 – 263.
URL: *http://www.sciencedirect.com/science/article/pii/S0009254104004218*

Molnar, P. & Tapponnier, P. (1975), 'Cenozoic tectonics of Asia: effects of a continental collision', *Science* **189**(4201), 419–426.

Nachtergaele, S., De Pelsmaeker, E., Glorie, S., Zhimulev, F., Jolivet, M., Danišík, M., Buslov, M. M. & De Grave, J. (2017), 'Meso-Cenozoic tectonic evolution of the Talas-Fergana region of the Kyrgyz Tien Shan revealed by low-temperature basement and detrital thermochronology', *Geoscience Frontiers* .
URL: *http://www.sciencedirect.com/science/article/pii/S1674987117302013*

Paton, C., Hellstrom, J., Paul, B., Woodhead, J. & Hergt, J. (2011), 'Iolite: Freeware for the visualisation and processing of mass spectrometric data', *Journal of Analytical Atomic Spectrometry* **26**(12), 2508–2518.

Ratschbacher, L., Hacker, B. R., Calvert, A., Webb, L. E., Grimmer, J. C., McWilliams, M. O., Ireland, T., Dong, S. & Hu, J. (2003), 'Tectonics of the Qinling (Central China): tectonostratigraphy, geochronology, and deformation history', *Tectonophysics* **366**(1), 1 – 53.
URL: *http://www.sciencedirect.com/science/article/pii/S0040195103000532*

Reiners, P. W. (2005), 'Zircon (u-th)/he thermochronometry', *Reviews in Mineralogy and Geochemistry* **58**(1), 151.
URL: *http://dx.doi.org/10.2138/rmg.2005.58.6*

Reiners, P. W., Farley, K. A. & Hickes, H. J. (2002), 'He diffusion and (U–Th)/He thermochronometry of zircon: initial results from Fish Canyon Tuff and Gold Butte', *Tectonophysics* **349**(1), 297 – 308. Low Temperature Thermochronology: From Tectonics to Landscape Evolution.
URL: *http://www.sciencedirect.com/science/article/pii/S0040195102000586*

Robinson, A. C. (2015), 'Mesozoic tectonics of the Gondwanan terranes of the Pamir plateau', *Journal of Asian Earth Sciences* **102**, 170 – 179. Special Issue on CIMMERIAN TERRANES.
URL: *http://www.sciencedirect.com/science/article/pii/S1367912014004258*

Samygin, S. G. & Burtman, V. S. (2009), 'Tectonics of the Ural paleozoides in comparison with the Tien Shan', *Geotectonics* **43**(2), 133–151.
URL: *https://doi.org/10.1134/S0016852109020058*

Schwab, M., Lothar, R., Wolfgang, S., Michael, M., Vladislav, M., Valery, L., Fokun, C., Klaus, S., Bruce, N., Wolfgang, F. & L., W. J. (2004), 'Assembly of the Pamirs: Age and origin of magmatic belts from the southern Tien Shan to the southern Pamirs and their relation to Tibet', *Tectonics* **23**(4).
URL: *https://agupubs.onlinelibrary.wiley.com/doi/abs/10.1029/2003TC001583*

Seltmann, R., Konopelko, D., Biske, G., Divaev, F. & Sergeev, S. (2011), 'Hercynian post-collisional magmatism in the context of Paleozoic magmatic evolution of the Tien Shan orogenic belt', *Journal of Asian Earth Sciences* **42**(5), 821 – 838. Continental accretion and intra-continental deformation of the Central Asian Orogenic Belt.
URL: *http://www.sciencedirect.com/science/article/pii/S1367912010002646*

Seltmann, R. & Porter, T. M. (2005), 'The porphyry Cu–Au/Mo deposits of Central Eurasia: 1. Tectonic, geologic and metallogenic setting and significant deposits', *Super porphyry copper and gold deposits: a global perspective* **2**, 467–512.

Sobel, E. R., Chen, J. & Heermance, R. V. (2006a), 'Late Oligocene–Early Miocene initiation of shortening in the Southwestern Chinese Tian Shan: Implications for Neogene shortening rate variations', *Earth and Planetary Science Letters* **247**(1), 70 – 81.
URL: *http://www.sciencedirect.com/science/article/pii/S0012821X06002834*

Sobel, E. R. & Dumitru, T. A. (1997), 'Thrusting and exhumation around the margins of the western Tarim basin during the India-Asia collision', *Journal of Geophysical Research: Solid Earth* **102**(B3), 5043–5063.
URL: *http://dx.doi.org/10.1029/96JB03267*

Sobel, E. R., Oskin, M., Burbank, D. & Mikolaichuk, A. (2006b), 'Exhumation of basement-cored uplifts: Example of the Kyrgyz Range quantified with apatite fission track thermochronology', *Tectonics* **25**(2). TC2008.
URL: *http://dx.doi.org/10.1029/2005TC001809*

Thiede, R. C., R., S. E., Jie, C., M., S. L., F., S. D., Masafumi, S. & R., S. M. (2013), 'Late Cenozoic extension and crustal doming in the India-Eurasia collision zone: New thermochronologic constraints from the NE Chinese Pamir', *Tectonics* **32**(3), 763–779.
URL: *https://agupubs.onlinelibrary.wiley.com/doi/abs/10.1002/tect.20050*

Vermeesch, P. (2009), 'RadialPlotter: A Java application for fission track, luminescence and other radial plots', *Radiation Measurements* **44**(4), 409–410.

Vermeesch, P. (2017), 'Statistics for LA-ICP-MS based fission track dating', *Chemical Geology* **456**, 19 – 27.
URL: *http://www.sciencedirect.com/science/article/pii/S0009254117301158*

Wagner, G. & Van den Haute, P. (1992), *Fission-track dating*, Vol. 6, Springer Science & Business Media.

Windley, B. F., Alexeiev, D., Xiao, W., Kröner, A. & Badarch, G. (2007), 'Tectonic models for accretion of the Central Asian Orogenic Belt', *Journal of the Geological Society* **164**(1), 31.
URL: *http://dx.doi.org/10.1144/0016-76492006-022*

Xiao, W. J., Windley, B. F., Huang, B. C., Han, C. M., Yuan, C., Chen, H. L., Sun, M., Sun, S. & Li, J. L. (2009), 'End-Permian to mid-Triassic termination of the accretionary processes of the southern Altaids: implications for the geodynamic evolution, Phanerozoic continental growth, and metallogeny of Central Asia', *International Journal of Earth Sciences* **98**(6), 1189–1217.
URL: *https://doi.org/10.1007/s00531-008-0407-z*

Xiao, W., Windley, B. F., Allen, M. B. & Han, C. (2013), 'Paleozoic multiple accretionary and collisional tectonics of the Chinese Tianshan orogenic collage', *Gondwana Research* **23**(4), 1316 – 1341.
URL: *http://www.sciencedirect.com/science/article/pii/S1342937X12000469*

Yablonskaya, N. A. (2004), 'Alpine tectonics of tien shan and central kyzylkum', *Thesis; In Russian, Unpublished* p. Tashkent.

Zeitler, P., Herczeg, A., McDougall, I. & Honda, M. (1987), 'U-Th-He dating of apatite: A potential thermochronometer', *Geochimica et Cosmochimica Acta* **51**(10), 2865 – 2868.
URL: *http://www.sciencedirect.com/science/article/pii/0016703787901645*

8 Supplementary Files

8.1 Supplementary File 1: Apatite Fission Track

Supplemtary File 1: Apatite fission track data and chemistry: ρ_s is the density of spontaneous tracks within the region of interest and is expressed as 10^5 tracks/cm^2. N_s is the total number of counted spontaneous tracks per sample. ^{238}U is the average concentration in ppm of uranium 238 measured in each grain. ^{35}Cl is the average concentration in ppm of chlorine 35 measured in each grain; concentrations were obtained using laser ablation–inductively coupled plasma–mass spectrometry (LA-ICP-MS). BLOD is below limits of detection, and thus, could not provide a concentration value and was not used in calculating sample concentration averages. Dpar is the length of spontaneous track etch pits in μm. t is the AFT single grain age for each sample in Ma.

Sample	ρ_s	N_s	^{238}U	$\pm 1\sigma$	^{35}Cl	$\pm 1\sigma$	Dpar	$\pm 1\sigma$	t	$\pm 1\sigma$
UZ-51-1	10.9	29	6.8	0.5	2390	380	3.3	0.7	223.6	45.0
UZ-51-2	8.2	17	9.4	1.2	2700	500	3.1	0.5	191.1	52.4
UZ-51-3	47.5	160	64.1	4.4	9820	670	3.4	0.4	161.6	16.9
UZ-51-4	13.4	53	16.5	1.1	2850	490	2.1	0.2	176.8	27.0
UZ-51-5	10.3	31	8.9	0.5	3150	430	2.2	1.3	251.6	47.1
UZ-51-6	12.0	36	12.5	0.8	3930	320	2.6	0.6	208.7	37.4

UZ-51-7	4.7	15	6.8	0.5	3280	750	2.9	0.3	151.6	40.9
UZ-51-8	58.4	185	63.3	5.7	11190	680	2.0	0.2	200.6	23.3
UZ-51-9	6.3	14	9.3	0.7	3120	450	1.5	0.2	148.5	41.2
UZ-51-10	13.2	34	9.4	0.4	4680	550	3.2	0.3	301.4	53.0
UZ-51-11	49.8	130	46.8	2.5	11710	820	3.9	0.5	231.0	23.7
UZ-51-12	50.1	154	60.0	4.2	10960	770	2.0	1.1	182.1	19.4
UZ-51-13	20.1	87	13.6	0.7	2120	430	2.3	1.0	318.4	38.1
UZ-51-14	24.3	82	17.4	1.0	5090	550	1.2	0.1	301.6	37.3
UZ-51-15	3.5	7	9.0	0.4	4540	760	3.0	0.4	84.8	32.2
UZ-51-16	6.4	19	5.4	0.3	3410	590	3.0	0.3	256.6	61.0
UZ-51-17	19.8	81	17.9	0.9	4420	500	2.5	0.9	239.4	29.3
UZ-51-18	40.8	169	36.6	1.9	4520	430	1.4	0.4	241.9	22.4
UZ-51-19	5.7	18	8.2	0.4	4890	530	1.7	0.7	152.4	36.8
UZ-51-20	28.0	53	12.6	0.6	1070	440	1.7	0.8	271.1	39.7
UZ-51-21	7.4	18	42.8	2.3	5930	460	2.2	0.9	38.1	9.2
UZ-51-22	13.7	23	4.9	0.3	6540	420	2.5	0.8	271.5	59.1
UZ-51-23	5.6	17	18.4	2.3	4280	520	2.2	0.7	67.0	18.3
UZ-51-24	10.8	16	6.7	0.4	4530	530	2.2	0.5	215.9	55.8
UZ-51-25	17.9	26	8.1	0.6	4680	440	2.4	0.5	138.9	29.2
UZ-51-26	9.1	21	6.5	0.4	4340	770	2.0	0.8	300.1	68.3
UZ-51-27	15.5	30	32.4	2.0	6350	550	2.0	0.7	85.0	16.4
UZ-51-28	41.1	105	32.8	2.3	17300	1000	1.7	0.6	271.6	32.6
UZ-51-29	4.2	11	39.6	2.2	15230	890	2.1	0.7	23.4	7.2
UZ-51-30	9.7	24	34.1	2.4	16990	890	2.1	0.7	62.4	13.5
UZ-51-31	4.2	9	55.9	3.1	17900	1300	2.0	1.0	16.8	5.7
UZ-51-32	8.3	8	5.3	0.3	3670	900	1.8	0.7	226.9	80.9
UZ-52-1	13.3	43	12.4	0.6	1220	270	1.8	1.0	223.0	35.5
UZ-52-2	24.4	13	10.3	0.6	2800	520	1.4	0.4	255.6	72.3
UZ-52-3	23.6	31	16.9	1.1	2240	450	1.6	0.6	233.6	44.6
UZ-52-5	12.9	48	7.8	0.5	2570	490	2.0	0.9	252.4	39.4

UZ-52-6	13.1	14	13.7	1.0	10320	630	1.7	0.5	206.4	57.1
UZ-53-1	16.8	161	29.8	2.0	17810	920	3.3	0.7	120.0	12.4
UZ-53-2	25.4	95	40.4	2.6	14590	740	3.1	0.5	137.6	16.7
UZ-53-3	29.7	101	91.1	5.8	17290	870	3.4	0.4	71.5	8.4
UZ-53-4	17.9	77	32.9	1.8	4830	500	2.1	0.2	119.1	15.1
UZ-53-5	28.5	105	46.6	2.4	19770	750	2.2	1.3	133.6	14.7
UZ-53-6	29.8	135	33.8	1.8	19500	1000	2.6	0.6	191.9	19.4
UZ-53-7	31.6	91	51.1	2.8	17000	1100	2.9	0.3	135.0	16.0
UZ-53-8	21.4	49	38.4	2.5	17040	970	2.0	0.2	121.8	19.1
UZ-53-9	32.6	85	40.6	2.6	16100	1100	1.5	0.2	175.1	22.1
UZ-53-10	29.3	57	44.2	2.4	18600	1100	3.2	0.3	144.9	20.7
UZ-53-11	37.8	109	56.6	2.1	22100	1300	3.9	0.5	145.9	15.0
UZ-53-12	33.2	61	37.2	2.1	23900	1000	2.0	1.1	194.0	27.1
UZ-53-13	32.8	139	55.7	3.6	22300	1100	2.3	1.0	128.7	13.7
UZ-53-14	34.5	57	48.7	3.4	21700	1200	1.2	0.1	154.6	23.1
UZ-53-15	27.4	136	42.9	1.9	24800	1300	3.0	0.4	139.3	13.4
UZ-53-16	24.7	58	46.8	2.9	22900	1300	3.0	0.3	115.7	16.8
UZ-53-17	32.5	74	50.6	2.5	16770	900	2.5	0.9	140.3	17.7
UZ-53-18	35.9	93	40.9	2.6	25000	1900	3.0	0.9	191.3	23.3
UZ-53-19	27.2	169	27.2	2.1	26700	1400	2.9	0.5	217.2	23.7
UZ-53-20	27.5	69	33.7	1.6	23200	1100	2.4	0.7	177.8	23.0
UZ-53-21	25.0	82	33.5	1.8	23700	1100	1.2	0.1	162.9	20.0
UZ-53-22	31.3	96	39.4	2.2	31500	1500	2.7	0.7	172.9	20.1
UZ-53-23	34.8	158	41.3	2.5	28600	2000	2.7	0.7	183.3	18.3
UZ-53-24	33.1	121	31.0	2.2	27800	1500	3.2	0.8	231.6	26.7
UZ-53-25	33.6	58	38.9	1.7	31200	2100	4.0	0.4	188.2	26.0
UZ-53-26	26.4	92	37.4	2.1	22600	1400	2.4	0.7	153.8	18.2
UZ-53-27	29.4	83	37.4	2.0	33100	1800	2.3	0.5	171.4	20.9
UZ-53-28	29.9	69	49.7	3.6	36900	2300	1.8	0.2	131.5	18.5
UZ-53-29	27.2	57	44.6	2.6	27900	1800	1.9	0.2	133.5	19.3
UZ-53-30	30.6	116	42.0	2.8	29600	1900	2.9	0.6	158.8	18.2

UZ-53-31	28.1	131	27.5	1.3	47800	2700	2.9	0.4	221.7	22.0
UZ-53-32	33.8	79	42.5	2.4	45400	2400	2.8	0.7	173.2	21.8
UZ-53-33	24.5	62	35.6	1.7	32000	2400	2.9	0.7	150.2	20.4
UZ-53-34	27.7	102	39.9	2.2	47500	2500	3.0	0.5	151.5	17.2
UZ-53-35	34.9	79	44.9	3.0	51400	2700	3.0	0.4	169.3	22.2
UZ-53-36	36.1	86	50.1	3.7	47600	2400	2.8	0.8	157.5	20.6
UZ-53-37	29.8	90	36.1	2.5	48700	3000	2.9	0.6	180.1	22.7
UZ-53-38	26.6	63	45.9	3.4	69800	2900	2.6	0.6	127.0	18.6
UZ-54-1	49.7	126	30.3	1.7	8350	500	2.0	0.7	213.0	22.4
UZ-54-2	38.6	105	36.0	2.8	12740	520	2.3	0.9	194.8	24.3
UZ-54-3	48.6	116	41.0	2.4	13840	420	2.2	0.7	215.0	23.6
UZ-54-4	48.0	202	39.7	2.5	9740	400	2.0	0.8	219.2	20.7
UZ-54-5	36.7	79	32.6	1.7	16250	460	2.3	0.6	204.7	25.4
UZ-54-6	46.8	169	36.9	2.6	8170	460	1.9	0.6	230.0	24.0
UZ-54-7	63.7	223	46.0	3.2	9650	440	1.7	0.7	215.4	20.8
UZ-54-8	76.0	201	108.2	9.7	1600	170	1.7	0.8	128.3	14.6
UZ-54-9	46.0	124	35.0	2.5	10270	460	2.2	0.9	238.1	27.3
UZ-54-10	46.9	182	39.6	2.5	14410	340	2.5	0.8	214.9	20.9
UZ-54-11	42.2	181	31.3	2.0	10560	420	2.2	0.7	244.3	24.0
UZ-54-12	35.3	100	30.0	1.5	13160	630	2.2	0.5	213.3	23.8
UZ-54-13	35.5	113	31.9	1.6	13280	430	2.4	0.5	202.1	21.5
UZ-54-14	50.1	162	45.1	4.1	13120	730	2.0	0.8	201.8	24.2
UZ-54-15	41.6	217	34.8	2.3	13540	700	2.0	0.7	216.7	20.5
UZ-54-16	40.7	139	31.1	1.3	6360	650	1.7	0.6	236.9	22.4
UZ-54-17	53.0	186	38.7	2.4	5410	380	2.1	0.7	247.9	23.8
UZ-54-18	35.4	103	38.4	2.6	6250	260	2.1	0.7	167.8	20.1
UZ-54-19	35.0	100	38.8	3.6	2910	210	2.0	1.0	164.4	22.4
UZ-54-20	45.5	115	41.7	4.1	9430	460	1.8	0.7	198.3	26.9
UZ-54-21	32.1	226	27.9	1.7	8690	390	2.0	0.5	208.6	18.8
UZ-54-22	61.3	235	66.8	5.7	13600	650	2.1	0.7	167.2	18.0
UZ-54-23	60.4	203	42.0	2.6	11390	640	2.1	0.6	209.5	19.6

UZ-54-24	37.4	144	32.3	2.5	12660	470	2.3	0.7	210.2	23.9
UZ-54-25	40.4	210	38.1	2.8	13320	590	2.1	0.5	192.8	19.4
UZ-54-26	41.4	175	33.6	3.1	7480	450	2.0	0.9	223.5	26.7
UZ-54-27	48.0	237	49.1	4.0	8010	590	1.9	0.6	178.0	18.5
UZ-54-28	46.4	170	35.7	2.9	10540	550	2.2	0.7	235.5	26.3
UZ-54-29	41.0	113	32.6	2.8	15110	850	2.3	0.5	228.1	29.1
UZ-54-30	37.7	140	32.6	2.1	9250	430	2.2	0.6	210.1	22.3
UZ-54-31	49.3	156	28.7	2.3	10570	750	2.2	0.6	235.7	26.7
UZ-54-32	43.6	144	36.3	3.4	9510	640	1.9	0.7	182.8	22.9
UZ-54-33	46.8	137	38.4	2.8	13720	590	2.2	0.6	220.9	24.8
UZ-54-34	35.1	154	33.3	2.4	6670	510	2.1	0.7	191.4	20.7
UZ-54-35	43.1	125	33.8	2.5	10660	710	2.1	0.6	231.3	26.8
UZ-54-36	37.0	80	30.6	1.9	7370	330	2.4	0.7	219.2	28.0
UZ-54-37	29.0	76	32.5	2.3	2470	310	1.8	0.7	162.5	21.9
UZ-55-1	3.5	9	7.7	0.6	510	120	2.1	0.7	83.3	28.5
UZ-55-2	26.7	105	35.2	2.8	9260	180	2.1	0.6	138.3	17.4
UZ-55-3	11.0	20	8.9	0.5	600	160	2.3	0.7	224.8	52.0
UZ-55-4	16.0	58	10.4	0.8	BLOD	BLOD	2.1	0.5	277.7	42.0
UZ-55-5	4.8	11	6.8	0.4	580	180	2.0	0.9	129.5	39.8
UZ-55-6	6.1	13	6.4	0.5	640	220	1.9	0.6	175.9	50.4
UZ-55-7	4.7	12	5.2	0.4	450	170	2.2	0.7	163.2	48.6
UZ-55-8	10.1	29	10.5	0.6	530	160	2.3	0.5	175.0	33.8
UZ-55-9	16.5	28	19.2	1.7	500	120	2.2	0.6	156.9	32.8
UZ-55-10	7.9	19	12.6	0.8	770	180	2.2	0.6	114.5	27.2
UZ-55-11	15.8	43	11.1	0.9	510	180	1.8	0.6	258.1	44.4
UZ-55-12	3.7	7	4.1	0.3	510	160	1.5	0.5	164.1	63.0
UZ-55-13	10.4	17	12.1	1.2	630	140	1.6	0.6	156.8	41.1
UZ-55-14	3.7	9	7.2	0.5	610	120	1.7	0.6	96.0	32.6
UZ-55-15	8.6	11	9.2	0.6	530	160	1.5	0.7	171.3	53.0
UZ-55-16	13.9	34	12.0	0.8	630	190	1.9	0.7	209.4	38.5
UZ-55-17	11.7	21	10.4	0.9	760	210	1.6	0.6	204.3	48.0

UZ-55-18	12.0	45	13.2	0.7	600	140	1.6	0.5	165.8	26.3
UZ-55-19	9.9	12	9.4	0.6	450	150	1.5	0.6	192.0	56.6
UZ-55-20	12.7	22	14.4	0.9	560	140	1.6	0.5	161.0	35.7
UZ-55-21	6.8	32	8.0	0.5	470	170	1.7	0.6	156.1	29.4
UZ-55-22	22.7	67	15.9	1.2	650	130	1.3	0.5	258.3	37.1
UZ-55-23	20.3	87	39.6	2.5	BLOD	BLOD	1.7	0.5	93.9	11.7
UZ-55-24	10.4	36	12.2	0.9	370	220	1.6	0.6	155.2	28.4
UZ-55-25	13.4	69	10.1	1.0	490	150	1.5	0.5	239.7	37.4
UZ-55-26	11.2	27	11.3	0.7	600	120	1.7	0.6	179.8	36.2
UZ-55-27	13.5	53	9.5	1.0	620	210	1.5	0.7	257.0	44.3
UZ-55-28	9.4	24	14.2	0.7	760	180	2.3	0.5	121.6	25.5
UZ-55-29	13.1	17	8.8	0.7	660	150	2.2	0.6	268.2	68.9
UZ-55-30	10.6	58	6.7	0.6	BLOD	BLOD	2.2	0.6	287.4	44.5
UZ-55-31	10.4	13	22.5	9.0	BLOD	BLOD	1.8	0.6	84.5	41.1
UZ-55-32	9.5	22	12.2	0.6	650	170	1.5	0.5	141.8	31.1
UZ-55-33	11.4	18	13.6	0.6	490	170	1.8	0.6	153.1	36.7
UZ-56-1	11.9	27	11.0	1.2	1660	220	1.8	0.6	224.8	49.7
UZ-56-2	11.5	22	7.3	0.5	680	220	1.5	0.5	324.4	72.0
UZ-56-3	5.1	10	6.0	0.3	750	130	1.6	0.6	179.2	57.5
UZ-56-4	4.5	9	5.1	0.3	16200	5500	1.7	0.6	187.4	63.7
UZ-56-5	43.1	88	36.3	1.9	5210	420	1.5	0.7	246.4	29.3
UZ-56-6	15.1	29	12.5	1.0	1090	240	2.3	0.5	250.8	50.7
UZ-56-7	41.4	103	36.6	2.4	12660	570	2.2	0.6	235.4	27.9
UZ-56-8	14.7	31	14.9	0.7	820	330	2.2	0.6	205.7	38.3
UZ-56-9	28.8	53	36.9	2.5	9770	680	1.8	0.6	163.1	25.0
UZ-56-10	38.1	91	30.5	2.5	11900	350	1.5	0.5	258.9	34.4
UZ-56-11	43.8	83	35.3	1.9	11840	380	1.6	0.6	257.3	31.5
UZ-56-12	8.4	13	7.9	0.4	700	210	1.7	0.6	220.0	62.2
UZ-56-13	13.7	24	11.5	0.7	760	200	1.5	0.7	247.9	52.6
UZ-56-14	16.7	34	23.5	1.6	BLOD	BLOD	1.9	0.7	148.8	27.4
UZ-56-15	44.3	269	43.6	3.5	13540	420	1.6	0.6	211.6	21.3

UZ-56-16	44.2	116	39.8	2.6	12290	600	1.6	0.5	230.9	26.2
UZ-56-17	11.8	37	10.4	0.6	4020	310	1.5	0.6	235.9	40.9
UZ-56-18	13.8	42	9.6	0.5	310	190	2.3	0.6	298.7	48.9
UZ-56-19	35.5	98	48.9	2.3	11250	460	2.0	0.5	187.9	20.9
UZ-56-20	37.9	110	32.8	2.3	10070	330	1.6	0.6	239.8	28.4
UZ-56-21	48.9	143	39.9	2.7	11200	480	1.5	0.5	254.1	27.3
UZ-56-22	61.4	112	57.5	2.4	10170	350	1.9	0.4	222.2	22.9
UZ-56-23	2.0	4	3.3	0.2	510	200	2.0	0.4	127.4	64.1
UZ-56-24	59.5	201	52.7	3.1	10970	410	1.8	0.5	234.8	21.6
UZ-56-25	54.5	125	63.0	3.1	12410	640	1.7	0.6	180.7	18.4
UZ-56-26	7.8	19	7.6	0.5	720	170	2.0	1.0	215.9	51.3
UZ-56-27	45.6	78	47.8	2.0	11380	400	2.0	0.7	198.9	24.0
UZ-56-28	7.6	14	12.8	0.7	BLOD	BLOD	1.9	0.8	124.8	34.0
UZ-56-29	10.3	30	13.4	0.7	730	180	1.9	0.8	161.0	30.5
UZ-56-30	13.9	40	14.0	1.4	540	180	2.9	1.0	207.1	38.7
UZ-56-31	22.2	159	46.5	3.0	12790	490	2.3	0.3	245.3	25.1
UZ-56-32	54.9	19	8.8	1.6	BLOD	BLOD	2.1	0.5	180.1	52.7
UZ-56-33	7.6	19	7.4	0.7	700	230	1.5	0.5	249.3	61.5
UZ-56-34	8.9	64	25.5	1.7	510	230	1.6	0.6	173.5	24.6
UZ-57-1	7.5	11	40.9	3.3	4380	740	1.3	0.5	15.5	4.8
UZ-57-2	12.2	10	36.4	2.3	8140	740	1.7	0.5	29.3	9.5
UZ-57-3	1.9	2	36.9	2.9	2540	270	1.4	0.6	6.6	4.7
UZ-57-4	7.0	13	60.1	3.2	5630	270	1.8	0.6	16.2	4.6
UZ-57-5	14.7	9	33.7	2.8	6250	640	1.5	0.5	29.0	10.0
UZ-57-6	18.5	23	81.5	7.3	4590	320	1.6	0.6	15.3	3.5
UZ-57-7	12.2	27	79.0	13.0	7930	240	1.7	0.6	14.2	3.6
UZ-57-8	12.6	20	45.4	2.2	5170	300	1.5	0.7	32.4	7.4
UZ-57-9	17.8	24	24.2	1.6	10700	370	1.9	0.7	72.1	15.5
UZ-57-10	17.8	20	40.9	4.3	8200	270	1.6	0.6	29.6	7.3
UZ-57-11	12.8	31	41.9	2.8	8260	440	1.6	0.5	36.0	6.9
UZ-57-12	9.7	15	62.5	2.9	6190	290	1.5	0.6	16.9	4.4

UZ-57-13	16.8	26	60.7	3.9	8090	570	1.6	0.5	23.3	4.8
UZ-57-14	31.8	31	42.3	2.5	9340	390	1.7	0.6	79.6	15.0
UZ-57-15	9.4	11	68.6	8.9	8010	510	1.3	0.5	17.1	5.6
UZ-57-16	22.1	20	44.5	3.4	9750	800	1.7	0.5	28.2	6.7
UZ-57-17	26.3	17	116.5	7.3	7000	410	1.6	0.6	16.6	4.2
UZ-57-18	17.8	16	19.8	1.0	11990	320	1.5	0.5	67.1	17.1
UZ-57-19	1.8	1	5.8	0.8	670	230	1.0	0.6	19.3	19.4
UZ-57-20	26.7	32	37.9	3.2	13590	700	1.9	0.6	72.0	14.1
UZ-57-21	9.8	9	23.5	1.5	10300	380	1.3	0.3	35.5	12.1
UZ-57-22	26.0	33	40.8	4.0	10160	560	1.6	0.7	39.7	7.9
UZ-58-1	8.3	26	4.8	0.3	7400	270	2.0	0.4	247.7	50.4
UZ-58-2	10.0	33	6.7	0.4	8710	470	2.0	0.7	226.8	41.5
UZ-58-3	5.2	24	6.7	0.3	8580	360	2.3	0.6	133.9	28.0
UZ-58-4	12.5	45	14.9	1.2	6430	300	2.3	0.6	143.7	24.4
UZ-58-5	6.8	12	6.0	0.4	9450	340	2.0	0.5	195.0	58.0
UZ-58-6	6.1	18	5.6	0.5	7650	400	1.6	0.5	188.3	47.3
UZ-58-7	11.2	15	10.5	0.7	8570	440	1.5	0.6	182.7	48.8
UZ-58-8	6.5	22	6.2	0.4	8180	350	1.6	0.5	178.9	39.9
UZ-58-9	8.5	27	7.7	0.5	9280	390	1.7	0.6	188.3	38.3
UZ-58-10	12.0	23	11.0	0.9	7680	430	1.6	0.6	184.4	41.1
UZ-58-11	4.1	14	6.6	0.6	7680	390	1.5	0.5	108.2	30.7
UZ-58-12	11.4	22	11.0	0.7	7430	360	1.9	0.4	177.9	39.6
UZ-58-13	9.7	17	7.0	0.7	8010	440	2.0	0.4	233.3	60.9
UZ-58-14	6.6	10	8.0	0.5	8310	460	1.8	0.5	142.5	45.9
UZ-58-15	8.8	24	7.5	0.5	8740	360	1.7	0.6	199.5	42.5
UZ-58-16	4.0	9	7.0	0.4	8650	380	3.1	0.5	98.3	33.3
UZ-58-17	7.1	13	11.1	0.7	7920	490	2.7	0.7	110.6	31.5
UZ-58-18	4.7	10	7.7	0.7	8030	330	1.5	0.4	106.2	34.9
UZ-58-19	7.7	28	6.6	0.6	8140	360	1.4	0.6	199.7	41.9
UZ-58-20	11.9	59	9.1	0.9	8130	380	2.2	0.8	221.9	36.0
UZ-58-21	7.1	18	7.0	0.4	7120	310	1.7	0.6	172.5	41.7

UZ-58-22	10.8	30	9.9	0.5	7180	330	1.9	0.5	186.5	35.5
UZ-58-23	11.1	27	9.0	0.8	8370	330	1.4	0.5	208.2	43.9
UZ-58-24	10.3	24	13.9	1.4	6970	340	1.9	0.9	127.3	29.0
UZ-58-25	5.0	12	5.6	0.3	8390	340	1.6	0.6	154.1	45.4
UZ-58-26	9.2	15	8.1	0.4	7320	440	1.1	0.3	194.7	51.2
UZ-58-27	7.5	16	11.4	1.4	6700	380	1.9	0.5	112.0	31.2
UZ-58-28	12.1	23	10.8	0.9	10810	550	2.2	0.6	190.9	43.1
UZ-58-29	10.7	19	15.7	1.0	6970	370	1.8	0.4	116.7	27.8
UZ-58-30	9.4	11	8.4	0.9	7250	460	2.0	0.3	190.8	61.0
UZ-58-31	11.6	24	14.7	1.5	8940	330	2.0	0.8	135.0	30.8
UZ-59-1	5.2	12	18.9	1.1	4460	280	1.8	0.7	50.5	14.9
UZ-59-2	12.6	30	20.3	1.1	4980	230	2.3	0.7	113.7	21.7
UZ-59-3	13.1	34	19.6	1.5	4760	330	1.9	0.8	122.4	23.0
UZ-59-4	5.5	14	11.7	0.7	5150	310	2.1	0.4	86.3	23.6
UZ-59-5	11.2	30	26.3	2.0	3950	230	1.9	0.6	77.8	15.4
UZ-59-6	17.1	25	27.0	1.7	4130	230	2.0	0.4	115.9	24.3
UZ-59-7	17.2	59	23.8	1.7	4290	350	2.0	0.7	132.0	19.6
UZ-59-8	11.4	31	15.1	0.7	5270	270	2.3	0.6	138.1	25.7
UZ-59-9	18.8	51	34.1	2.9	5250	250	2.3	0.6	100.7	16.5
UZ-59-10	23.6	61	23.7	2.4	4970	360	2.0	0.5	181.4	29.6
UZ-59-11	6.8	17	11.0	1.0	3900	480	1.6	0.6	113.5	29.4
UZ-59-12	9.3	19	15.6	1.8	5510	280	1.5	0.5	108.9	28.0
UZ-59-13	31.9	72	26.3	1.9	5120	380	1.9	0.4	220.2	30.4
UZ-59-14	5.5	11	19.9	1.0	5250	240	2.0	0.4	50.7	15.5
UZ-59-15	11.7	32	25.7	1.6	4800	230	1.8	0.5	83.8	15.7
UZ-59-16	8.1	19	29.1	2.2	2380	160	1.7	0.6	51.3	12.4
UZ-59-17	5.4	11	6.6	0.5	4560	250	2.0	1.0	149.2	46.1
UZ-59-18	24.6	38	21.4	1.6	5150	300	2.0	0.7	208.5	37.3
UZ-59-19	12.5	43	12.9	0.8	4920	310	1.9	0.8	177.0	29.3
UZ-59-20	11.2	20	25.7	1.5	5050	300	1.9	0.8	79.6	18.4
UZ-59-21	7.4	16	24.6	1.7	4330	260	2.9	1.0	55.1	14.3

UZ-59-22	13.5	32	21.0	2.0	5230	410	2.3	0.3	117.9	23.7
UZ-59-23	18.4	38	45.0	2.6	5760	340	2.1	0.5	75.0	12.9
UZ-59-24	6.2	12	12.4	1.0	5140	280	3.1	0.5	91.4	27.4
UZ-59-25	5.2	12	5.1	0.4	4410	220	2.7	0.7	187.1	55.5
UZ-59-26	11.2	32	53.7	3.3	5110	330	1.5	0.4	38.3	7.2
UZ-59-27	4.5	14	11.9	0.7	4120	170	1.4	0.6	69.1	19.0
UZ-59-28	7.0	10	32.7	4.3	4450	270	2.0	1.0	39.2	13.4
UZ-59-29	14.4	20	35.2	2.6	5060	260	2.6	0.8	74.8	17.6
UZ-59-30	11.5	30	34.0	2.9	5300	290	1.8	0.4	62.0	12.5
UZ-59-31	48.7	72	34.0	3.2	5300	340	1.7	0.6	259.1	39.1
UZ-60-1	20.3	103	19.8	1.5	6630	320	2.2	0.6	186.8	23.2
UZ-60-2	3.2	11	3.5	0.2	2050	150	2.1	0.3	167.7	51.6
UZ-60-3	13.8	37	16.3	1.0	5250	260	2.4	0.5	154.7	27.1
UZ-60-4	20.8	56	16.0	1.1	5340	300	1.9	0.6	235.8	35.4
UZ-60-5	23.3	86	28.4	2.3	5000	200	1.9	0.4	149.4	20.2
UZ-60-6	17.2	74	23.4	2.3	5550	380	2.2	0.8	134.4	20.5
UZ-60-7	25.0	119	26.9	2.0	5180	220	1.7	0.6	169.3	20.0
UZ-60-8	16.5	58	19.9	1.1	3080	220	1.9	0.5	150.8	21.5
UZ-60-9	18.1	54	27.8	1.8	3050	140	1.4	0.5	118.9	17.9
UZ-60-10	19.0	55	32.6	1.9	2810	280	1.6	0.4	106.5	15.7
UZ-60-11	13.9	49	16.5	1.0	4370	270	2.1	0.7	153.6	23.7
UZ-60-12	19.2	75	21.8	1.5	4260	290	1.5	0.6	160.1	21.5
UZ-60-13	16.3	32	28.7	2.1	4330	260	2.0	0.5	103.7	19.8
UZ-60-14	11.8	35	18.3	1.9	3410	370	2.0	0.7	117.8	23.4
UZ-60-15	16.1	49	20.3	1.8	4620	220	2.3	1.4	144.9	24.4
UZ-60-16	15.6	26	17.4	1.4	6430	290	1.5	0.5	163.5	34.7
UZ-60-17	12.2	71	17.9	1.2	4970	240	1.6	0.7	124.4	17.0
UZ-60-18	9.9	40	12.5	1.0	3840	190	1.3	0.6	145.4	25.6
UZ-60-19	8.7	45	10.7	0.8	2010	190	1.4	0.5	148.5	25.0
UZ-60-20	21.4	41	18.0	1.0	5280	350	1.8	0.8	215.7	35.8
UZ-60-21	17.1	65	19.1	1.6	5090	240	1.7	0.5	163.2	24.4

UZ-60-22	15.7	39	18.9	1.4	5030	260	1.9	0.7	151.7	26.8
UZ-60-23	18.9	59	39.7	2.4	3260	220	2.3	0.8	87.4	12.5
UZ-60-24	11.1	32	20.0	1.2	5300	290	2.6	0.7	101.5	18.9
UZ-60-25	19.5	29	35.9	2.5	2230	200	2.4	1.0	99.5	19.7
UZ-60-26	16.3	42	22.2	1.6	4630	260	2.1	0.9	134.0	22.8
UZ-60-27	11.5	47	9.3	0.9	3880	270	2.4	0.8	224.8	39.8
UZ-60-28	4.4	26	6.9	0.6	1830	210	1.9	1.0	115.6	24.6
UZ-60-29	12.5	37	18.0	1.0	5950	430	2.3	0.7	126.6	21.9
UZ-60-30	11.9	32	26.2	2.5	4090	170	1.6	0.7	83.3	16.7
UZ-60-31	18.4	43	28.1	1.6	5020	240	1.9	0.8	119.7	19.5
UZ-60-32	17.0	35	17.1	1.1	5290	230	1.8	0.7	181.1	32.7
UZ-60-33	24.0	60	31.1	2.1	3170	250	1.9	0.9	140.7	20.5
UZ-60-34	24.7	52	38.6	2.9	4230	290	1.6	0.6	117.1	18.5
UZ-60-35	14.2	36	20.2	1.3	5200	230	1.6	0.5	128.4	22.9
UZ-60-36	5.0	12	6.2	0.6	7750	400	1.7	0.6	148.9	45.5
UZ-61-1	12.0	57	8.6	0.9	4740	560	1.8	0.4	218.8	37.5
UZ-61-2	18.3	99	17.2	1.7	5260	780	2.4	0.6	191.7	27.0
UZ-61-3	7.8	40	5.2	0.8	5160	840	1.9	0.4	220.4	47.1
UZ-61-4	8.3	32	9.0	0.8	5710	850	2.0	0.4	168.4	33.7
UZ-61-5	5.8	40	3.7	0.6	4680	710	1.7	0.5	226.9	49.1
UZ-61-6	15.9	112	15.4	1.8	5940	800	1.8	0.5	187.9	28.2
UZ-61-7	10.1	81	9.6	1.2	6550	710	2.0	0.4	191.8	32.1
UZ-61-8	10.9	56	9.1	0.8	4540	440	2.2	0.4	218.9	35.5
UZ-61-9	9.6	36	6.1	0.5	6630	750	1.7	0.4	215.0	39.8
UZ-61-10	10.3	72	11.0	1.0	4200	990	1.5	0.7	169.5	25.0
UZ-61-11	8.6	28	7.1	0.9	5650	410	2.1	0.5	178.0	40.0
UZ-61-12	8.0	27	5.8	0.9	4990	600	2.2	0.3	222.4	54.1
UZ-61-13	5.6	39	4.3	0.6	4720	830	2.1	0.3	229.4	49.3
UZ-61-14	11.9	49	12.6	1.8	4910	760	1.1	0.3	171.4	34.6
UZ-61-15	21.4	78	8.5	1.3	5960	860	1.9	0.5	313.0	59.6
UZ-61-16	17.5	80	11.6	1.6	7280	740	2.2	0.6	224.9	39.9

UZ-61-17	42.2	198	45.9	3.1	3810	400	1.8	0.4	167.6	16.4
UZ-61-18	17.5	59	12.6	1.0	4330	230	2.0	0.3	250.7	38.1
UZ-61-19	9.9	84	8.1	0.9	4350	590	2.0	0.8	223.2	33.8
UZ-61-20	25.7	229	31.8	2.5	4350	400	1.9	0.4	147.3	15.1
UZ-61-21	12.6	54	7.0	0.6	5060	500	1.9	0.5	252.1	40.2
UZ-61-22	7.7	60	7.1	0.7	4930	430	2.7	0.6	196.9	32.3
UZ-61-23	8.7	70	7.2	0.7	4370	420	2.7	1.2	217.8	33.5
UZ-61-24	7.1	42	5.7	0.6	4110	400	2.4	0.4	224.9	41.5
UZ-61-25	33.8	152	26.6	3.1	4360	660	2.2	0.6	215.2	30.6
UZ-61-26	7.8	48	7.3	1.0	3980	850	2.1	0.6	195.4	38.0
UZ-61-27	13.1	43	7.1	0.5	4730	560	2.2	0.9	258.6	43.3
UZ-61-28	30.0	110	18.7	2.7	4420	470	2.1	0.4	214.5	37.1
UZ-61-29	16.5	37	7.2	0.9	4580	580	2.5	0.8	324.7	66.8
UZ-61-30	15.3	55	9.9	2.0	4910	760	1.7	0.3	226.5	55.0
UZ-61-31	7.0	29	6.9	0.6	5780	630	1.5	0.5	185.2	38.3
UZ-61-32	5.5	25	4.5	0.6	5430	870	1.7	0.4	223.8	54.4
UZ-61-33	17.9	70	11.0	0.9	4880	480	2.1	1.0	250.2	36.5
UZ-61-34	21.3	115	19.8	2.0	5100	630	2.1	0.4	195.9	26.9
UZ-61-35	15.5	73	13.0	1.7	7600	1000	1.8	0.5	215.9	37.9
UZ-61-36	15.3	58	14.8	2.1	8600	2400	1.8	0.6	188.4	36.4
UZ-61-37	9.2	19	6.4	0.6	6140	510	1.9	0.4	176.0	43.8
UZ-61-38	8.4	31	8.1	1.1	7200	840	1.7	0.6	153.7	34.6
UZ-62-1	19.0	45	11.3	1.0	5200	220	2.1	0.5	200.4	34.6
UZ-62-2	21.6	193	14.0	0.6	5080	160	2.1	0.6	219.8	18.3
UZ-62-3	21.7	150	21.4	1.6	4720	270	2.3	0.6	184.7	20.4
UZ-62-4	14.2	100	15.2	1.3	4810	280	2.3	0.8	169.6	22.3
UZ-62-5	15.1	67	14.8	1.4	5060	380	2.3	0.5	185.9	28.7
UZ-62-6	14.9	74	15.6	1.3	5330	190	2.0	0.6	173.3	24.8
UZ-62-7	20.0	116	18.2	1.1	5100	220	2.3	0.4	199.3	22.1
UZ-62-8	11.4	52	9.4	1.1	4190	310	2.3	0.5	220.2	39.9
UZ-62-9	17.4	84	14.9	2.1	4660	440	2.1	0.6	211.6	37.7

UZ-62-10	19.2	96	22.2	2.7	4530	200	2.4	0.7	157.5	25.0
UZ-62-11	22.7	120	21.7	1.7	4520	210	2.1	0.8	190.4	22.9
UZ-62-12	17.3	89	14.7	1.3	4880	180	1.8	0.5	213.3	29.4
UZ-62-13	16.8	99	21.3	1.7	4850	280	2.3	0.5	144.0	18.5
UZ-62-14	18.6	110	21.6	2.5	4390	310	2.3	0.3	156.6	23.5
UZ-62-15	15.5	85	20.3	2.7	4430	300	2.4	0.4	138.9	23.8
UZ-62-16	14.9	51	24.3	2.6	4120	420	1.7	0.8	112.5	19.8
UZ-62-17	18.9	71	24.1	2.0	4370	290	2.1	0.4	142.9	20.7
UZ-62-18	19.1	92	23.9	2.4	3940	270	2.3	0.8	145.7	21.1
UZ-62-19	17.2	75	22.0	1.7	4060	210	2.2	0.4	142.8	19.8
UZ-62-20	23.0	116	38.6	2.8	3850	250	1.9	0.6	108.8	12.8
UZ-62-21	13.1	56	19.2	1.2	3780	160	2.2	0.4	124.5	18.4
UZ-62-22	13.5	28	27.6	1.6	4050	180	2.0	0.3	89.8	17.8
UZ-62-23	17.4	60	28.5	2.4	2810	150	1.9	0.5	110.0	17.0
UZ-62-24	16.6	76	33.4	1.8	3400	190	2.2	0.3	90.8	11.5
UZ-62-25	9.9	52	14.4	1.3	3810	280	2.4	0.2	125.8	20.8
UZ-62-26	17.8	70	33.8	2.5	3430	130	2.3	0.6	96.3	13.5
UZ-62-27	29.2	131	74.9	6.2	1490	190	2.1	0.4	71.5	8.6
UZ-62-28	18.0	57	38.9	3.0	4230	220	2.2	0.6	85.0	13.0
UZ-63-1	9.0	58	10.6	0.6	660	92	1.9	0.7	154.3	21.9
UZ-63-2	10.4	29	9.5	0.7	730	140	1.7	0.5	198.0	39.7
UZ-63-3	6.4	20	12.3	0.7	800	160	1.7	0.8	95.5	21.9
UZ-63-4	9.5	19	14.8	0.9	710	160	1.6	0.3	117.3	27.8
UZ-63-5	10.9	52	14.2	1.3	1640	230	1.6	0.7	140.6	23.4
UZ-63-6	23.5	88	14.7	0.7	680	180	1.8	0.5	260.4	30.6
UZ-63-7	16.1	89	13.7	0.8	1070	170	1.8	0.6	212.3	25.8
UZ-63-8	9.9	39	12.2	0.6	670	130	1.8	0.4	147.2	24.6
UZ-63-9	8.8	44	10.5	0.6	1890	220	1.4	0.4	154.0	25.1
UZ-63-10	15.8	48	16.2	1.4	1480	170	1.8	0.6	178.0	29.9
UZ-63-11	10.2	44	9.7	0.7	1100	190	1.8	0.5	190.2	31.6
UZ-63-12	7.7	61	12.3	0.8	630	160	1.8	0.8	114.5	16.5

UZ-63-13	9.0	33	14.0	0.8	550	140	2.0	0.6	116.8	21.5
UZ-63-14	8.7	68	13.2	1.0	1130	170	1.5	0.5	119.9	17.1
UZ-63-15	8.2	84	10.6	0.7	1230	180	1.3	0.4	141.1	17.9
UZ-63-16	11.0	43	11.2	0.7	400	160	1.7	0.4	179.1	29.3
UZ-63-17	12.4	55	10.1	1.0	820	200	1.6	0.5	223.1	37.3
UZ-63-18	15.5	62	13.0	0.7	1010	190	1.5	0.7	215.3	29.9
UZ-63-19	12.7	51	8.1	1.1	860	150	1.7	0.5	282.0	55.0
UZ-63-20	11.5	61	12.3	0.8	630	130	1.6	0.5	170.1	24.4
UZ-63-21	13.8	54	7.3	0.4	1120	150	1.5	0.4	302.5	44.1
UZ-63-22	10.6	31	6.4	0.5	910	160	1.8	0.3	256.7	50.3
UZ-63-23	7.6	26	5.6	0.3	500	120	2.3	0.2	243.9	49.9
UZ-63-24	10.4	48	10.0	0.8	650	200	1.6	0.3	187.8	31.2
UZ-63-25	8.2	59	5.5	0.6	490	130	1.3	0.4	272.0	45.4
UZ-63-26	9.6	55	8.5	0.5	1000	150	1.5	0.5	205.9	30.3
UZ-63-27	13.1	102	7.4	0.4	1440	160	1.6	0.6	318.3	36.3
UZ-63-28	9.2	23	12.7	1.1	990	200	1.8	0.4	132.5	29.9
UZ-63-29	7.9	55	10.5	0.7	1640	160	1.6	0.5	138.2	20.7
UZ-63-30	15.6	105	12.8	0.8	580	160	2.1	0.8	221.1	26.0
UZ-63-31	11.1	66	7.4	0.4	627	95	1.6	0.4	268.6	35.4
UZ-63-32	13.3	69	8.1	0.6	700	130	1.6	0.4	295.3	41.5
UZ-63-33	13.7	144	12.3	1.6	1540	130	1.6	0.4	201.6	31.1
UZ-63-34	13.0	64	13.6	0.8	430	140	1.8	0.3	173.7	23.9
UZ-63-35	10.3	45	6.3	0.4	1110	140	1.8	0.5	294.3	47.7
UZ-63-36	5.9	22	11.3	0.5	640	180	1.9	0.7	95.4	20.7
UZ-63-37	8.1	27	8.7	0.6	370	170	1.7	0.3	169.4	34.6
UZ-63-38	9.3	42	11.5	0.8	410	140	2.3	1.0	146.8	25.0
UZ-63-39	5.9	22	12.6	0.7	830	130	1.7	0.5	86.1	18.9
UZ-65-1	8.3	13	9.0	0.5	877	92	1.1	53.2	166.9	47.0
UZ-65-2	13.8	43	9.0	0.4	9540	310	1.8	0.7	276.6	43.6
UZ-65-3	4.2	9	5.4	0.3	2350	300	1.4	0.7	141.0	47.7
UZ-65-4	2.7	11	3.7	0.3	1420	120	1.4	0.5	132.3	40.9

UZ-65-5	7.6	20	8.3	0.3	6760	160	1.2	0.5	166.2	37.7
UZ-65-6	11.4	14	5.1	0.4	1030	120	1.5	0.6	313.3	86.9
UZ-65-7	4.9	18	5.0	0.3	2590	140	1.8	0.6	178.4	43.5
UZ-65-8	17.2	164	23.6	1.3	389	95	1.4	0.3	133.1	12.7
UZ-65-9	2.3	9	2.3	0.1	1336	96	1.3	0.5	179.0	60.4
UZ-65-10	34.2	94	27.7	1.2	2680	120	2.1	0.8	223.9	25.1
UZ-65-11	10.9	31	7.2	0.4	7190	290	2.3	0.5	234.9	44.2
UZ-65-12	7.6	33	5.6	0.2	6680	240	1.7	0.7	245.3	43.8
UZ-65-13	4.4	13	3.3	0.2	1807	97	1.7	0.7	242.4	68.2
UZ-65-14	4.9	8	7.7	0.5	1620	130	1.3	0.8	115.4	41.6
UZ-65-15	7.3	25	10.2	0.6	1350	110	1.6	0.5	130.3	27.1
UZ-65-16	10.9	25	15.0	1.3	690	150	1.8	0.5	132.8	28.9
UZ-65-17	22.7	29	13.8	0.9	651	95	1.6	0.3	239.8	47.4
UZ-66-1	12.5	21	18.3	1.6	2360	240	2.9	0.5	142.4	33.5
UZ-66-2	12.2	46	24.5	1.7	1700	180	2.6	1.0	104.5	17.0
UZ-66-3	18.2	73	15.9	1.2	2270	240	2.7	0.6	237.3	33.0
UZ-66-4	24.0	69	18.0	1.2	2620	220	2.3	0.8	275.9	38.0
UZ-66-5	24.0	64	13.5	0.9	2420	200	2.5	0.6	297.3	42.4
UZ-66-6	17.5	99	12.5	1.0	2340	330	2.8	0.5	289.1	37.1
UZ-66-7	8.5	29	9.4	0.8	2030	230	2.7	0.3	188.5	38.1
UZ-66-8	14.4	53	17.6	1.3	2360	170	2.2	0.6	170.7	26.6
UZ-66-9	12.4	28	5.6	0.5	2080	340	2.8	0.4	356.8	73.6
UZ-66-10	11.8	39	27.9	2.1	1620	180	2.5	1.0	89.2	15.8
UZ-66-11	12.7	37	18.6	1.6	1820	200	2.4	0.5	142.5	26.4
UZ-66-12	20.2	54	15.8	1.1	2330	220	2.4	0.4	265.6	40.6
UZ-66-13	7.6	18	8.2	0.6	2870	290	2.7	1.0	193.9	48.1
UZ-66-14	7.1	29	17.7	1.5	2010	250	2.1	0.4	84.8	17.3
UZ-66-15	20.1	62	30.0	1.8	1870	200	2.4	0.6	140.0	19.7
UZ-66-16	11.3	16	5.7	0.4	1970	140	1.9	0.5	275.9	71.3
UZ-66-17	21.0	95	17.4	1.0	2680	210	2.3	0.5	250.4	29.4
UZ-66-18	6.8	22	7.4	0.4	2000	200	1.5	0.5	192.2	42.3

UZ-66-19	18.3	76	19.5	1.4	1740	260	2.6	0.5	195.4	26.4
UZ-66-20	15.0	61	18.3	1.6	2700	150	2.7	0.7	170.9	26.5
UZ-66-21	12.8	63	14.1	1.7	2140	270	2.7	0.7	189.8	33.1
UZ-66-22	13.7	44	20.8	1.5	2330	280	2.4	0.4	138.2	23.1
UZ-66-23	21.5	62	11.5	1.2	1960	260	2.4	0.3	295.4	48.6
UZ-66-24	15.6	24	8.3	0.7	2790	320	2.6	0.2	267.4	58.5
UZ-66-25	17.0	50	15.4	1.0	1820	280	2.4	0.4	228.8	35.6
UZ-66-26	18.7	56	24.4	1.5	2360	230	2.9	0.7	160.5	23.6
UZ-66-27	19.7	51	18.6	1.4	1870	290	2.5	0.7	220.0	35.0
UZ-66-28	16.0	36	18.1	1.3	2100	220	2.3	0.3	184.6	33.5
UZ-66-29	14.4	43	11.8	1.0	1400	230	2.6	0.6	253.6	43.9
UZ-66-30	14.0	39	18.2	1.4	2620	210	2.4	0.5	160.2	28.5
UZ-66-31	19.3	41	17.5	1.8	2090	250	2.3	0.7	229.1	42.8
UZ-67-1	4.0	14	2.7	0.1	1130	170	2.1	0.3	309.1	84.0
UZ-67-2	10.3	39	10.8	0.6	1240	310	1.5	0.4	199.4	33.9
UZ-67-3	1.8	3	3.8	0.3	1350	220	1.5	0.2	102.7	59.9
UZ-67-4	11.4	43	10.8	1.1	1410	200	1.7	0.2	218.8	40.1
UZ-67-5	12.6	36	12.3	0.7	1240	180	2.4	0.7	213.3	37.6
UZ-67-6	7.6	28	7.5	0.6	1440	290	1.9	0.3	208.6	42.3
UZ-67-7	9.6	54	10.7	0.5	1570	290	1.7	0.3	187.2	26.8
UZ-67-8	5.5	14	7.1	0.6	1300	240	2.2	0.2	162.7	45.3
UZ-67-9	6.1	38	4.5	0.3	970	210	2.0	0.4	252.1	44.2
UZ-67-10	10.8	35	9.1	0.9	1020	330	2.2	0.3	248.1	48.2
UZ-67-11	4.1	14	5.4	0.3	1300	200	1.8	0.2	157.3	42.9
UZ-67-12	11.5	89	9.0	0.6	1120	260	2.0	0.3	263.0	32.4
UZ-67-13	8.1	40	8.3	0.7	1730	270	1.9	0.3	202.1	36.0
UZ-67-14	5.9	31	5.7	0.3	920	180	1.9	0.3	215.2	40.0
UZ-67-15	14.2	45	21.3	1.2	1010	290	1.9	0.4	139.9	22.3
UZ-67-16	4.9	28	3.8	0.2	1610	210	1.9	0.5	269.4	53.1
UZ-67-17	6.3	33	5.9	0.5	1520	210	1.9	0.3	224.6	43.3
UZ-67-18	8.1	31	9.2	0.4	1290	150	1.6	0.4	183.8	34.1

UZ-67-19	9.9	28	6.0	0.6	1190	180	2.5	0.8	308.0	64.6
UZ-67-20	6.4	24	7.8	0.3	950	140	2.7	0.6	171.0	35.7
UZ-67-21	12.5	61	12.8	0.6	1080	230	2.1	0.3	203.4	27.7
UZ-67-22	11.4	39	15.9	1.0	1320	300	2.2	0.6	150.0	25.7
UZ-67-23	10.5	37	23.9	2.9	1390	200	2.6	0.7	91.9	18.8
UZ-67-24	8.5	24	11.8	0.6	1180	220	1.7	0.5	150.0	31.7
UZ-67-25	13.0	24	13.7	0.8	1140	180	1.5	0.2	197.8	41.8
UZ-67-26	13.7	31	12.9	0.6	1120	180	2.1	0.7	221.6	41.0
UZ-67-27	5.2	9	6.6	0.4	1350	170	2.2	0.3	165.3	56.2
UZ-67-28	11.4	37	9.7	0.8	1060	200	1.4	0.5	243.0	45.1
UZ-67-29	8.0	18	5.9	0.4	1360	270	2.7	0.4	282.1	68.7
UZ-67-30	12.7	29	14.8	0.9	1290	200	2.2	0.5	179.2	34.8
UZ-67-31	2.9	7	4.7	0.3	990	280	2.3	0.7	129.2	49.3
UZ-67-32	5.3	12	6.8	0.3	1290	200	2.2	0.7	162.0	47.3
UZ-67-33	5.7	14	3.6	0.3	1060	200	1.9	0.2	287.3	79.5
UZ-67-34	9.1	23	9.0	0.6	1540	230	2.2	0.3	200.6	43.8
UZ-67-35	3.2	7	4.3	0.3	3910	290	2.5	0.4	153.5	59.0
UZ-67-36	6.5	16	5.8	0.4	1210	220	2.2	0.2	233.8	60.9
UZ-67-37	3.9	12	6.2	0.3	940	140	2.0	0.2	130.6	38.4
UZ-68-1	15.1	22	50.1	3.6	1420	280	1.6	0.3	63.5	14.3
UZ-68-2	3.0	4	2.8	0.1	1560	240	1.5	0.5	223.9	112.4
UZ-68-3	5.0	9	15.5	1.1	3970	320	2.7	0.5	68.0	23.2
UZ-68-4	5.0	8	7.8	0.5	1940	270	1.1	0.4	136.0	48.8
UZ-68-5	4.8	11	7.2	0.3	2050	280	2.0	0.1	140.5	42.8
UZ-68-6	4.3	11	5.1	0.3	2190	200	1.9	0.7	177.9	55.0
UZ-68-7	11.3	26	15.4	1.2	5850	390	1.7	0.4	153.7	32.4
UZ-68-8	10.9	32	8.0	0.6	1160	260	1.5	0.3	282.5	54.8
UZ-68-9	13.9	44	17.0	0.9	1900	230	1.7	0.4	169.8	27.1
UZ-68-10	3.6	11	6.6	0.5	2030	300	1.2	0.2	115.5	35.7
UZ-68-11	1.7	3	5.2	0.4	1490	230	2.1	0.0	69.4	40.4
UZ-68-12	8.3	15	8.1	0.6	2210	330	2.3	0.9	212.5	57.2

UZ-68-13	44.4	74	83.0	13.0	2430	280	1.8	0.6	112.2	21.9
UZ-68-14	4.3	9	3.7	0.2	2220	290	1.7	0.2	238.8	80.3
UZ-68-15	1.9	4	5.9	0.3	1960	280	2.2	0.3	67.5	33.9
UZ-68-16	3.2	6	4.2	0.3	21100	9900	1.5	0.6	159.7	66.1
UZ-68-17	12.2	20	26.9	1.6	2550	290	1.8	0.4	94.8	21.9
UZ-68-18	0.8	2	4.8	0.3	2270	280	1.6	0.3	34.3	24.4
UZ-68-19	1.7	2	4.9	0.3	1850	330	1.7	0.5	74.6	53.0
UZ-68-20	4.1	7	3.9	0.3	1480	240	1.4	0.3	222.1	85.3
UZ-68-21	5.6	8	5.5	0.2	8700	2900	1.6	0.4	214.8	76.5
UZ-68-22	2.3	4	5.3	0.5	2290	430	2.3	0.8	91.2	46.5
UZ-68-23	1.8	2	3.3	0.2	2310	240	1.4	0.5	110.4	78.3
UZ-68-24	0.7	1	4.5	0.2	1880	260	0.5	0.4	30.5	30.6
UZ-68-25	12.8	21	22.0	1.5	3490	310	1.5	0.7	121.8	27.8
UZ-68-26	6.7	11	10.4	0.8	8100	3400	1.5	0.8	135.4	42.0
UZ-68-27	31.6	71	42.9	3.9	4740	340	1.9	0.4	154.1	23.0
UZ-69-1	4.0	5	13.9	0.9	4600	370	1.9	0.2	60.7	27.4
UZ-69-2	10.1	10	25.0	1.7	4430	300	1.6	0.9	85.1	27.5
UZ-69-3	3.5	6	22.5	1.9	8830	440	2.2	0.6	32.5	13.6
UZ-69-4	6.6	14	12.8	0.6	5170	430	1.5	0.5	108.2	29.4
UZ-69-5	6.5	12	22.9	1.1	5270	450	1.6	0.5	59.6	17.4
UZ-69-6	5.8	13	17.4	1.0	5430	310	1.8	0.3	70.4	19.9
UZ-69-7	18.2	10	13.2	0.7	6130	390	1.6	0.3	144.2	46.2
UZ-69-8	2.3	4	11.7	0.7	6710	470	1.7	0.5	40.6	20.5
UZ-69-9	10.2	31	21.5	1.3	6400	390	1.4	0.3	99.6	18.9
UZ-69-10	7.1	13	13.0	1.0	5910	360	1.6	0.4	114.8	33.0
UZ-69-11	6.0	9	10.5	0.5	5580	290	2.0	0.1	120.5	40.6
UZ-69-12	18.1	19	15.8	1.1	6620	330	2.3	0.4	157.1	37.7
UZ-69-13	11.5	14	16.5	1.0	6320	300	0.6	0.1	102.6	28.1
UZ-69-14	11.0	10	12.2	0.9	5570	390	1.8	0.6	99.1	32.3
UZ-69-15	12.3	13	18.1	1.1	4770	360	2.2	0.6	109.2	31.0
UZ-69-16	9.3	11	16.8	0.7	5590	390	1.9	0.7	91.9	28.0

UZ-69-17	9.4	17	16.3	1.1	5270	470	1.5	0.5	102.9	25.9
UZ-69-18	9.8	23	23.2	1.7	4870	390	2.0	0.2	81.4	18.0
UZ-69-19	14.5	21	24.9	2.1	5770	450	1.5	0.2	91.6	21.4
UZ-70-1	4.8	12	3.6	0.3	630	190	1.4	0.6	272.9	81.4
UZ-70-2	2.2	3	6.5	0.4	600	240	1.5	0.2	71.0	41.2
UZ-70-3	6.6	18	5.1	0.3	790	190	2.3	0.4	271.4	66.5
UZ-70-4	3.2	11	7.8	0.3	910	240	2.0	0.1	86.1	26.2
UZ-70-5	4.9	10	12.7	1.0	620	210	2.3	0.4	80.4	26.2
UZ-70-6	2.0	3	6.6	0.5	25900	9200	0.6	0.1	63.1	36.7
UZ-70-7	6.9	17	7.1	0.6	2270	710	1.8	0.6	203.2	52.6
UZ-70-8	13.2	26	11.0	0.6	4170	280	2.2	0.6	247.7	50.5
UZ-70-9	3.4	10	4.0	0.3	BLOD	BLOD	1.9	0.7	179.2	58.4
UZ-70-10	1.8	2	5.1	0.3	BLOD	BLOD	1.5	0.5	73.3	52.0
UZ-70-11	8.5	19	8.8	0.5	BLOD	BLOD	2.0	0.2	200.4	47.5
UZ-70-12	6.4	19	6.1	0.3	450	240	1.8	0.6	217.8	51.0
UZ-70-13	3.4	7	5.1	0.5	830	550	2.2	0.1	141.8	55.7
UZ-70-14	4.9	22	4.1	0.2	640	220	1.9	0.7	249.9	54.5
UZ-70-15	2.9	4	8.2	0.3	590	270	2.3	0.2	73.0	36.6
UZ-70-16	3.3	4	6.0	0.4	2400	1600	3.4	0.8	114.3	57.5
UZ-70-17	2.3	3	3.9	0.4	590	190	2.0	0.5	120.2	70.5
UZ-70-18	7.0	19	5.3	0.4	790	260	2.1	0.3	270.7	64.7
UZ-70-19	16.5	30	30.6	2.1	7670	600	2.6	0.8	113.3	22.1
UZ-70-20	11.0	23	13.9	0.9	3770	290	2.1	0.3	164.9	36.0
UZ-70-21	3.0	6	3.3	0.2	610	180	1.6	0.4	187.2	77.1
UZ-70-22	4.7	6	4.4	0.4	470	220	3.6	0.8	222.0	92.5
UZ-70-23	6.9	14	6.9	0.4	BLOD	BLOD	1.9	0.6	209.5	57.2
UZ-70-24	5.3	11	22.4	2.5	BLOD	BLOD	1.9	0.5	49.5	15.9
UZ-70-25	13.6	21	26.4	1.7	5420	600	2.4	0.7	107.8	24.5
UZ-70-26	5.9	7	4.0	0.3	6430	930	1.6	0.6	302.3	116.5
UZ-70-27	1.8	3	5.1	0.5	62300	5000	1.1	0.5	74.2	43.3
UZ-71-1	12.1	55	46.0	3.8	5380	680	1.8	0.4	53.8	7.2

UZ-71-2	5.8	7	12.0	2.1	1560	220	1.4	0.5	48.3	18.3
UZ-71-3	8.7	21	17.0	2.0	BLOD	BLOD	1.6	0.5	107.0	23.3
UZ-71-4	23.8	42	40.0	1.7	540	360	1.1	0.4	106.5	16.4
UZ-71-5	22.9	41	38.0	1.7	5180	290	1.9	0.2	110.5	17.3
UZ-71-6	9.2	32	29.0	3.2	500	180	1.6	0.9	59.7	10.6
UZ-71-7	36.2	127	86.0	2.4	11160	360	2.2	0.6	105.9	9.4
UZ-71-8	4.8	20	12.0	2.5	560	210	1.5	0.5	114.0	25.5
UZ-71-9	13.7	24	21.0	1.5	400	160	1.6	0.5	126.9	25.9
UZ-71-10	20.8	74	49.0	2.4	2580	360	1.8	0.3	109.0	12.7
UZ-71-11	6.2	18	12.0	1.9	800	160	1.4	0.2	132.5	31.2
UZ-71-12	20.5	41	35.0	1.7	BLOD	BLOD	1.2	0.3	116.4	18.2
UZ-71-13	3.7	11	7.0	1.9	630	230	1.5	0.6	140.9	42.5
UZ-71-14	3.5	12	10.0	2.9	770	330	1.0	0.2	71.6	20.7
UZ-71-15	6.2	17	13.0	2.1	720	190	1.4	0.2	106.2	25.8
UZ-71-16	17.6	31	29.0	1.7	2260	290	1.5	0.3	110.2	19.8
UZ-71-17	9.0	37	24.0	2.7	720	250	1.5	0.4	98.0	16.1
UZ-71-18	13.3	43	33.0	2.5	5170	360	1.6	0.3	89.6	13.7
UZ-71-19	18.7	65	47.0	2.5	2090	540	1.3	0.6	93.9	11.6
UZ-71-20	14.5	71	54.0	3.7	580	210	1.2	0.3	60.5	7.2
UZ-71-21	4.3	19	12.0	2.8	960	220	1.4	0.1	97.0	22.2
UZ-71-22	6.4	33	18.0	2.8	2350	260	1.5	0.2	110.1	19.2
UZ-71-23	22.6	51	39.0	1.7	34000	11000	1.9	0.3	128.7	18.0
UZ-71-24	5.1	16	13.0	2.5	1110	250	1.3	0.2	82.4	20.6
UZ-71-25	33.8	72	55.0	1.6	2610	220	1.6	0.4	136.9	16.1
UZ-71-26	7.0	17	12.0	1.7	BLOD	BLOD	1.2	0.2	141.1	34.2
UZ-71-27	3.5	11	8.0	2.3	810	240	1.5	0.6	103.7	31.3
UZ-71-28	14.3	54	45.0	3.2	11900	5500	1.4	0.6	65.0	8.9
UZ-71-29	2.1	7	5.0	2.4	2550	500	1.8	0.7	101.5	38.4
UZ-71-30	4.1	18	12.0	2.9	1040	260	1.4	0.1	87.2	20.6
UZ-71-31	3.1	8	7.0	2.2	1090	270	1.5	0.4	87.6	31.0
UZ-72-1	9.1	20	10.7	0.9	3000	940	0.9	0.2	201.8	48.2

UZ-72-2	7.1	23	6.4	0.4	1140	410	1.2	0.3	259.2	55.9
UZ-72-3	5.0	15	5.3	0.3	1670	560	1.4	0.7	224.8	59.2
UZ-72-4	4.8	19	6.1	0.3	970	580	1.0	0.2	185.0	43.6
UZ-72-5	50.1	145	89.3	6.1	BLOD	BLOD	1.2	0.3	132.8	14.3
UZ-72-6	6.3	18	9.2	0.6	BLOD	BLOD	1.4	0.7	162.0	39.8
UZ-72-7	7.8	33	8.1	0.5	1220	730	1.3	0.4	225.7	41.7
UZ-72-8	5.4	14	17.0	1.3	BLOD	BLOD	1.0	0.2	75.1	20.9
UZ-72-9	23.3	57	15.1	1.0	BLOD	BLOD	1.1	0.2	358.2	53.0
UZ-72-10	20.3	24	19.9	1.3	1440	610	1.1	0.2	239.6	51.4
UZ-72-11	4.9	14	9.1	0.5	1220	520	0.8	0.4	127.2	34.7
UZ-72-12	13.3	34	23.4	1.0	1680	610	1.0	0.2	134.8	23.8
UZ-72-13	5.6	21	13.0	0.7	1270	500	1.4	0.4	103.1	23.3
UZ-72-14	4.1	8	5.0	0.4	1300	550	1.1	0.2	194.3	70.0
UZ-72-15	2.6	7	5.4	0.3	1190	600	0.9	0.1	114.0	43.7
UZ-72-16	7.6	24	15.7	0.8	BLOD	BLOD	0.9	0.2	115.2	24.3
UZ-72-17	10.1	18	13.6	0.6	BLOD	BLOD	1.1	0.4	175.5	42.1
UZ-72-18	42.8	77	68.9	3.9	1530	490	1.3	0.4	146.7	18.7
UZ-72-19	4.8	13	9.9	0.4	1410	500	0.9	0.0	114.4	32.1
UZ-72-20	11.8	32	25.2	2.1	BLOD	BLOD	1.1	0.3	110.7	21.6
UZ-72-21	2.8	5	6.3	0.5	BLOD	BLOD	1.5	0.2	104.5	47.4
UZ-72-22	1.4	3	6.4	0.4	1670	540	1.2	0.3	52.8	30.7
UZ-72-23	9.2	20	6.3	0.3	BLOD	BLOD	1.1	0.3	337.8	77.6
UZ-72-24	4.5	7	10.9	0.6	BLOD	BLOD	0.8	0.2	98.3	37.5
UZ-72-25	5.7	12	4.5	0.3	1120	410	1.2	0.2	296.3	87.6
UZ-72-26	6.5	10	8.2	0.6	9000	2700	0.8	0.0	188.4	60.9
UZ-72-27	6.7	23	5.8	0.3	BLOD	BLOD	1.0	0.4	268.7	57.6
UZ-72-28	10.8	28	8.2	0.5	BLOD	BLOD	1.2	0.5	307.8	61.2
UZ-72-29	24.8	47	24.9	1.4	BLOD	BLOD	1.3	0.4	233.7	36.5
UZ-72-30	5.9	13	15.8	0.6	BLOD	BLOD	1.4	0.2	88.5	24.8
UZ-72-31	6.0	24	5.6	0.3	BLOD	BLOD	1.1	0.2	249.5	53.0
UZ-72-32	3.2	7	5.8	0.3	BLOD	BLOD	1.2	0.4	129.5	49.3

UZ-72-33	12.9	16	43.7	2.2	BLOD	BLOD	1.1	0.3	70.0	17.8
UZ-72-34	4.9	7	16.1	2.1	BLOD	BLOD	1.0	0.2	72.0	28.8
UZ-72-35	6.2	13	4.0	0.2	1410	450	0.9	0.2	359.5	101.6
UZ-72-36	4.4	12	7.6	0.4	1230	420	1.1	0.1	135.9	39.9
UZ-72-37	9.0	42	8.8	0.5	800	560	1.1	0.3	241.3	39.4
UZ-72-38	7.3	12	6.1	0.3	1520	540	1.3	0.2	279.7	82.1
UZ-72-39	2.2	8	6.8	0.4	1620	420	1.1	0.2	75.3	27.0
UZ-72-40	19.8	34	37.3	2.0	1120	420	1.2	0.5	125.5	22.5
UZ-72-41	4.6	14	4.9	0.3	1160	440	1.2	0.3	223.6	61.5
TK-31-1	89.2	191	115.7	8.7	3570	720	1.6	0.4	152.7	15.9
TK-31-2	63.3	342	109.4	7.0	3980	540	1.7	0.6	114.9	9.6
TK-31-3	94.1	462	92.2	4.8	3780	410	1.5	0.5	201.3	14.1
TK-31-4	79.4	295	86.2	6.0	2860	440	1.4	0.5	182.0	16.5
TK-31-5	88.7	176	194.0	12.0	3690	530	1.5	0.5	91.0	8.9
TK-31-6	73.0	209	128.1	8.6	3510	690	1.4	0.4	113.2	10.9
TK-31-7	106.0	299	248.0	15.0	3300	610	1.8	0.7	85.1	7.1
TK-31-8	100.0	292	140.4	9.9	4670	560	1.5	0.4	141.7	13.0
TK-31-9	58.7	201	113.7	6.3	3560	660	1.5	0.5	102.7	9.2
TK-31-10	100.0	987	226.0	18.0	4090	710	1.5	0.5	88.4	7.6
TK-31-11	106.0	436	204.0	12.0	3100	490	1.6	0.6	103.6	7.9
TK-31-12	98.6	371	126.1	6.6	3630	460	1.6	0.6	154.8	11.4
TK-31-13	119.0	874	220.0	13.0	4380	780	1.7	0.6	107.2	7.3
TK-31-14	51.3	189	58.4	3.3	3130	550	1.2	0.5	173.7	16.0
TK-31-15	57.8	340	104.4	5.4	3580	600	1.4	0.5	109.9	8.2
TK-31-16	103.0	347	183.0	11.0	2840	510	1.7	0.6	112.3	9.0
TK-31-17	81.0	197	111.8	6.0	3120	530	1.4	0.5	143.6	12.8
TK-31-18	125.0	456	256.0	19.0	3720	780	1.6	0.6	97.0	8.5
TK-31-19	66.3	773	97.0	6.6	3370	630	1.4	0.5	135.4	10.4
TK-31-20	85.8	305	160.8	9.7	3440	520	1.6	0.5	106.1	8.8
TK-31-21	119.0	469	185.7	9.9	2820	480	1.5	0.5	127.4	9.0
TK-31-22	79.1	405	104.0	14.0	3040	530	1.5	0.5	150.6	21.6

TK-31-23	90.4	365	120.6	7.6	3620	550	1.4	0.5	148.4	12.2
TK-31-24	92.5	363	178.0	14.0	4060	750	1.6	0.5	103.3	9.8
TK-31-25	106.0	375	160.0	11.0	3890	420	1.8	0.6	131.8	11.3
TK-31-26	86.8	513	133.1	8.7	3980	480	1.5	0.5	129.4	10.2
TK-31-27	126.0	474	187.0	11.0	2870	650	1.6	0.5	133.7	10.0
TK-31-28	78.5	185	88.9	8.1	2810	620	1.5	0.4	174.5	20.4
TK-31-29	100.0	264	114.5	8.6	3620	470	1.7	0.6	172.6	16.8
TK-31-30	103.0	429	160.7	8.9	3180	440	1.6	0.5	126.5	9.3
TK-31-31	80.7	236	145.1	7.3	3150	460	1.6	0.5	110.4	9.1
TK-31-32	104.0	453	145.0	11.0	3550	430	1.6	0.6	142.2	12.7
TK-31-33	97.5	504	121.3	9.6	3150	670	1.5	0.5	159.1	14.4
TK-31-34	90.6	462	109.8	6.8	3500	510	1.4	0.5	163.2	12.6
TK-31-35	82.5	535	129.8	8.6	2850	650	1.5	0.6	126.1	10.0
TK-31-36	99.6	767	144.9	7.4	3730	560	1.6	0.6	136.2	8.5
TK-31-37	109.0	540	126.3	9.6	2610	460	1.7	0.6	170.1	14.9
TK-31-38	89.5	396	93.4	7.2	3610	570	1.4	0.5	189.1	17.4
TK-31-39	97.2	251	170.0	14.0	3210	400	1.2	0.4	113.6	11.8
TK-31-40	87.4	603	103.8	5.1	3030	550	1.7	0.5	166.6	10.6
TK-36-1	29.6	244	23.8	1.6	1750	350	1.2	0.3	244.4	22.7
TK-36-2	10.5	60	7.9	1.0	1480	420	1.3	0.3	260.1	46.1
TK-36-3	19.2	143	13.3	0.7	1050	410	1.4	0.3	283.1	28.1
TK-36-4	23.0	291	25.0	1.7	1260	450	1.2	0.3	183.2	16.4
TK-36-5	13.6	35	11.4	0.6	870	450	1.5	0.2	234.4	41.3
TK-36-6	14.4	209	24.6	1.8	960	400	1.0	0.2	116.4	11.7
TK-36-7	28.1	95	16.1	0.8	1090	500	1.1	0.3	339.5	38.9
TK-36-8	19.5	115	22.8	1.8	830	600	1.2	0.3	169.2	20.7
TK-36-9	15.4	50	18.1	0.9	1360	400	1.4	0.3	168.3	25.4
TK-36-10	9.3	76	10.8	1.1	1400	540	1.2	0.4	170.8	26.2
TK-36-11	16.0	70	20.2	2.1	0	0	1.3	0.2	157.0	24.9
TK-36-12	10.7	85	9.0	0.7	0	0	1.2	0.3	233.0	31.3
TK-36-13	18.8	145	26.9	1.3	830	580	1.3	0.4	138.3	13.3

TK-36-14	12.3	62	11.6	0.6	870	350	1.2	0.3	210.0	28.6
TK-36-15	24.4	149	16.9	1.0	1110	350	1.3	0.3	282.8	28.1
TK-36-16	11.5	102	15.3	0.8	1680	390	1.2	0.4	149.4	16.7
TK-36-17	7.9	54	15.1	1.3	0	0	1.1	0.4	104.4	16.8
TK-36-18	16.5	170	34.1	2.2	1070	280	0.9	0.2	96.2	9.6
TK-36-19	28.5	133	22.1	2.2	0	0	1.2	0.3	253.2	33.4
TK-36-20	10.7	95	17.5	1.3	1650	350	1.1	0.2	121.0	15.3
TK-36-21	13.3	54	12.7	1.0	2090	790	1.1	0.2	206.3	32.2
TK-36-22	25.8	185	40.4	2.0	1440	440	1.0	0.3	126.7	11.2
TK-36-23	10.4	108	13.2	1.1	1290	600	1.1	0.2	156.3	19.9
TK-36-24	12.0	99	14.6	0.8	950	480	1.0	0.2	162.5	18.7
TK-36-25	11.8	61	11.8	0.8	0	0	1.4	0.2	198.0	28.5
TK-36-26	14.5	96	13.9	1.2	940	560	1.2	0.4	206.0	27.5
TK-36-27	17.9	156	20.3	1.0	1400	450	1.2	0.3	174.6	16.4
TK-36-28	9.7	25	7.9	0.3	1710	520	1.1	0.3	241.8	49.3
TK-37-1	26.2	71	27.4	2.2	5460	440	1.0	0.2	181.0	25.9
TK-37-2	17.8	45	22.0	1.8	5530	670	1.1	0.3	159.7	27.2
TK-37-3	19.7	107	31.4	2.1	2860	470	1.2	0.3	124.4	14.6
TK-37-4	20.5	50	30.0	1.7	4820	660	1.4	0.3	135.3	20.6
TK-37-5	15.5	38	43.7	3.1	5120	630	1.2	0.4	70.6	12.5
TK-37-6	12.7	61	24.1	1.5	4030	730	1.3	0.2	104.5	14.9
TK-37-7	9.4	34	26.0	1.7	3280	700	1.2	0.3	71.9	13.2
TK-37-8	12.1	29	32.1	1.9	6820	710	1.6	0.5	74.9	14.6
TK-37-9	14.1	41	26.1	1.4	5130	690	1.6	0.6	106.9	17.7
TK-37-10	14.9	34	26.3	2.7	2830	540	1.5	0.5	112.3	22.4
TK-37-11	11.0	39	22.4	1.8	3630	580	1.5	0.5	98.0	17.6
TK-37-12	14.6	58	18.9	1.1	3500	640	1.9	0.8	152.7	21.9
TK-37-13	17.2	63	27.5	1.9	3650	630	2.4	1.0	123.8	17.8
TK-37-14	17.6	37	31.6	1.7	2260	460	2.4	0.6	110.6	19.1
TK-37-15	21.1	90	23.9	2.0	4310	340	2.3	0.7	174.4	23.5
TK-37-16	14.5	46	30.9	2.1	2790	720	2.0	1.0	93.2	15.1

TK-37-17	14.2	87	26.5	1.5	2840	510	2.4	0.7	106.6	12.9
TK-37-18	13.6	41	22.2	1.6	3470	650	2.4	0.6	121.7	20.9
TK-37-19	11.1	48	16.4	1.3	3540	390	2.3	0.6	133.7	22.0
TK-37-20	11.4	94	25.6	1.6	4490	580	2.2	0.6	88.9	10.7
TK-37-21	14.2	32	30.1	1.9	3480	630	2.5	0.7	94.1	17.7
TK-37-22	17.7	32	34.7	3.8	5010	670	2.2	0.7	101.2	21.0
TK-37-23	8.5	36	28.9	1.4	2850	580	2.4	0.9	65.9	11.4
TK-37-24	17.8	74	23.1	1.3	3040	500	2.2	0.8	152.3	19.7
TK-37-25	11.4	46	31.9	1.9	2550	400	1.6	0.6	71.0	11.3
TK-37-26	8.6	45	24.5	2.0	2690	690	1.5	0.5	69.8	11.9
TK-37-27	8.6	25	31.1	1.9	4240	640	1.5	0.5	76.7	16.0
TK-37-28	8.3	45	21.6	1.5	3840	550	1.9	0.8	76.2	12.5
TK-37-29	10.1	25	17.9	0.9	2860	380	2.4	1.0	112.2	23.1
TK-37-30	9.3	41	27.0	1.8	2440	630	2.4	0.6	69.0	11.7
TK-37-31	15.4	69	25.3	2.1	1990	460	2.3	0.7	120.7	17.6
TK-37-32	13.1	97	24.7	1.5	2800	390	1.5	0.5	105.3	12.5
TK-37-33	12.4	41	25.2	1.6	4110	410	1.9	0.8	98.0	16.5
TK-37-34	10.7	46	17.7	1.0	1930	380	2.4	1.0	119.8	18.9
TK-37-35	7.0	80	26.4	2.2	4400	760	2.4	0.6	65.6	9.1
TK-40-1	2.1	49	29.6	3.0	BLOD	BLOD	1.1	0.2	164.0	23.7
TK-40-2	8.8	80	26.4	2.6	BLOD	BLOD	1.2	0.3	309.4	44.0
TK-40-3	2.3	67	30.7	3.1	BLOD	BLOD	1.3	0.5	129.1	16.0
TK-40-4	8.3	88	32.5	3.3	BLOD	BLOD	1.1	0.6	185.7	25.1
TK-40-5	7.0	61	36.3	3.6	BLOD	BLOD	1.2	0.4	173.4	25.3
TK-40-6	1.2	55	33.2	3.3	BLOD	BLOD	1.6	0.5	117.7	15.9
TK-40-7	2.0	132	27.8	2.8	BLOD	BLOD	1.5	0.2	118.1	10.5
TK-40-8	2.3	63	33.7	3.4	BLOD	BLOD	1.7	0.4	132.5	17.0
TK-40-9	1.9	91	31.2	3.1	BLOD	BLOD	1.2	0.7	115.1	12.3
TK-40-10	2.4	43	26.0	2.6	BLOD	BLOD	1.3	0.4	85.9	13.3
TK-40-11	1.7	63	36.7	3.7	BLOD	BLOD	1.4	0.2	106.8	13.6
TK-40-12	2.7	55	38.6	3.9	BLOD	BLOD	1.6	0.3	98.5	13.5

TK-40-13	1.9	83	26.8	2.7	BLOD	BLOD	1.5	0.5	120.3	13.4
TK-40-14	1.8	49	33.9	3.4	BLOD	BLOD	1.7	0.4	100.0	14.4
TK-40-15	1.9	63	31.9	3.2	BLOD	BLOD	1.4	0.1	163.0	20.8
TK-40-16	2.5	51	33.0	3.3	BLOD	BLOD	2.0	0.2	106.8	15.2
TK-40-17	2.2	23	32.6	3.3	BLOD	BLOD	1.1	0.8	70.4	14.8
TK-41-1	33.5	266	49.0	2.5	9970	590	2.4	0.9	121.0	9.7
TK-41-2	29.3	104	26.4	1.2	12890	710	1.9	0.3	179.4	19.4
TK-41-3	25.3	63	21.6	1.1	11450	610	2.8	0.8	184.6	25.1
TK-41-4	30.6	156	29.2	1.9	11700	620	2.0	0.6	181.2	18.7
TK-41-5	34.4	260	29.9	1.7	8890	470	1.9	0.8	204.2	17.2
TK-41-6	19.6	68	37.1	2.0	10190	650	2.4	1.0	105.0	13.9
TK-41-7	38.0	162	45.1	2.1	9730	720	2.4	0.6	166.6	15.2
TK-41-8	27.5	178	31.2	1.3	9130	520	2.3	0.7	174.4	15.0
TK-41-9	25.9	129	34.1	1.6	11090	590	2.0	1.0	150.3	15.0
TK-41-10	28.5	231	31.3	1.9	8930	820	2.4	0.7	179.9	16.1
TK-41-11	24.5	142	26.9	1.6	12200	550	2.4	0.6	179.8	18.5
TK-41-12	24.0	117	26.6	1.0	11450	530	2.3	0.6	178.1	17.8
TK-41-13	26.8	153	22.2	1.3	5290	470	2.2	0.6	206.7	20.6
TK-41-14	29.6	133	30.5	1.7	13050	750	2.5	0.7	191.8	19.8
TK-41-15	33.5	229	37.7	1.5	14950	980	2.2	0.7	175.5	13.5
TK-41-16	29.5	307	34.8	2.4	10150	860	2.4	0.9	167.6	15.0
TK-41-17	18.7	97	22.7	1.3	10700	510	2.2	0.8	162.9	19.0
TK-41-18	15.3	78	20.9	1.1	11990	830	2.4	0.5	145.0	18.1
TK-41-19	30.7	130	29.0	1.9	10990	850	1.8	0.3	208.5	22.8
TK-41-20	35.3	216	36.5	2.4	10870	720	2.3	0.6	190.7	18.0
TK-41-21	31.1	104	29.9	2.2	12410	930	1.9	0.0	205.2	25.2
TK-41-22	29.8	171	33.7	2.4	12800	1000	2.9	1.3	175.0	18.3
TK-41-23	25.4	138	27.8	1.3	13260	820	2.2	0.4	180.8	17.6
TK-41-24	30.5	163	40.1	2.6	11880	750	2.1	0.8	150.5	15.3
TK-41-25	16.6	66	20.5	1.5	6740	570	2.2	0.6	160.1	22.9
TK-41-26	22.8	133	27.3	2.0	9950	930	2.2	1.2	164.9	18.7

TK-41-27	5.7	25	7.8	0.4	10110	940	1.5	0.7	143.6	29.6
TK-41-28	34.7	139	39.2	2.7	14110	820	2.4	0.7	174.8	19.1
TK-41-29	19.3	78	31.9	2.1	11590	850	3.1	0.1	120.3	15.8
TK-41-30	21.8	138	27.8	1.9	13200	1200	2.3	0.6	155.3	17.0
TK-41-31	18.6	77	32.6	1.6	13000	950	1.6	0.8	113.6	14.1
TK-41-32	30.8	150	42.0	2.0	13310	990	2.3	0.5	145.3	13.7
TK-41-33	39.2	139	53.2	3.5	12340	840	2.2	0.6	146.0	15.7
TK-41-34	14.7	59	26.4	1.7	15400	980	3.4	0.8	110.7	16.1
TK-48-1	6.3	47	6.2	0.3	930	93	1.0	0.2	197.9	30.5
TK-48-2	6.6	50	7.1	0.4	BLOD	BLOD	1.2	0.3	184.4	28.0
TK-48-3	7.3	31	11.9	0.7	BLOD	BLOD	1.0	0.2	121.8	23.1
TK-48-4	5.0	24	5.9	0.3	1170	117	0.9	0.2	167.3	35.1
TK-48-5	8.4	93	26.5	1.2	1300	130	1.1	0.3	62.9	7.1
TK-48-6	7.5	47	6.6	0.4	BLOD	BLOD	1.0	0.3	222.3	35.1
TK-48-7	2.3	21	8.2	0.4	BLOD	BLOD	0.8	0.3	54.9	12.2
TK-48-8	5.1	29	5.7	0.3	1690	169	1.1	0.2	175.5	34.1
TK-48-9	6.1	25	25.8	1.2	BLOD	BLOD	1.2	0.4	47.3	9.7
TK-48-10	6.3	49	12.0	0.8	BLOD	BLOD	1.1	0.2	104.4	16.4
TK-48-11	7.5	35	7.8	0.5	1140	114	1.3	0.3	191.2	34.7
TK-48-12	5.2	33	6.3	0.3	BLOD	BLOD	1.1	0.2	162.9	29.7
TK-48-13	5.5	13	5.4	0.2	2740	274	1.0	0.2	201.1	56.5
TK-48-14	4.9	14	8.9	0.4	BLOD	BLOD	1.0	0.2	108.4	29.3
TK-48-15	6.6	34	7.0	0.4	1030	103	1.0	0.2	187.1	34.0
TK-48-16	4.2	18	9.9	0.6	BLOD	BLOD	0.9	0.3	85.1	20.7
TK-48-17	9.0	65	8.2	0.4	BLOD	BLOD	1.0	0.2	216.6	29.0
TK-48-18	5.5	43	15.6	0.8	1170	117	1.1	0.2	70.4	11.3
TK-48-19	7.0	34	9.9	0.4	1270	127	1.0	0.2	139.8	24.7
TK-48-20	5.2	17	11.6	0.4	1050	105	1.0	0.2	89.2	21.9
TK-48-21	4.4	31	8.9	0.5	BLOD	BLOD	1.2	0.4	97.3	18.4
TK-48-22	6.7	42	13.6	0.6	1210	121	1.0	0.3	98.4	15.8
TK-49-1	1.7	4	5.9	0.3	570	310	1.4	0.8	40.4	20.3

TK-49-2	1.6	4	5.6	0.3	BLOD	BLOD	0.7	0.0	28.3	14.2
TK-49-3	5.8	34	15.3	0.9	BLOD	BLOD	1.0	0.2	114.5	20.8
TK-49-4	2.6	5	34.7	7.3	211000	29000	1.0	0.5	11.5	5.7
TK-49-5	3.4	2	7.8	0.5	BLOD	BLOD	0.8	0.2	49.3	35.0
TK-49-6	3.2	12	4.1	0.3	BLOD	BLOD	0.9	0.1	131.2	39.1
TK-49-7	3.4	7	16.0	1.3	BLOD	BLOD	1.1	0.3	49.5	19.1
TK-49-8	9.6	13	59.6	3.4	BLOD	BLOD	1.1	0.2	9.2	2.6
TK-49-9	2.8	6	14.8	0.8	BLOD	BLOD	1.1	0.2	26.5	10.9
TK-49-10	2.0	8	61.0	3.2	BLOD	BLOD	0.1	0.2	7.3	2.6
TK-50-1	1.4	7	12.0	0.8	1180	380	0.6	0.0	21.4	8.2
TK-50-2	1.0	3	11.9	1.1	1750	680	1.3	0.1	17.4	10.2
TK-50-3	0.4	1	6.3	0.6	1370	290	2.0	0.2	11.6	11.7
TK-50-4	0.9	2	20.7	1.8	BLOD	BLOD	1.5	0.3	8.8	6.3
TK-50-5	1.6	4	4.6	0.3	1160	430	1.0	0.1	68.6	34.5
TK-50-6	0.3	1	5.4	0.4	BLOD	BLOD	1.2	0.4	11.0	11.0
TK-50-7	1.6	8	21.1	1.5	1640	390	1.5	0.4	15.1	5.5
TK-50-8	2.3	5	10.7	1.1	BLOD	BLOD	1.3	0.6	42.3	19.4
TK-50-9	2.7	11	17.9	1.3	1760	370	0.7	0.5	30.6	9.5
TK-50-10	1.8	11	8.5	0.4	1620	370	1.7	0.9	42.4	12.9
TK-50-11	2.8	4	14.7	1.4	2090	470	1.2	0.1	38.1	19.4
TK-50-12	2.8	10	8.2	0.5	2340	670	1.1	0.2	65.7	21.1
TK-50-13	0.6	1	12.1	0.8	1100	350	1.5	0.3	10.2	10.2
TK-50-14	1.5	5	10.4	0.8	1050	560	1.8	0.1	27.8	12.6
TK-50-15	1.8	12	4.8	0.3	1310	390	1.3	0.5	73.7	21.8
TK-50-16	1.3	5	7.9	0.4	BLOD	BLOD	1.2	0.6	32.5	14.6
TK-50-17	0.9	5	6.0	0.4	2050	380	1.2	0.2	29.0	13.1
TK-50-18	2.2	6	15.4	1.0	1350	640	0.8	0.3	28.9	11.9
TK-50-19	2.3	8	9.4	0.6	1760	360	1.1	0.4	48.3	17.4
TK-50-20	1.4	5	6.1	0.4	1280	450	1.1	0.3	46.2	20.8
TK-50-21	1.4	4	12.6	0.7	1620	480	1.2	0.2	22.4	11.3
TK-50-22	0.7	1	9.0	0.5	1100	520	1.1	0.1	14.7	14.7

TK-50-23	0.8	2	25.0	2.2	1520	590	1.3	0.5	6.6	4.7
TK-50-24	0.5	1	7.5	0.6	2340	320	1.7	0.4	13.8	13.8
TK-50-25	3.0	12	17.2	1.1	1700	480	1.2	0.3	34.3	10.1
TK-50-26	0.7	2	6.6	0.4	1350	500	1.4	0.4	22.5	16.0
TK-50-27	2.3	4	6.8	0.4	2300	410	0.7	0.6	66.9	33.7
TK-50-28	3.2	11	12.5	0.8	1500	380	1.1	0.4	50.9	15.7
TK-50-29	3.6	15	10.8	0.7	2320	520	1.3	0.5	65.7	17.5
TK-50-30	0.9	2	8.9	0.5	910	400	1.3	0.4	19.5	13.9
TK-50-31	2.8	5	20.1	2.4	1380	440	1.4	0.5	28.1	13.0
TK-50-32	0.2	1	10.9	1.1	1560	500	1.4	0.4	4.1	4.1
TK-50-33	0.5	2	7.4	0.4	1480	370	1.3	0.2	12.9	9.1

8.2 Supplementary File 2: Zircon and Apatite Helium data

Supplementary File 2: Single grain zircon (U–Th–Sm)/He and apatite (U–Th–Sm)/He age and chemistry data. For single grain analysis, see Table 2. Concentrations of thorium, uranium and samarium in ng. He is the concentration of helium measured in ncc. Th/U is the ratio of thorium to uranium. Raw age is the age before the F_T correction is made. F_T is the alpha-ejection correction parameter of Farley et al. (1996). Cor. age is the age after applying the F_T correction, and TAU is the total analytical uncertainty.

Sample	^{232}Th	±(%)	^{238}U	±(%)	^{147}Sm	±(%)	He	±(%)	TAU(%)	Th/U	Raw age	±1σ	F_T	Cor. age	±1σ
Zircon (U-Th-Sm)/He Data															
TK-42-1	0.555	1.4	1.212	1.9	0.002	26.1	28.120	1.8	2.5	0.45	169.6	4.2	0.64	265.7	13.5
TK-42-2	1.408	1.4	4.501	2.0	0.003	2.0	68.269	0.7	2.0	0.31	115.0	2.3	0.71	161.6	8.8
TK-42-3	1.033	1.4	1.586	1.9	0.001	27.5	46.088	0.6	1.8	0.65	203.5	3.6	0.72	281.7	15.4
TK-42-4	1.530	1.4	3.434	1.9	0.003	17.2	70.073	0.8	1.9	0.44	149.9	2.9	0.72	206.9	11.5
TK-36-1	2.347	1.4	7.770	2.0	0.005	6.6	179.440	0.7	2.0	0.30	174.5	3.5	0.80	216.9	13.4
TK-36-2	0.924	1.4	2.900	1.9	0.002	21.7	71.820	0.6	1.9	0.32	186.2	3.5	0.73	256.6	14.2
TK-36-3	1.022	1.4	4.638	1.9	0.001	4.9	109.085	0.6	1.9	0.22	180.8	3.5	0.70	256.6	13.8
TK-36-4	0.753	1.4	3.496	1.9	0.001	11.9	73.653	0.6	1.9	0.21	162.4	3.1	0.66	247.4	23.6
Apatite (U-Th-Sm)/He Data															
TK-40-1	0.620	5.7	0.253	5.8	0.076	0.3	4.001	8.6	9.6	2.43	81.8	7.8	0.75	156.0	12.6
TK-40-2	0.242	4.0	0.112	4.3	0.030	0.3	1.759	6.2	6.9	2.16	85.1	5.9	0.67	127.3	10.4
TK-40-3	0.717	5.7	0.290	5.9	0.081	0.4	6.295	4.5	6.2	2.46	111.8	6.9	0.76	146.4	12.7
TK-41-1	0.211	5.7	0.079	5.8	0.030	0.4	1.524	3.5	5.5	2.63	96.3	5.3	0.72	133.3	10.2
TK-41-2	0.046	4.1	0.017	4.2	0.012	0.4	0.110	3.4	4.6	2.71	32.3	1.5	0.56	57.9	3.1
TK-41-3	0.173	5.7	0.104	5.9	0.021	0.4	1.399	0.9	4.6	1.65	78.7	3.6	0.67	118.4	7.6
TK-36-1	0.127	4.0	0.123	4.2	0.016	0.3	1.075	3.8	5.2	1.03	57.5	3.0	0.75	76.9	5.9
TK-36-2	0.118	5.7	0.089	5.9	0.017	0.4	1.775	1.5	4.9	1.31	123.2	6.0	0.62	197.9	12.3
TK-36-3	0.071	4.1	0.079	4.2	0.014	0.4	1.591	2.8	4.5	0.90	135.2	6.1	0.70	192.8	21.2
TK-36-4	0.088	4.1	0.092	4.2	0.014	0.4	1.737	1.5	3.8	0.96	125.2	4.8	0.73	170.6	19.1
TK-36-5	0.080	5.7	0.083	5.8	0.010	0.4	1.386	3.8	6.2	0.96	111.2	6.9	0.73	153.3	18.7
UZ-69-1	0.052	3.3	0.022	3.5	0.012	0.4	0.038	2.7	3.7	2.37	9.1	0.3	0.55	16.7	1.8
UZ-69-2	0.081	4.6	0.042	4.7	0.017	0.3	0.055	2.2	4.2	1.90	7.4	0.3	0.55	13.4	1.4
UZ-69-3	0.173	3.3	0.085	3.5	0.033	0.3	0.141	1.1	2.8	2.02	9.2	0.3	0.72	12.8	0.7
UZ-69-4	0.111	3.3	0.051	3.5	0.022	0.3	0.075	2.4	3.5	2.16	8.0	0.3	0.51	15.7	1.7
UZ-69-5	0.140	4.6	0.056	4.7	0.027	0.3	0.066	3.5	4.9	2.51	6.1	0.3	0.66	9.2	0.6
TK-50-1	0.242	3.3	0.138	3.5	0.077	0.2	0.475	5.1	5.7	1.74	19.9	1.1	0.74	27.0	2.1
TK-50-2	0.078	4.6	0.043	4.7	0.029	0.3	0.075	1.2	3.8	1.78	9.9	0.4	0.70	14.1	0.9
TK-50-3	0.090	4.6	0.058	4.7	0.029	0.2	0.084	1.1	3.8	1.55	8.6	0.3	0.69	12.5	0.8
TK-50-4	0.065	3.3	0.029	3.5	0.030	0.3	0.066	1.3	2.9	2.23	12.3	0.4	0.64	19.2	1.1
TK-49-1	0.030	4.6	0.022	4.7	0.007	0.4	0.046	3.2	4.9	1.33	12.9	0.6	0.54	24.1	2.7
TK-49-2	0.023	3.3	0.014	3.5	0.006	0.4	0.035	1.5	3.1	1.56	14.2	0.4	0.47	30.6	3.2
TK-49-3	0.089	4.6	0.054	4.7	0.014	0.4	0.068	1.4	3.9	1.66	7.5	0.3	0.54	13.8	1.5
TK-49-4	0.112	3.3	0.083	3.5	0.024	0.3	0.374	3.3	4.3	1.34	28.0	1.2	0.68	41.4	2.7

8.3 Supplementary File 3: Apatite Fission Track Radial Plots

Supplementary File 3a: Single grain apatite fission track data for samples taken from the Chatkal-Kurama terrane plotted using Vermeesch (2009). Single grain ages are coloured according to their respective chlorine (Cl) measurements, or uranium (U) measurements.

Chamgin Radial Plots (1)

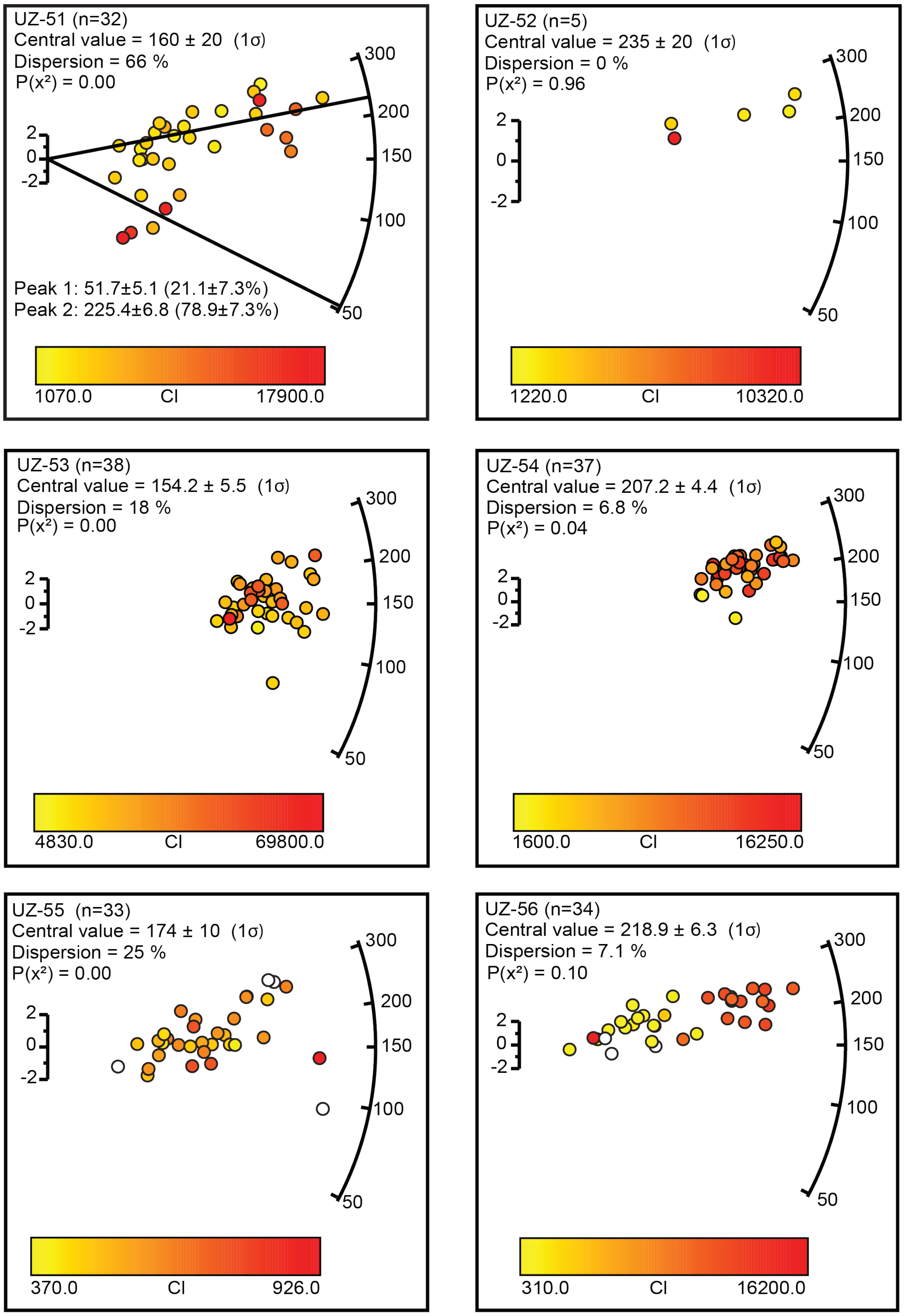

Supplementary File 3b:

Chamgin Radial Plots (2)

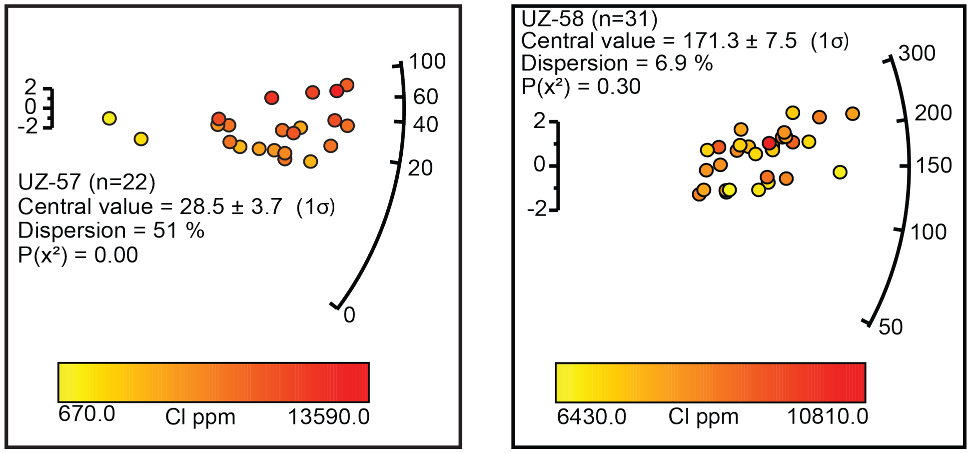

Supplementary File 3c:

Kamchik Pass Radial Plots

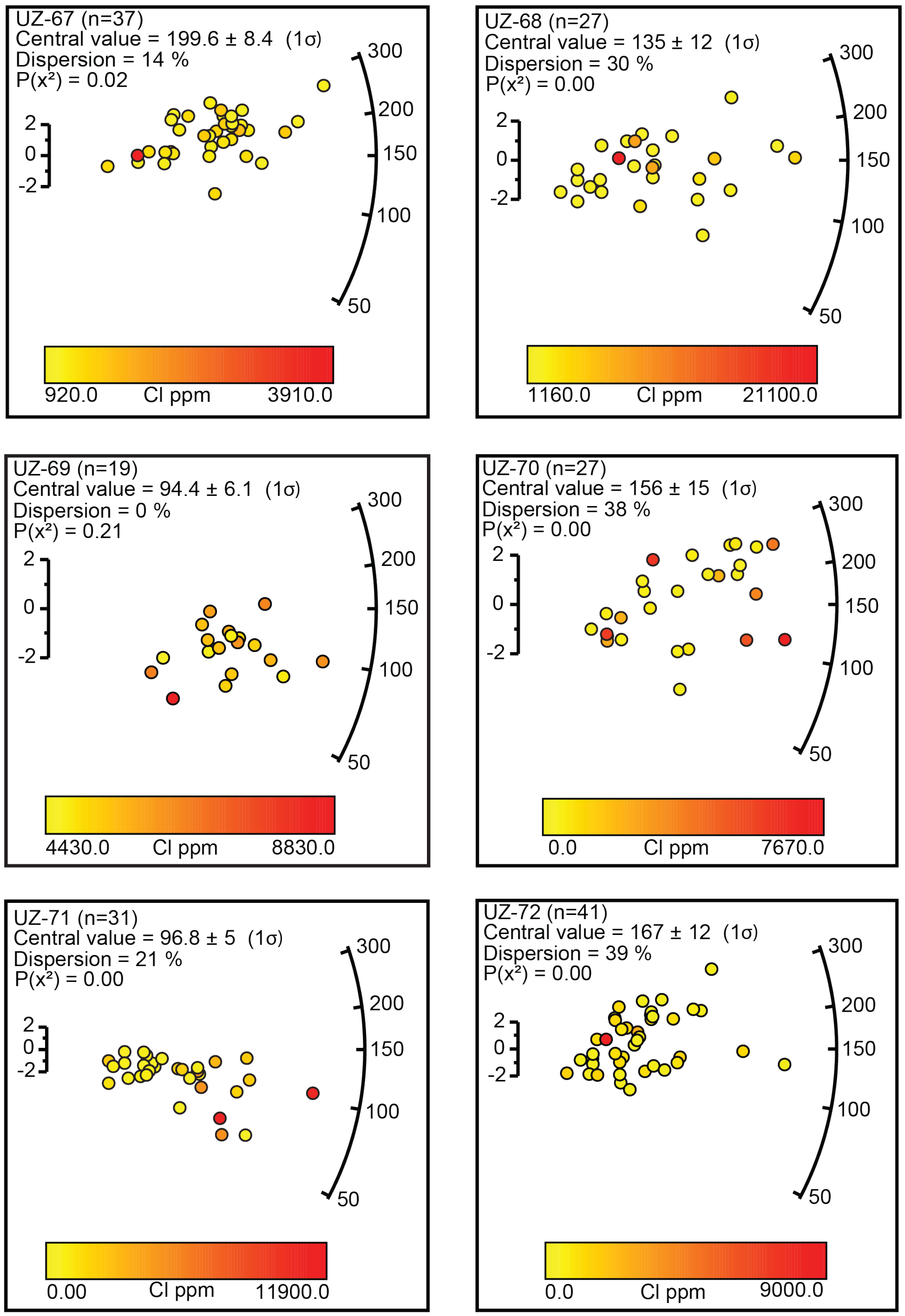

Supplementary File 3d:

Almalyk Radial Plots (1)

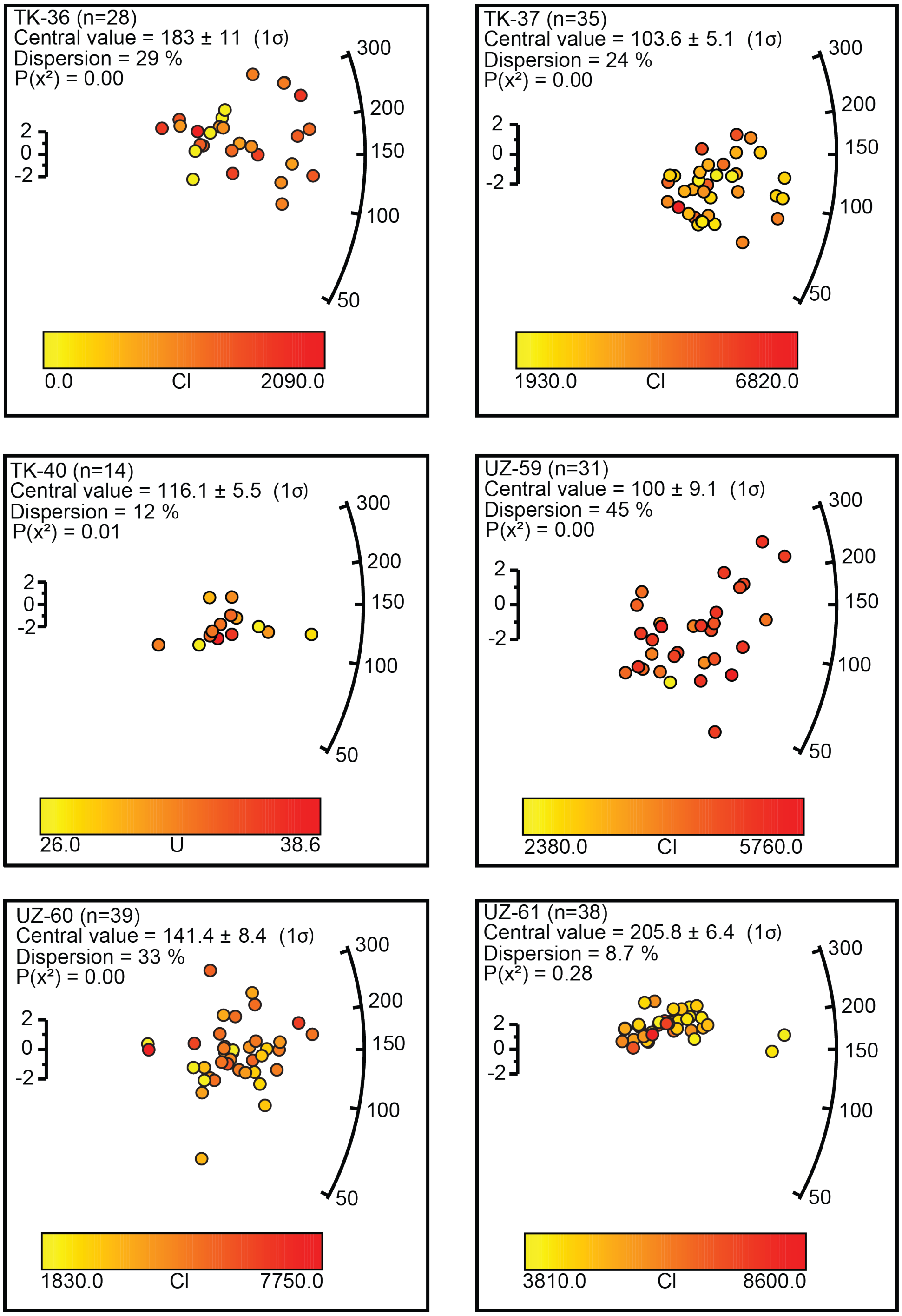

Supplementary File 3e:

Almalyk Radial Plots (2)

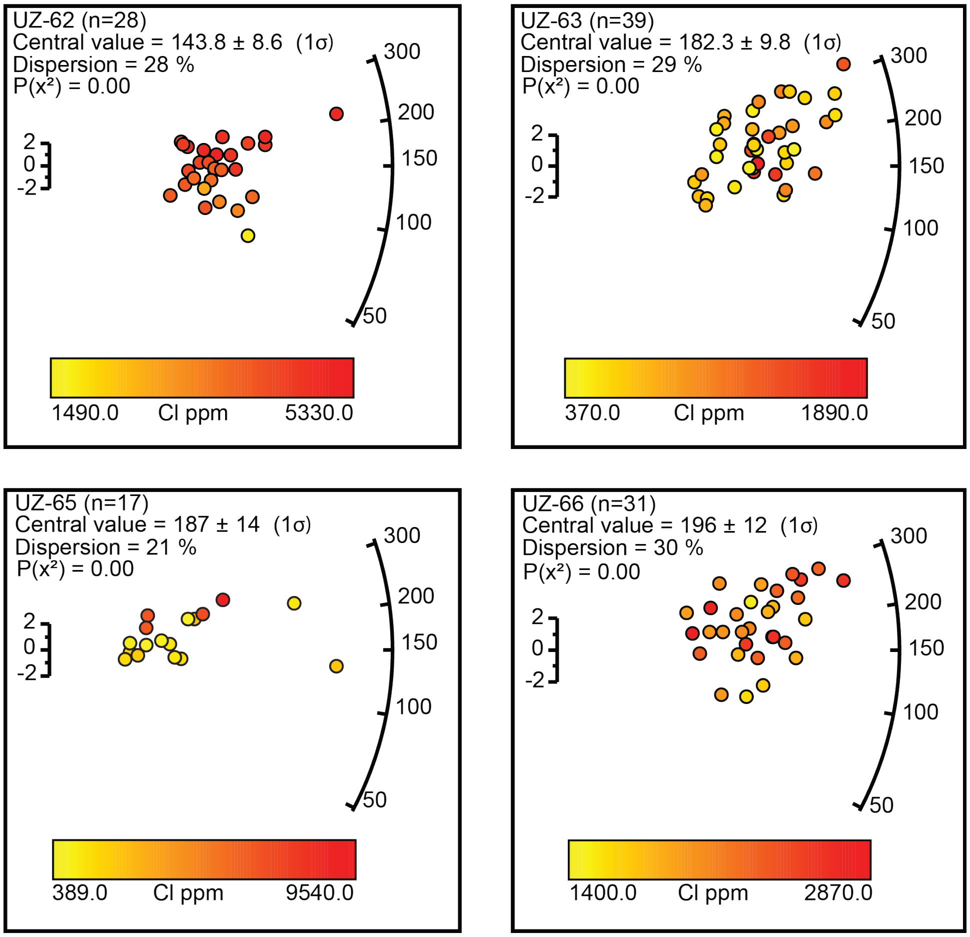

Supplementary File 3f:

Shaydon Radial Plots

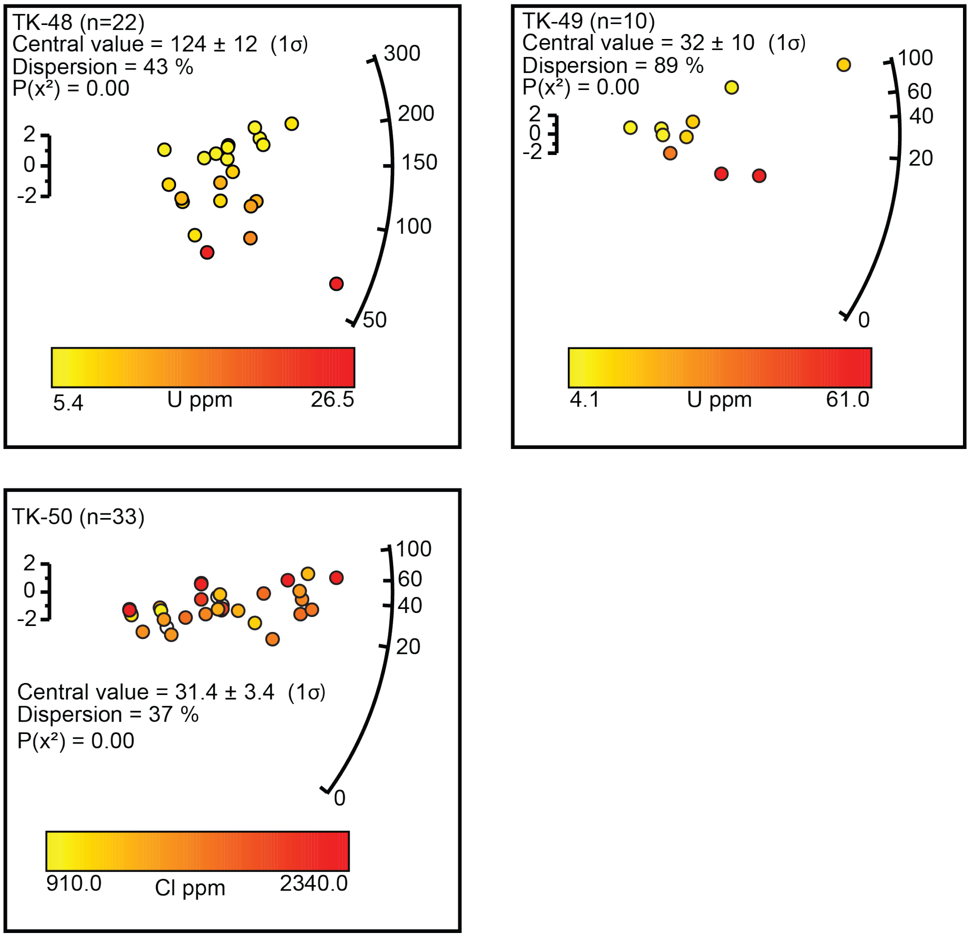

Supplementary File 3g:

Shaydon Radial Plots

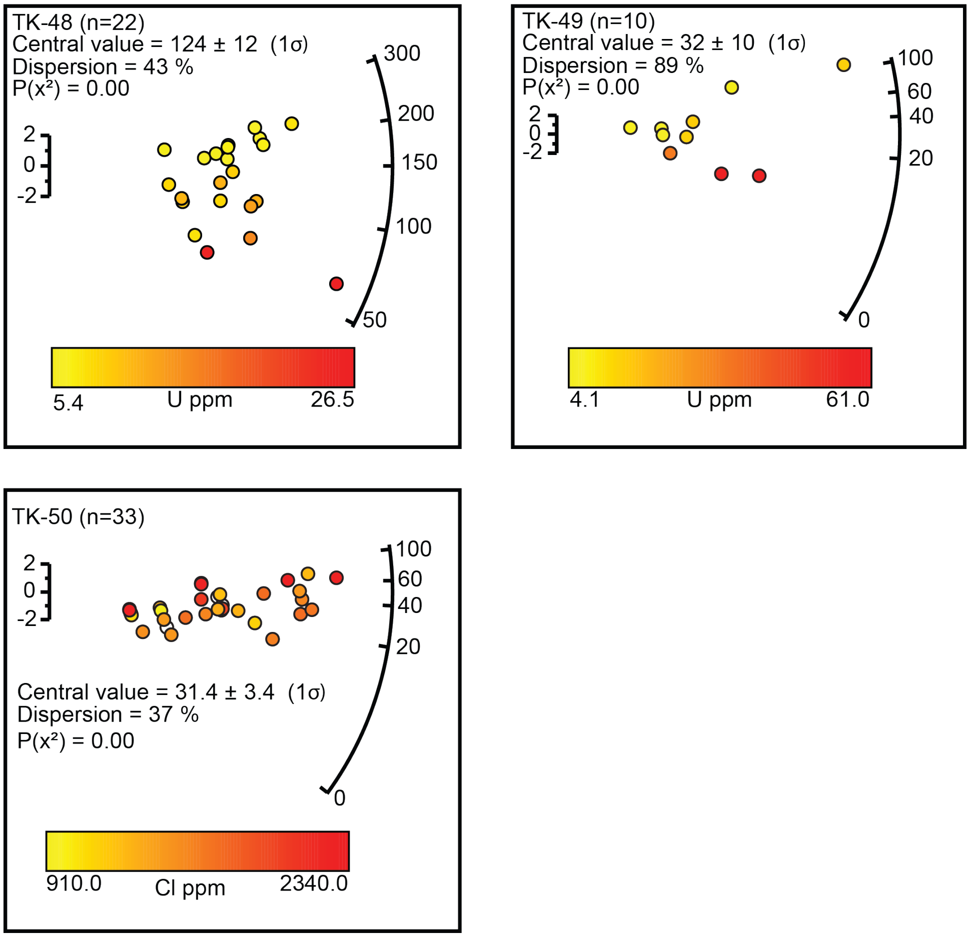

8.4 Supplementary File 4: Confined Length Histograms

Supplementary File 4a: Confined fission track length histograms for each sample in the Chatkal-Kurama region.

Chimgan Histograms (1)

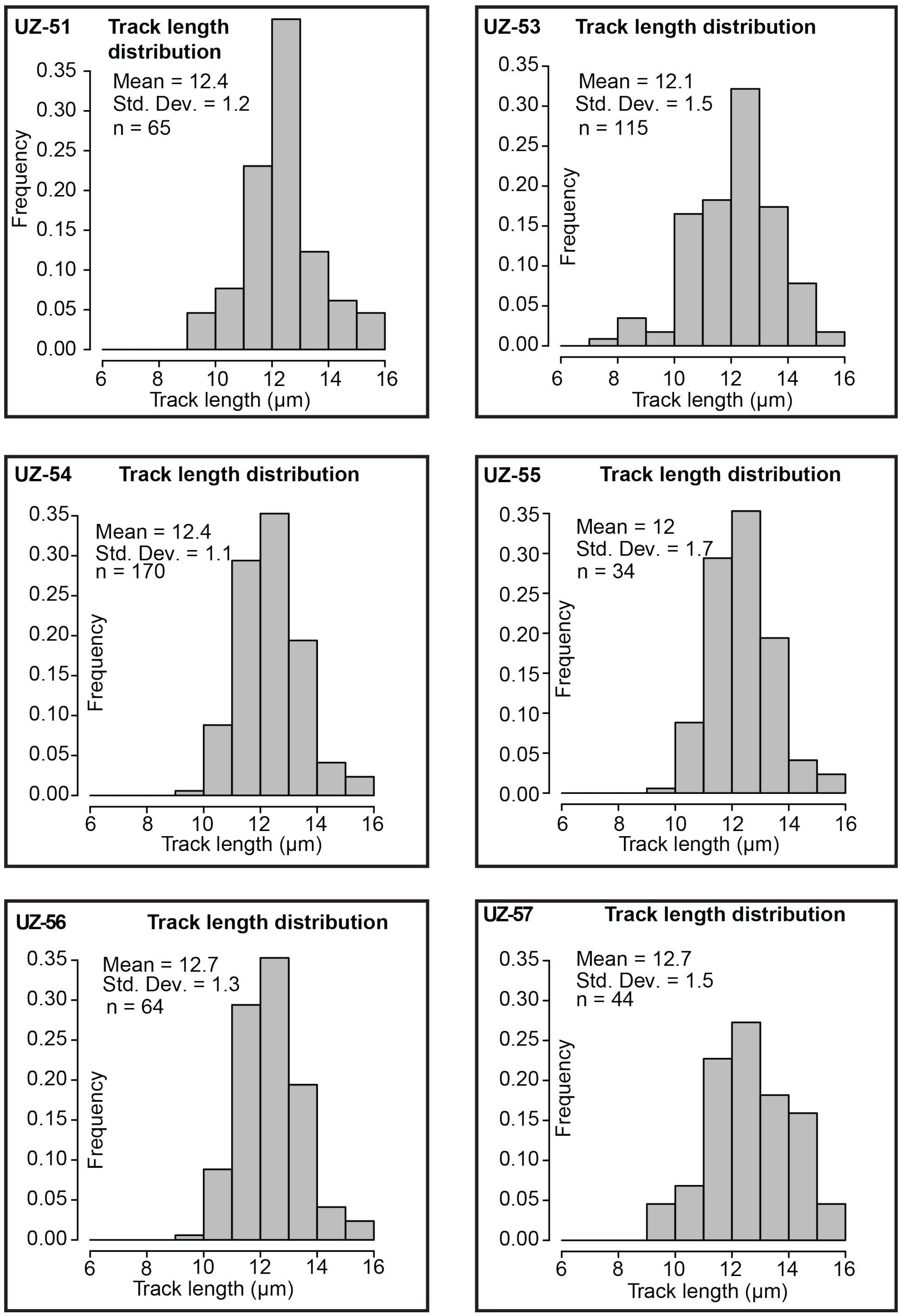

Supplementary File 4b:

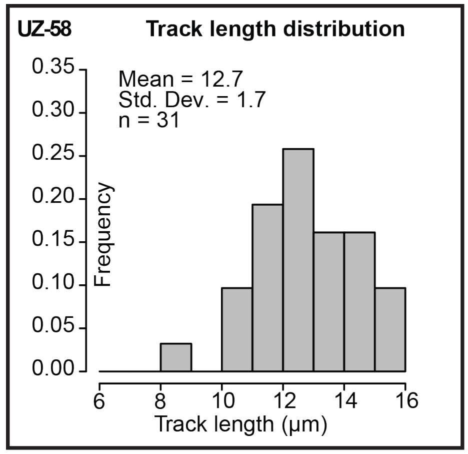

Supplementary File 4c:

Kamchik Pass Histograms

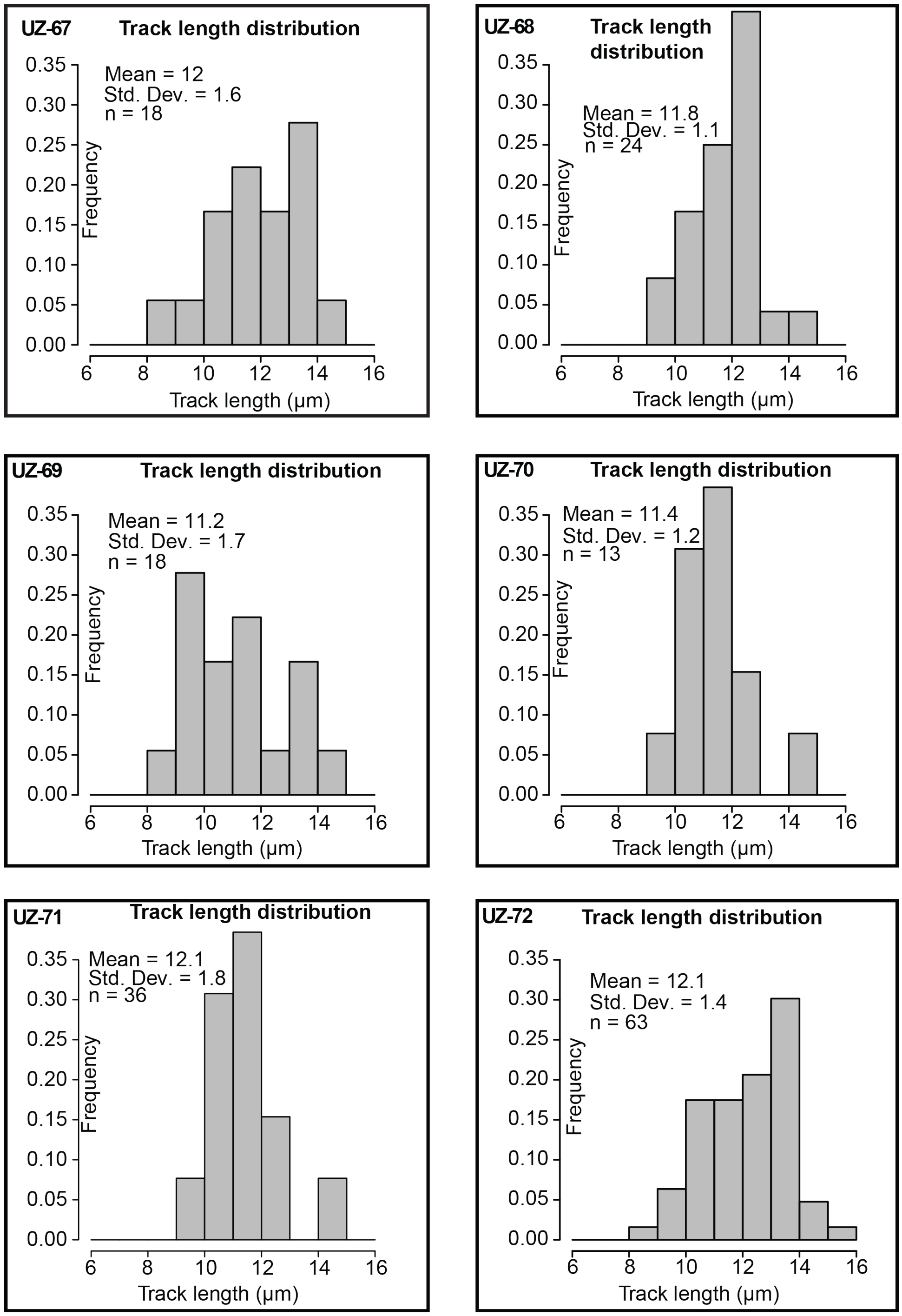

Supplementary File 4d:

Almalyk Histograms (1)

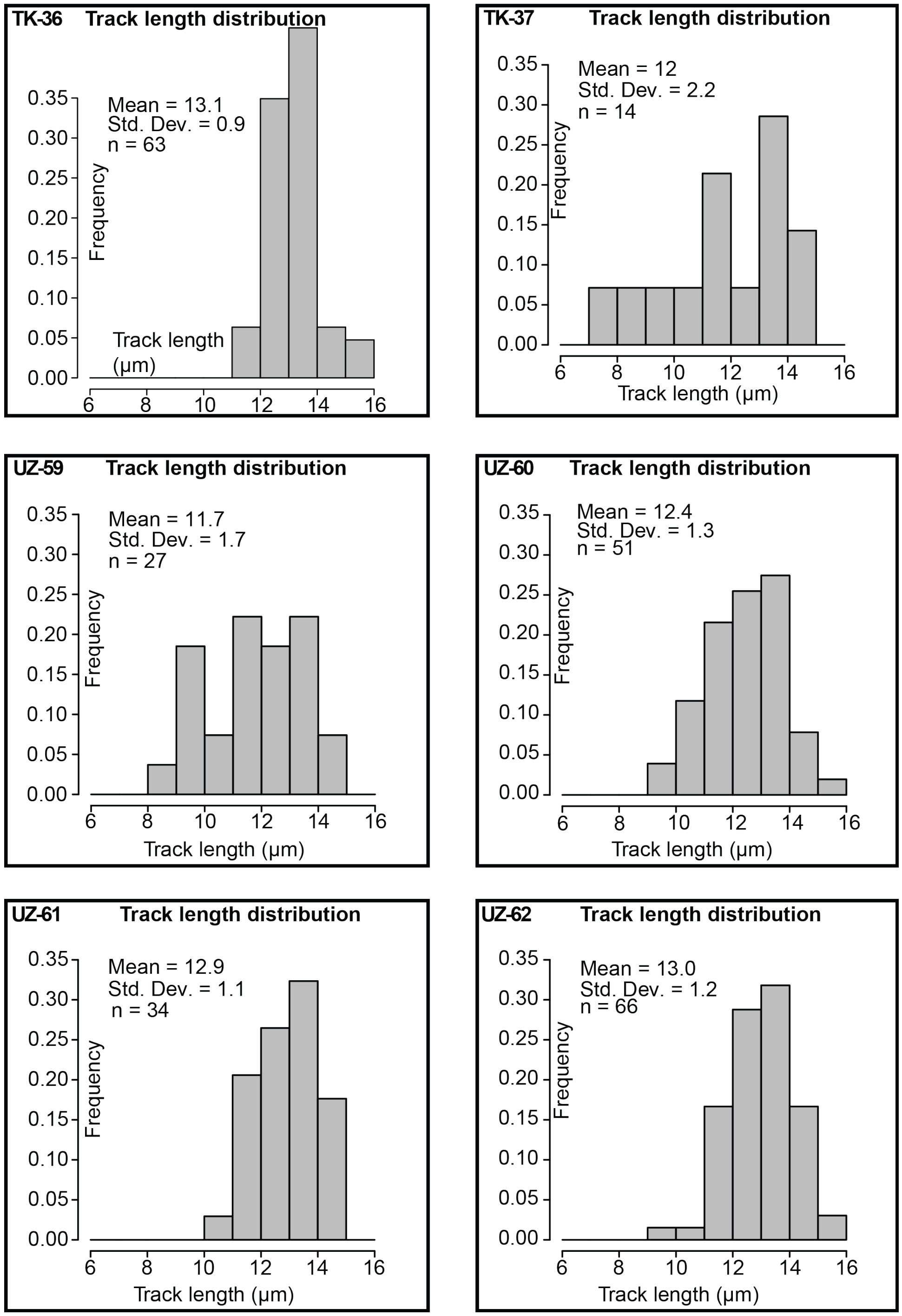

Supplementary File 4e:

Almalyk Histograms (2)

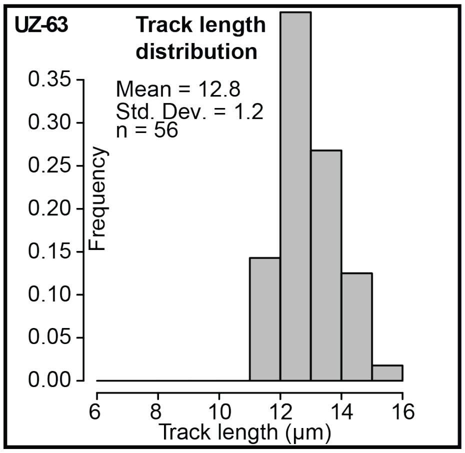

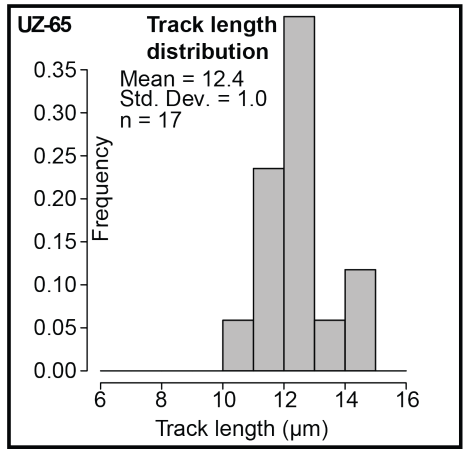

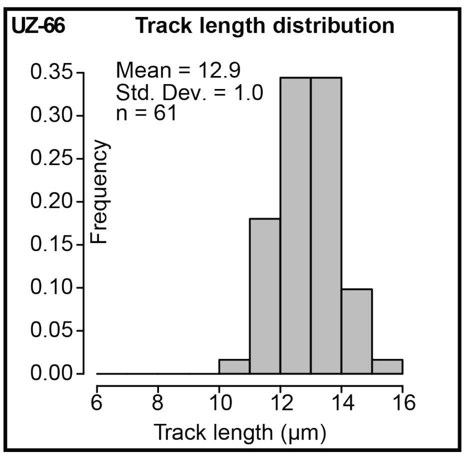

Supplementary File 4f:

Shaydon Histograms

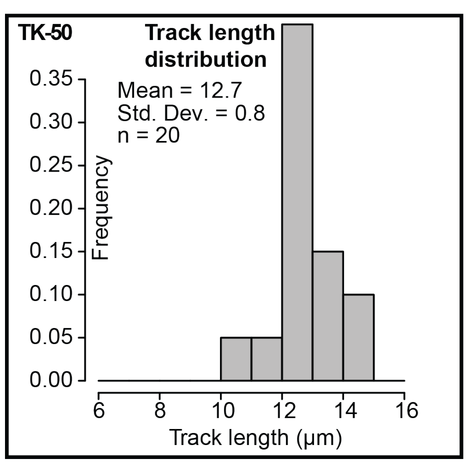

Supplementary File 4g:

Khujand Histograms

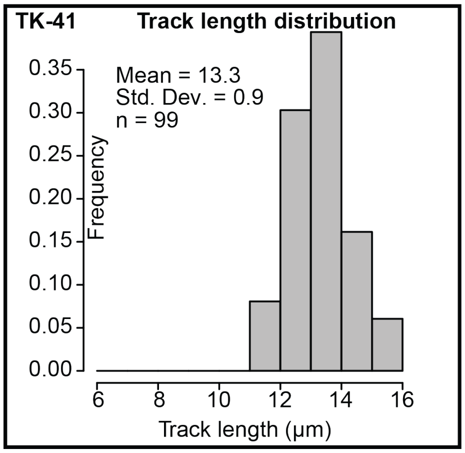

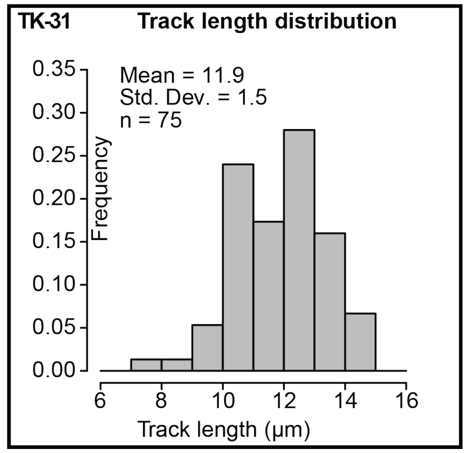

8.5 Supplementary File 5: Thermal History Models

Supplementary File 5a: Individual time-temperature plots for each sample modelled using Gallagher (2012). For modelling parameters see Supplementary File 6.

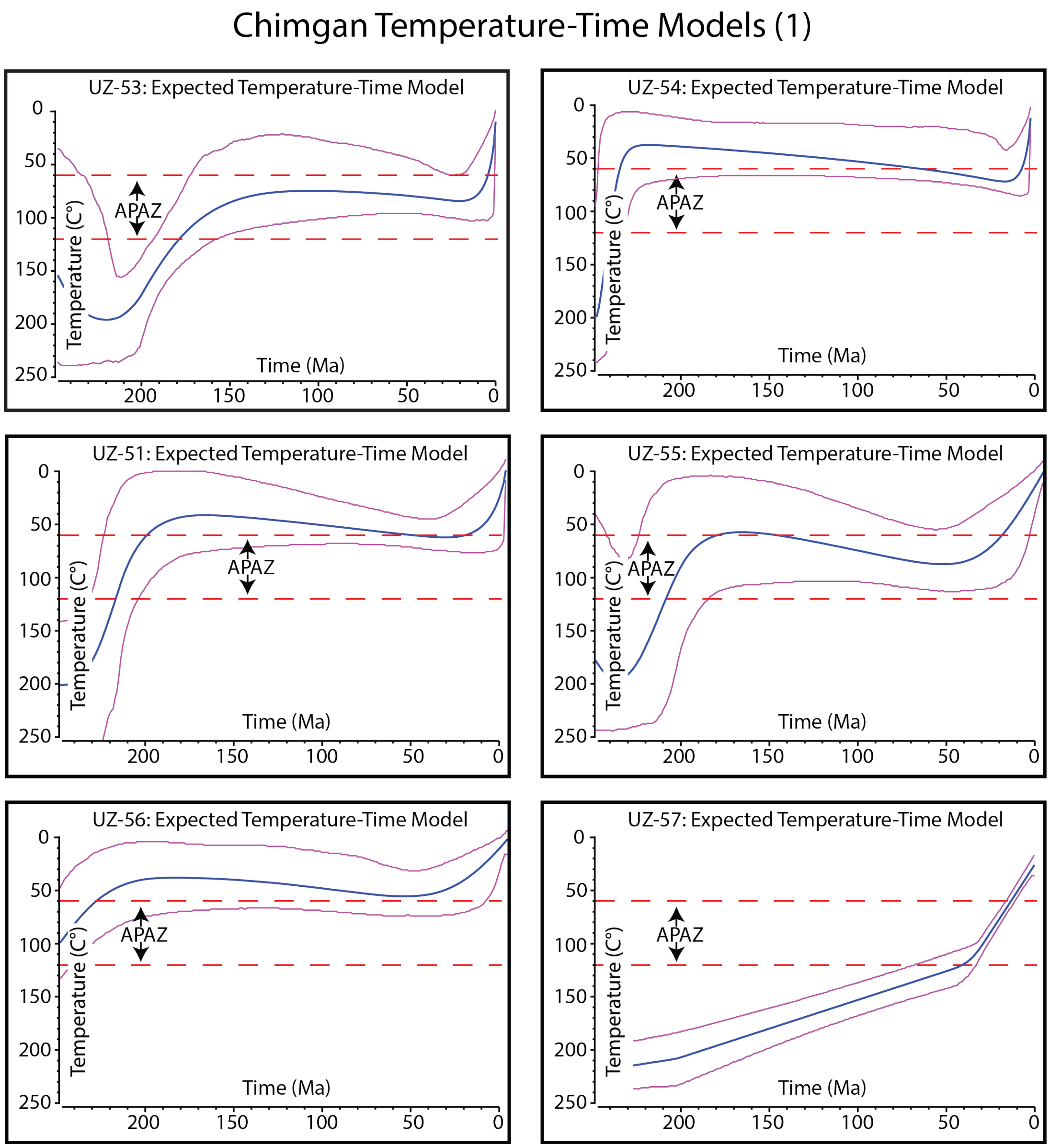

Supplementary File 5b:

Chimgan Temperature-Time Models (2)

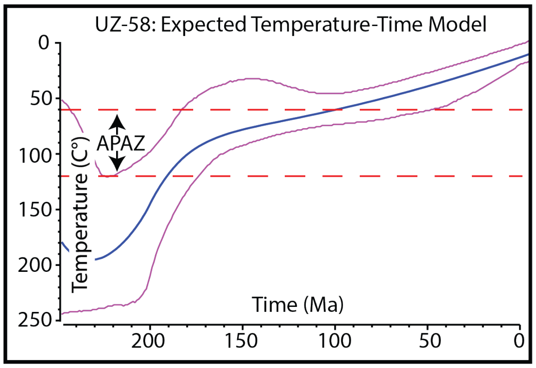

Supplementary File 5c:

Kamchik Pass Temperature-Time Models

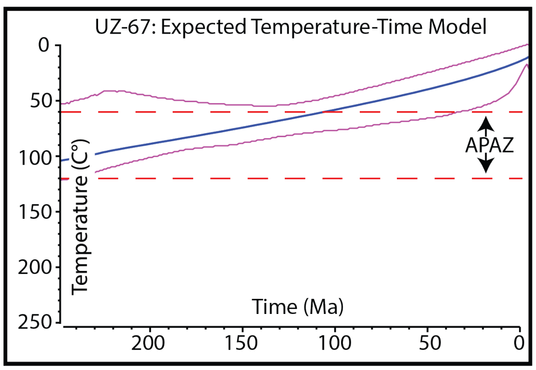

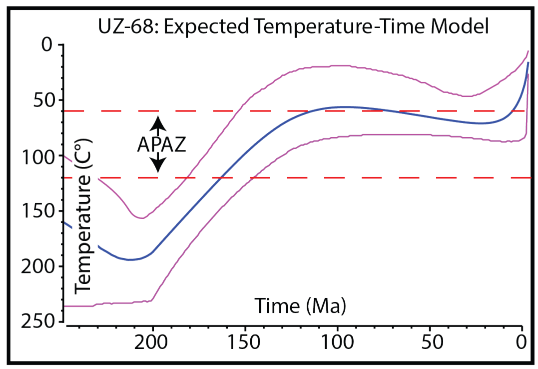

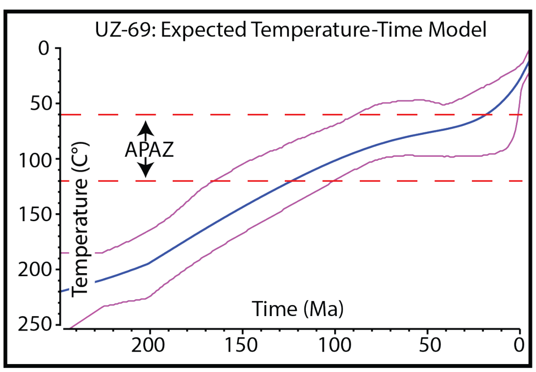

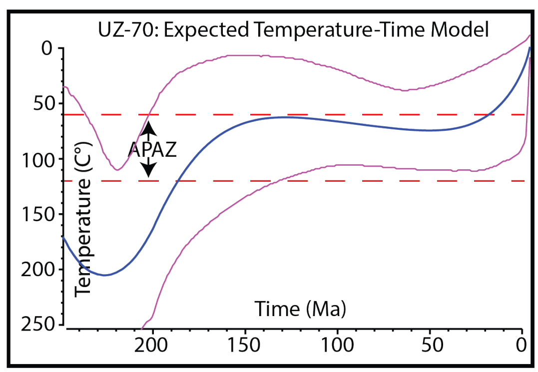

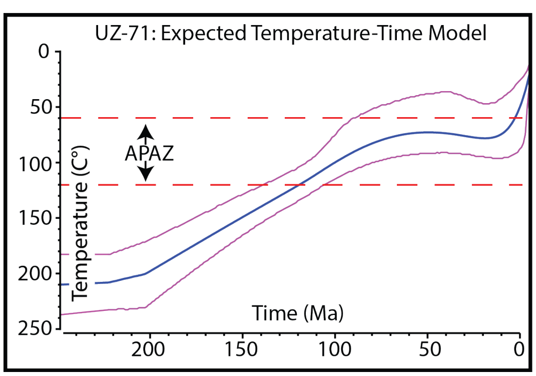

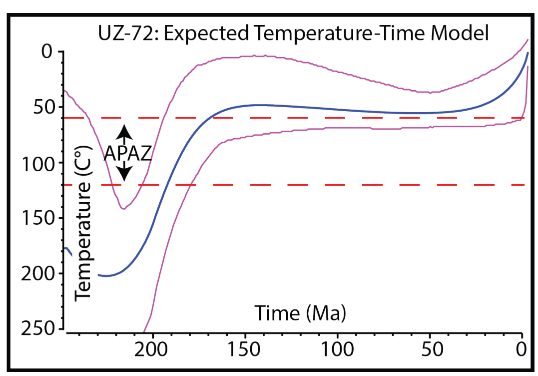

Supplementary File 5d:

Almalyk Temperature-Time Models (1)

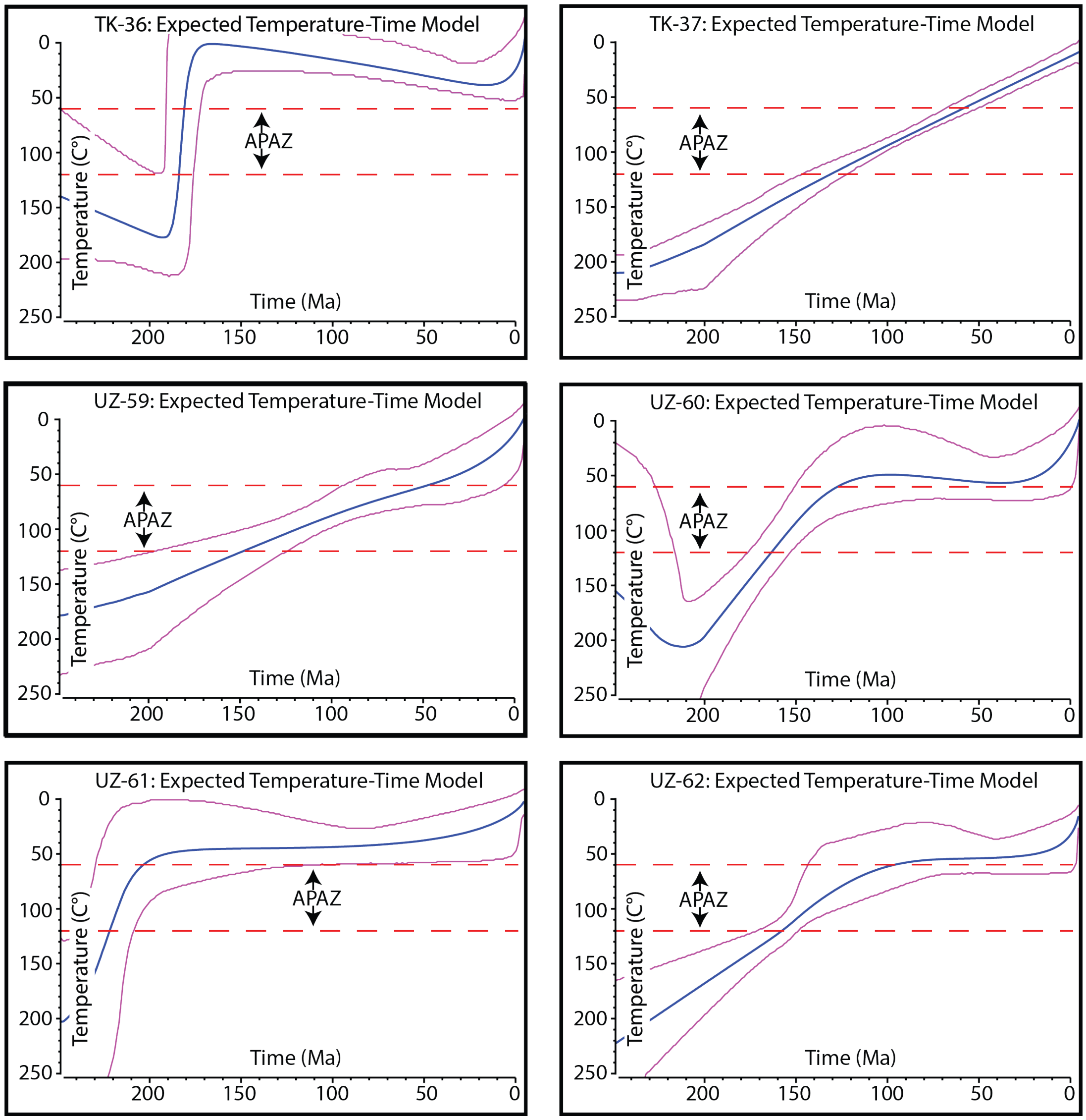

Supplementary File 5e:

Almalyk Temperature-Time Models (2)

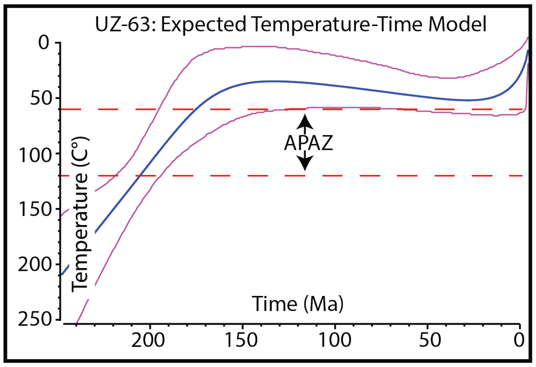

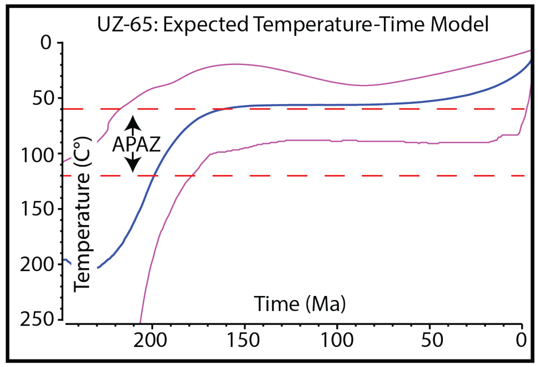

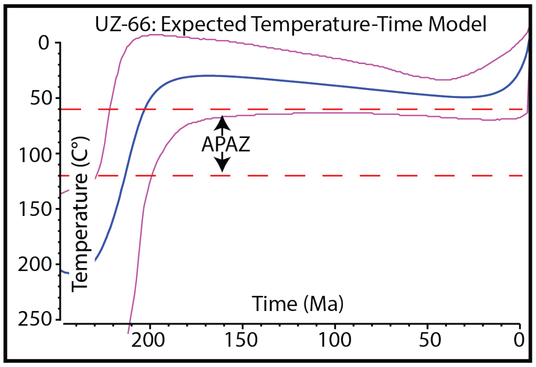

Supplementary File 5f:

Shaydon Temperature-Time Models

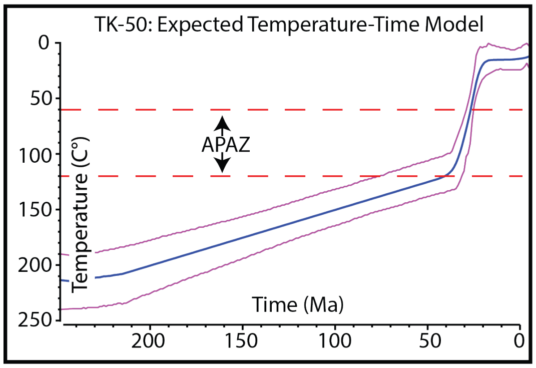

Supplementary File 5g:

Khujand Temperature-Time Models

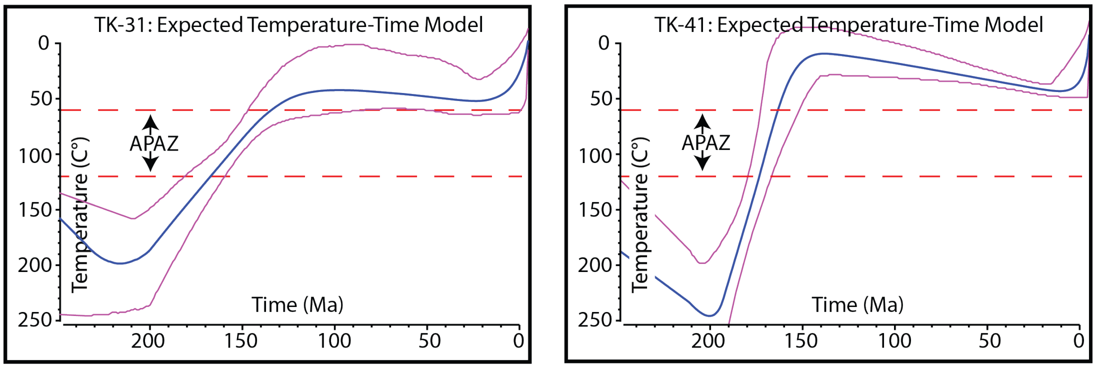

8.6 Supplementary File 6: Thermal History Modelling Parameters

Supplementary File 6: Thermal history model input table for simulations of the Chatkal-Kurama terrane, Uzbekistan and Tajikistan, based on framework established by Flowers et al. (2015)

1. Thermochronologic Data

Samples and data used in simulations

Simulation inputs				Data Source	All data needed for modeling published?
Sample Region	AHe	AFT	ZHe		
Chimgan					
UZ-53		×		Supplementary File 1	yes
UZ-54		x		Supplementary File 1	yes
UZ-55		x		Supplementary File 1	yes
UZ-56		x		Supplementary File 1	yes
UZ-57		x		Supplementary File 1	yes
UZ-58		x			
Kamchik Pass					
UZ-67		×		Supplementary File 1	yes
UZ-68		×		Supplementary File 1	yes
UZ-69	x	x		Supplementary File 1 and 2	yes
UZ-70		x		Supplementary File 1	yes
UZ-71		x		Supplementary File 1	yes
UZ-72		x		Supplementary File 1	yes
Almalyk					
TK-36	×	x	x	Supplementary file 1 and 2	yes
TK-37		×		Supplementary File 1	yes
UZ-57		×		Supplementary File 1	yes
UZ-60		×		Supplementary File 1	yes
UZ-61		×		Supplementary File 1	yes
UZ-62		×		Supplementary File 1	yes
UZ-63		×		Supplementary File 1	yes
UZ-65		×		Supplementary File 1	yes
UZ-66		×		Supplementary File 1	yes
Shaydon					
TK-50	x	x		Supplementary file 1 and 2	yes
Khujand					
TK-31		x		Supplementary File 1	yes
TK-41	x	×		Supplementary file 1 and 2	yes

Data treatment, uncertainties, and other relevant constraints

AHe Data

He dates (Ma): Single grain AHe ages were from Supplementary File 2 modelled individually

Error (Ma) applied in modeling: error of 1σ was used from Supplementary file 1

r (µm): Equivalent spherical radius of each grain

ZHe Data

He dates (Ma): Single grain ZHe ages were from Supplementary file 2 modelled individually

Error (Ma) applied in modeling: error of 1σ was used from Supplementary file 2

r (µm): Equivalent spherical radius of each grain

AFT data

Cl wt%: From Supplementary file 1

Lengths: Length data for all samples is available in Supplementary File 4

Initial mean track length: 16.3 μm

Track length reduction standard: 0.893

2. Additional geological information

Assumption	Explaination and data source
As all the samples were granitoid and there was no evidence for re-heating. Samples were assumed to have come from >120°C through the APAZ	

3. System- and model-specific parameters

He radiation damage model : Flowers et al. 2009

FT annealing model : Ketcham et al. 2007

FT c-axis projection : Not used

Modeling code : QTQt 5.6.0 PC

Statistical fitting criteria : Default QTQt values

MCMC Parameters : Burn-in = 200,000, Post-burn-in = 200,000

tT path characteristics : Not indicated